ULTRA-ACCELERATED ASSESSMENT OF ALKALI-REACTIVITY OF AGGREGATES BY NONLINEAR ACOUSTIC TECHNIQUES

A Dissertation
Presented to
The Academic Faculty

by

Jun Chen

In Partial Fulfillment
of the Requirements for the Degree
Doctor of Philosophy in the
School of Civil and Environmental Engineering

Georgia Institute of Technology
August 2010

ULTRA-ACCELERATED ASSESSMENT OF ALKALI-REACTIVITY OF AGGREGATES BY NONLINEAR ACOUSTIC TECHNIQUES

Approved by:

Dr. Kimberly Kurtis, Advisor
School of Civil and Environmental Engineering
Georgia Institute of Technology

Dr. Laurence Jacobs
School of Civil and Environmental Engineering
Georgia Institute of Technology

Dr. Glenn Rix
School of Civil and Environmental Engineering
Georgia Institute of Technology

Dr. Jin-Yeon Kim
School of Civil and Environmental Engineering
Georgia Institute of Technology

Dr. Jianmin Qu
Department of Civil and Environmental Engineering
Northwestern University

Date Approved: April 16, 2010

ACKNOWLEDGEMENTS

First of all, my deep gratitude goes to my two advisors, Dr. Kimberly Kurtis and Dr. Laurence Jacobs for providing me the opportunity, direction, encouragement and support to complete this research. I would also like to thank Dr. Jianmin Qu and Dr. Glenn Rix for giving me valuable suggestions for my research.

I would like to express my gratitude to Dr. Jin-Yeon Kim, for his inspiring discussions throughout all phases of my work. His help on the ultrasonic experimental instrumentation is greatly appreciated.

I want to thank the fellow PhD and Master students in my group, Amal Jayapalan, Robert Moser, Bo Yeon Lee, Chris Shearer, Jonah Kurth, Lisa Hoeke, Chiwon In, Krzysztof Lesnicki, and Dr. Victor Garas, for the technical assistances as well as good friendship. The nice atmosphere in our lab is always a good reason that I enjoy the life at Georgia Tech. Particularly I would like to thank Amal Jayapalan for providing petrographic images used in Chapter 4, and Robert Moser for help on the calibration of compression test equipment.

My gratitude also goes to the fellow PhD and Master students in the structures group. The lunch time over the past four year is a good memory of Georgia Tech.

I would like to thank the undergraduate assistants, Daniel Schuetz, Alex Crotty and Moe Yonehana, for their help on the research.

I would like to thank Georgia Department of Transportation and Portland Cement Association Education Foundation for the financial support.

Last but most importantly, I am deeply indebted to my parents and my wife. I thank my parents for their wholehearted support given for the every step I took in my life. Their unlimited encouragement is constantly the force which drives me to accomplish my goals. I cannot fully express the extent of gratitude to my wife for embracing me with so many uncertainties ahead. It is the most important and beautiful moment in my life. I am deeply appreciated for the emotional reinforcement she consistently gives, sharing my joy and pain.

TABLE OF CONTENTS

LIST OF TABLES

LIST OF FIGURES

LIST OF SYMBOLS

u	particle displacement
σ	stress
ρ	mass density
x,y	spatial coordinate
t	temporal coordinate
E_0	linear term of elastic modulus
E	elastic modulus
β	cubic parameter of material nonlinearity
δ	quartic parameter of material nonlinearity
α	hysteresis parameter of material nonlinearity
c_L	phase velocity of longitudinal waves
k_L	wave number of longitudinal waves
A	amplitude of longitudinal waves
A_2	amplitude of second harmonic
U_3	amplitude of sidebands
U_1	amplitude of high frequency signal
U_2	amplitude of low frequency signal
L	beam length
S	beam cross-section area
b	beam cross-section width
h	beam cross-section thickness
ε	strain

$\Delta\varepsilon$	strain amplitude
$\dot{\varepsilon}$	strain rate
M	bending momentum
I	moment of inertia
τ_0	damping coefficient
$F(t)$	force per unit length
ω	augular frequency
f	ordinary frequency
U	amplitude of transverse waves
ϕ	phase of transverse waves
Ω	normalized angular frequency
Q	quality factor
E_1	probing energy
E_2	impact energy
E_3	sideband energy

SUMMARY

This research develops two novel experimental techniques based on nonlinear acoustics/ultrasound to provide an ultra-accelerated characterization of alkali-reactivity of aggregates. Alkali-silica reaction (ASR) is a deleterious reaction occurring between reactive siliceous minerals present in some aggregates and alkalis mainly contributed by the cement, but also present in some deicing chemicals. With increasing reports of ASR-induced damage in transportation structures, there is a critical need for fast and reliable test methods for the screening of aggregates and aggregate/paste combinations. Currently, the accelerated mortar bar test (AMBT), which measures expansion, is the most commonly used test method. Also used is the concrete prism test (CPT), another expansion-based method, which requires at least one year testing time, limiting the practical utility of this method. In addition, petrographic analysis can be performed to identify potentially reactive minerals in aggregates but requires training and may not be appropriate for assessment of aggregate/paste combinations. Finally, linear acoustic methods such as wave speed and attenuation measurements can be used for the assessment of ASR, but the sensitivity of linear acoustic methods to ASR-induced damage is considered to be relatively low. Therefore, critical limitations exist in the existing test methods.

In light of recent advances in nonlinear acoustics (which are more sensitive to small-scale damage than linear acoustics), the purpose of this research is the development and assessment of an accelerated method for evaluating the potential for alkali reactivity in aggregate and aggregate/paste combinations by combining advanced ultrasonic methods with standard test procedures. In fact, two nonlinear acoustic methods are

developed under this research – nonlinear wave modulation spectroscopy (NWMS) and nonlinear impact resonance acoustic spectroscopy (NIRAS) – and are used to characterize the changes in material nonlinearity as a result of the progressive ASR damage during the standard mortar bar and concrete prism testing. Following the AMBT and CPT, nonlinear acoustic techniques are applied to both mortar bars and concrete prism samples. Nonlinearity parameters are defined as the indicator of growing ASR damage, and measurement results clearly show that these nonlinearity parameters are more sensitive to the ASR damage than the linear parameters used in the linear acoustic measurements, particularly at early ages. Different aggregates with varying alkali-reactivity are effectively distinguished with the proposed experimental techniques in a timely manner, particularly for those aggregates with similar levels of reactivity, as determined by AMBT.

The effect of a Class C fly ash addition on nonlinear properties was also investigated using the NIRAS measurements through a comparison of test results between mortar samples blended with fly ash and without fly ash. As complementary supports of the experimental results, petrographic analyses and theoretical modeling are also performed, and these results are well correlated with results from the NWMS and NIRAS techniques.

Through a comparison with results from accompanying expansion measurements and linear acoustic methods, the proposed nonlinear acoustic techniques show their advantages to accelerate the assessment of alkali-reactivity of aggregates. Under AMBT, reactive aggregates were identifiable as early as a few days of testing. With CPT, reactive aggregates were differentiated as early as a few weeks. Overall, the coupling of the

developed nonlinear test methods with standard expansion tests suggests that test durations could be potentially reduced by half, especially for AMBT tests.

CHAPTER 1

INTRODUCTION

1.1 Background of Alkali-Silica Reaction (ASR)

Alkali-silica reaction (ASR) is a deleterious chemical process that may occur in cement-based materials such as mortars and concretes, where the hydroxyl ions in the highly alkaline pore solution attack siliceous mineral components of aggregates. Aggregates containing siliceous minerals which are disordered, amorphous, strained, or cryptocrystalline are known to be particularly susceptible to this reaction [1-3]. Hydroxyl ions together with alkali metal cations (sodium or potassium) bind with siliceous species derived from the reactive minerals to form a cross-linked alkali-silica gel. The alkali-silica gel swells with imbibition of water from the surrounding material [4]. The expansion of gel results in cracking when the swelling stress exceeds the tensile capacity of the paste or aggregates. As expansion increases, cracks grow and eventually coalesce; the strength and modulus of the material are decreased and the permeability is increased [5]. The cracking produced by ASR damage can significantly undermine the durability of concrete structures and may result in reduced service life [6].

ASR was first identified in 1940 [7] and the ASR-damaged concretes have been discovered broadly in the United States and around the world. Figure 1.1 shows typical ASR damage found at the Hartsfield-Jackson international airport of Atlanta, United States and in Trondheim, Norway, respectively.

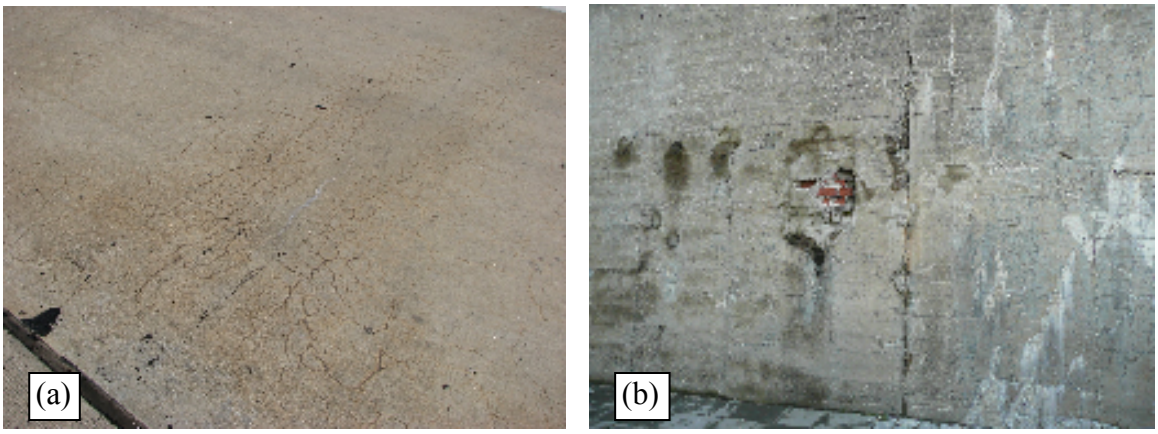

Figure 1.1 ASR damage in concrete structures found in (a) Atlanta, Georgia USA and (b) Trondheim, Norway

Although the detailed mechanism of ASR formation is not completely understood to date, it is well accepted that three essential components are necessary for damage to occur by ASR: (1) reactive siliceous minerals from aggregates, (2) sufficient alkalis (e.g., Na^+, K^+, Ca^{2+}), and (3) sufficient moisture. Therefore, it is crucial to reduce the alkali loading in concrete (e.g., use low alkali cement, reduce cement content, or limit use of alkali-containing deicers) and utilize aggregates with low alkali-reactivity to minimize the occurrence of ASR where exposure to moisture in service is anticipated.

Routine testing to determine alkali-reactivity of aggregates can be challenging because the demand of aggregates in the concrete industry is exceedingly large (the annual consumption of aggregates worldwide is estimated to be 9 billion metric tonnes [6]), and the reactivity of aggregates is variable, even within a single source. In addition, with increasing concrete alkali contents (stemming from both increasing cement alkali contents and increasing cement contents in concrete over recent decades), growing use of higher alkali supplementary cementitious materials (SCMs), increased use of external deicing agents, and – in some parts of the world – increased reliance on marginal

aggregate resources, screening of aggregates for alkali-reactivity is more critical than ever. Therefore, it is of great interest for the industry to establish a standard testing method to determine the alkali-reactivity of aggregates rapidly and reliably.

Conventionally, petrographic analysis and expansion tests are broadly used in research and industry for characterizing the alkali-reactivity of aggregates. Petrographic examinations are commonly used to evaluate the mineral compositions of aggregates, including identification and quantification of ASR reactive minerals [8]. By approximating the volume fraction of reactive minerals, an aggregate may be determined to be potentially reactive [9]. However, petrographic analysis cannot be used to designate an aggregate as non-reactive because some reactive phases may not be indentified by optical microscopy [10]. In addition, petrography can also be used to estimate ASR damage in mortars and concretes through the observation of reaction products, such as ASR gel, and by observations of characteristic crack patterns [11]. These methods require a skilled petrographer experienced in identifying reactive aggregates. Furthermore, petrography examination of aggregates are generally time consuming to perform and may require additional testing to validate the initial analysis [10].

Expansion test methods assess ASR damage based on length change measurements of mortar or concrete specimens when exposed to conditions known to accelerate ASR. The typical expansion test methods used in United States are accelerated mortar bar tests ASTM C 1260 [12], accelerated mortar bar tests using SCMs ASTM C 1567 [13], and concrete prism tests ASTM C 1293 [14]. The simple operation procedure and low cost of these expansion tests make them a suitable option for routine use. However, the long testing duration (1-2 years) of ASTM C 1293 makes it unfeasible for

routine testing in practice. Accelerated mortar bar tests ATSM C 1260 and ASTM C 1567 can be completed in a relatively short period (14 days of exposure) but they are commonly performed every three years or less [15] and considered overly severe [16] due to its extreme test environment including the high temperature and high alkaline storing solution for samples.

Lately, researchers have been working to develop new test methods by trying to balance the tradeoffs between reliability and test duration [17-20]. Nevertheless, nearly all of these new methods are still based on the principle of length measurement, and the modifications are focused on the experimental details, such as the size of the aggregates, size of the samples or the storing temperature. Meanwhile, practical and routine use of these new methods remains on the horizon, with concerns regarding the suitability of some of these proposed methods [20].

Overall, the current prevalent testing methods for ASR mainly focus on the measurement of specimen length, which is a bulk assessment of ASR damage and does not accurately characterize the varying stages of ASR occurring within the sample, such as the initial formation of ASR gel, crack initiation, and the progressive damage by crack propagation and increasing crack interconnectivity. Such information is useful in determining appropriate materials and mixture proportions for concrete used in critical applications. The limitations of existing test methods urge the development of an ultra-accelerated, but still simple and reproducible test method for the routine screening of aggregate alkali-reactivity.

1.2 Research Motivation

Acoustic and ultrasonic techniques have been well-developed for the detection of accumulated damage of materials [21, 22]. In the early research, methods based on linear acoustics such as measurements of changes in phase velocity and signal amplitude were popular. The linear acoustic/ultrasonic methods were essentially correlated to the change of linear material properties such as Young's modulus and had some success for the damage characterization of metallic materials. Recently these linear methods have drawn increasing interest [23-25] for the ASR characterization. Similar to defects in metallic materials, ASR damage in concrete also alters the elastic properties of materials at the microscopic scale. For instance, experiments showed that the elastic modulus of alkali-silica gel was significantly different from that of cement paste or aggregates, and that it varied under different internal pressures [26]. From the point of view of micromechanics, the occurrence of ASR gel and microcracking throughout the progression of ASR damage must increase the heterogeneity of multiple-phase cement-based materials, and change the overall elastic properties of this composite material which eventually results in the variation of linear acoustic parameters.

Although these linear acoustic/ultrasonic techniques provide a perspective for the ASR characterization that is different from the conventional approach of expansion measurements, a fundamental assumption of linear-elastic constitutive material behavior is adopted in the measurements. It is thus assumed that the elastic properties of measured materials are independent of the elastic deformation. However, both mortar and concrete do not follow this assumption. The sensitivity and reliability of these techniques based on

linear measurements are thus likely not appropriate for use as a standard laboratory method for screening aggregates.

Recent research [27, 28] has consistently demonstrated that a more accurate constitutive relation should be adopted for the damaged materials, including both the ordinary linear terms and those non-negligible nonlinear terms. Any damage to the microstructure results not only in changes of linear parameters, such as a decrease in Young's modulus and an increase in the attenuation coefficient, but also in an increase in the nonlinearity parameters associated with the nonlinear terms in the constitutive relation of materials. The nonlinearity parameters are shown a much higher sensitivity to the progress of damage when compared to their linear counterparts [28]. This is particularly important for cement-based materials, because their inherent heterogeneity may adversely affect the measurements.

In recent years, experimental techniques [29-33] based on nonlinear acoustic/ultrasonic measurements have attracted significant attention for their potential application in the early diagnostics of material damage. The very early application of these nonlinear acoustic/ultrasonic techniques was also first deployed for metallic materials. For example, with the development of small-scale and distributed damage (e.g., dislocations and microcracking) due to fatigue, the stress-strain relationship of the material deviates from its initial linear behavior and the nonlinear contribution increases [29-31]. The nonlinearity of the constitutive relation essentially provides the theoretical background for various nonlinear acoustic phenomena observed in elastic waves propagating in damaged materials. For instance, Kim et al. [29], Herrmann et al. [30] and Pruell et al. [31] reported on the generation of the second order harmonic in the initially

monochromatic incident waves and they related this phenomenon to the fatigue damage in metallic and alloy materials. Donskoy et al. [32] and Ekimov et al. [33] investigated cracks in steel samples using the phenomenon of nonlinear cross interaction between a low frequency vibration and high frequency elastic waves (nonlinear wave modulation).

The recent advances in the application of nonlinear acoustic/ultrasonic techniques in metallic materials provide new insight into characterizing ASR damage in cement-based materials. The most important advantage of nonlinear acoustic techniques over conventional expansion methods or recent linear acoustic/ultrasonic techniques is the enhanced sensitivity to the material structure (and damage of that structure). Cement-based materials are inherently heterogeneous and their attenuating effect on the propagation of ultrasonic wave signals is much more significant than the attenuation of relatively homogenous metallic materials. Therefore, the high sensitivity of nonlinear acoustic/ultrasonic techniques can ensure good output signal regardless of the magnitude of input power. In addition, the early determination of aggregate reactivity is of particular importance in the concrete industry since it results in cost and time savings. The successful use of nonlinear acoustic/ultrasonic techniques for the early detection of damage in metals suggests the potential of these methods for early detection of ASR damage in cement-based materials.

1.3 Research Purpose and Objectives

The purpose of this research is to develop accelerated experimental techniques for the evaluation of alkali-reactivity in aggregates and aggregate/paste combinations, to be performed in conjunction with current standard test procedures. The objectives of this

research are to determine if advanced acoustic/ultrasonic methods may be used in combination with the commonly used AASHTO T 303 [34](similar to ASTM C 1260) and/or ASTM C 1293 to provide an earlier indication of aggregate reactivity than currently available. Furthermore, this research will examine if damage parameters defined by advanced acoustic/ultrasonic methods can be used to quantify accumulative ASR damage during the standard testing and if limits for these defined damage parameters can be recommended for the identification of aggregate reactivity.

1.4 Outline of Dissertation

The structure of the dissertation is outlined as below

Chapter 1 presents an introduction to the research background on the ASR damage and nonlinear acoustics, and the purpose and objectives of this research.

Chapter 2 provides a thorough literature review, including the existing testing methods for the characterization of ASR in mortars and concretes and the state-of-the-art of nonlinear acoustic/ultrasonic testing methods, with particular emphasis on the recent applications in cement-based materials.

Chapter 3 summarizes the materials used in the experiments of this research, and presents the results from AMBT and CPT expansion measurements.

Chapter 4 presents microscopy techniques used in the research and corresponding petrographic images for the mortar samples tested in experiments.

Chapter 5 presents the results from two linear measurements, including the elastic modulus and pulse velocity.

Chapter 6 reports the details of theoretical background on the nonlinear wave modulation theory and nonlinear impact resonance theory.

Chapter 7 presents the nonlinear wave modulation spectroscopy developed in the research, including experimental set-up, and experimental results and discussions for mortar samples.

Chapter 8 presents the nonlinear impact resonance acoustic spectroscopy, including experimental set-up, experimental results and discussions for mortar samples and concrete samples, and a numerical simulation using the nonlinear impact resonance theory, derived in Chapter 6.

Chapter 9 summarizes the research and provides recommendations for the future work.

CHAPTER 2

LITERATURE REVIEW

In this chapter, test methods used in various parts of the world for ASR characterization are reviewed. Both expansion-based test methods and acoustic/ultrasonic methods (including linear and nonlinear methods) are considered in this chapter. (A brief review of petrographic characterization of aggregate mineralogy toward the identification of reactive aggregates was provided in Chapter 1.)

2.1 Existing Expansion Test Methods

As stated earlier, test methods based on expansion measurement of specimens are very common in the concrete industry due to their simple operation procedure and relatively low cost. Although the standard expansion test methods employed in different countries vary by sample size, curing procedure, and expansion limit, they can be placed into three general categories: (1) accelerated mortar bar test methods, (2) concrete prism methods and, (3) accelerated concrete prism methods. In this section, a detailed review is presented for the expansion test methods used around the world.

Each category of the expansion methods has its own advantages and disadvantages. For example, the accelerated mortar bar tests are generally favored among the expansion tests because of their relatively short duration. However, concerns surround the severe testing conditions (high temperature and strongly alkaline solution) and the need to crush and sieve coarse aggregates for the test may lead to the rejection of an aggregate which may perform suitably in the field [16]. While the concrete prism test

provides better reliability for the prediction of ASR expansion in field performance, the long test duration is a significant practical drawback. The test duration is shortened in the accelerated concrete prism test, but remains lengthy and relationships between ACPT results and field performance remain uncertain. An ideal test method should be able to rapidly identify the possible alkali-reactivity of unprocessed aggregates with good reliability. It is obvious that the uneven trade-off between the test reliability and test duration of these expansion methods required improvement. Thus, a rapid and potentially more accurate test method is still needed for the assessment of reactivity of a particular combination of aggregates and pastes.

2.1.1 Accelerated Mortar Bar Test (AMBT) Methods

The accelerated mortar bar test was first developed at the National Building Research Institute (NBRI) in South Africa [35]. This test is prescribed by many organizations for assessing the alkali-reactivity of aggregates, including the American Society for Testing and Materials (ASTM), American Association of State Highway and Transportation Officials (AASHTO), and Canadian Standards Association (CSA). As follows, several accelerated mortar bar test methods are introduced and compared.

2.1.1.1 ASTM C 1260 (ASTM C 1567)

In this method [12], the aggregates are processed to a standard gradation as shown in Table 2.1. (However, ASTM is also considering a provision to allow testing of aggregates in their as-received gradation when that gradation will be specified for a particular project.) There is no requirement for the cement alkali content as they are

found to have negligible or minor effects on expansion in this test [12]. The mortar bars are made based on a cement-aggregate mass ratio of 1:2.25 and a water-to-cement ratio (w/c) of 0.47 by mass. After 24 hours curing, the specimens are removed from molds and placed in containers with sufficient water to completely immerse them. Following immersion, the containers are transferred to an oven at 80°C for the next 24 hours. The first reading of the initial mortar bar length is taken immediately after they are removed from the hot water. After initial readings, the specimens are immersed in containers with a 1N NaOH solution at 80°C for 14 days. During the 14-day exposure period, measurements of specimen length are made periodically, with at least three intermediate readings. When the expansion of specimens is less than 0.10%, the aggregates are considered innocuous; when the expansion is within 0.10% to 0.20%, the aggregates are considered potentially reactive; when the expansion is larger than 0.20%, the aggregates are considered reactive [12].

In fact, however, these expansion limits are not universally accepted. Because some deleterious aggregates having a slow reaction rate could be passed with given a "false negative", some are now increasing the testing duration to 28 days and defining new expansion limits [36]. For example, the Brazilian Standards Association recently proposed to use a limit of 0.19% at 28 days [37]. To reduce the risk of ASR, others are providing lower limits on expansion. For example, the Department of Defense allows just a 0.06% expansion at 14 days during AMBT.

Table 2.1 Grading requirement in ASTM C 1260.

Sieve Size		Mass %
Passing	Retained on	
4.75 mm (No. 4)	2.36 mm (No. 8)	10
2.36 mm (No. 8)	1.18 mm (No. 16)	25
1.18 mm (No. 16)	600 μm (No. 30)	25
600 μm (No. 30)	300 μm (No. 50)	25
300 μm (No. 50)	150 μm (No. 100)	15

When the SCMs are used in the AMBT, the modified version of ASTM C 1260, ASTM C 1567 should be used [13]. A certain amount of cement is replaced by SCMs, and the binder-aggregate ratio and water-binder ratio remain the same as values given in ASTM C 1260. A high range water reducer may be added when the silica fume or metakaolin are used to provide the adequate workability. The combination of SCMs and aggregate will be accepted for use if the expansion is less than 0.10% at 14 days.

2.1.1.2 AASHTO T 303

The preparation of mortar bars and subsequent measurements in AASHTO T 303 [34] is almost the same as in ASTM C 1260. A minor difference lies in the water-to-cement ratio when casting the specimens. In this method, the required w/c is 0.50 instead of 0.47 of ASTM C 1260. The expansion limit of AASHTO T 303 is also 0.1% at 14 days. The use of SCMs is currently not considered in the AASHTO standard.

Table 2.2 Grading requirement in CSA A23.2-25A.

Sieve Size		Mass %
Passing	Retained on	
5 mm	2.5 mm	10
2.5 mm	1.25 mm	25
1.25 mm	630 μm	25
630 μm	315 μm	25
315 μm	160 μm	15

2.1.1.3 CSA A23.2-25A

CSA A23.2-25A [38] is also quite similar to ASTM C 1260 in most respect. However, it requires the equivalent alkali ($Na_2O + 0.658K_2O$) content of the cement used to be 0.90±0.10%. In addition, the aggregate grading requirement of this method is different from that of ASTM C 1260 (seen in Table 2.2). The curing procedure of CSA A23.2-25A is the same as in ASTM C 1260 – remove specimens from moulds after 24 hours curing and then immerse them with sufficient water in the storage containers stored at 80°C for 24 hours. After the initial reading, specimens are put in 1N NaOH solution at 80°C for 14 days. In addition, the expansion criteria in CSA A23.2-25A is that when the expansion is larger than 0.15% at 14 days, the aggregates are considered as reactive (except limestone); for limestone, the limit on expansion is 0.10% at 14 days.

The effectiveness of SCMs in AMBT methods is also introduced in CSA A23.2-28A [39]. The water-to-binder ratio is modified to obtain a slump of 50-100 mm for concrete (for SCMs containing silica fume and metakaolin, an initial slump of 50-80 mm for concrete at a water/blinder ratio of 0.35-0.45 is required). The reduction of alkali content in the mixture due to the replaced cement by SCM shall be reimbursed by the addition of NaOH. The proposed mix design with SCMs is deemed as effective when

expansion of such a combination (SCM and reactive aggregate) is less than 0.1% at 14 days.

2.1.1.4 RILEM TC 106-2 (RILEM AAR-2)

RILEM TC 106-2 [40] is the accelerated test method for ASR used in most European Union nations. In this method, a minimum cement equivalent alkali content of 1.0% is required and the w/c ratio is 0.47. Since RILEM TC 106-2 also originated from the NBRI accelerated test method, the preparation of mortar bars and the measurement of expansion are the same as ASTM C 1260 except the aggregate gradation requirement which is given in Table 2.3. The 14 day expansion limit of this method is described as: non-reactive for expansion less than 0.10%, reactive for expansion more than 0.20%, potential reactive for expansion in between 0.10%-0.20% [41].

Table 2.3 Grading requirement in RILEM TC 106-2.

Sieve Size		Mass %
Passing	Retained on	
4 mm	2 mm	10
2mm	1 mm	25
1 mm	500 μm	25
500 μm	250 μm	25
250 μm	125 μm	15

2.1.1.5 Chinese Accelerated Mortar Bar Test

The Chinese accelerated mortar bar test (CAMBT) is a relatively newer method which has been primarily used for the assessment of ASR in China [42]. The CAMBT was developed on the basis of the Chinese autoclave method [43] in which the small size of test specimens (10×10×40mm) is not very suitable for the quality control test of

aggregate quarries. In the currently employed CAMBT, larger aggregate sizes are used and larger (40×40×160mm) mortar bars are cast in order to conserve the textural characteristics of the reactive phases. The water-to-cement ratio in CAMBT is 0.33 and three cement-aggregate ratios are used (10:1, 2:1 and 1:1). Low-alkali cement is used and additional KOH shall be added in mixing water to bring the total alkalis to 1.5% Na_2O equivalent. The CAMBT uses a single size fraction of aggregates (0.15-0.8mm) and the mixing and molding procedures follow the requirements of CSA A23.2-25A. Aggregates whose expansion is larger than 0.10% at 7 days after initial reading (initial reading is after 4 hours' immersion of 1 N NaOH solution at 80°C) are considered reactive. The use of SCMs is not addressed in the current CAMBT specification.

Due to the practical advantage of using larger aggregate sizes and the shorter test duration (7 days) offered by the CAMBT, this method has attracted interest worldwide recently, and researchers from other countries are also examining various permutations of this test method [44-46]. For instance, Lu et al. [44] examined the influence of aggregate particle size on the applicability of CAMBT by evaluating 11 different aggregates from Canada, USA, Norway and Australia. Grattan-Bellow et al. [45] proposed a modified CAMBT method by changing the aggregate particle size for differentiating alkali-silica aggregates and alkali-carbonate aggregates. A most recent research conducted in Europe [46] also adopted a modification of the CAMBT for the ASR assessment of local aggregates.

2.1.1.6 Limitation of Accelerated Mortar Bar Tests

A comparison of different AMBT methods is summarized in Table 2.4. Although these AMBT methods based on the NBRI method are fast and simple techniques and have been used in a variety of regions, they are generally regarded as overly severe methods because of their extreme test conditions, including the use of a highly alkaline storage solution, elevated exposure temperature, fine aggregate, and samples with high surface area to volume ratios. In addition, the test is not likely suitable for examining aggregate/cement combinations, as the alkali content of the cement is overwhelmed by the high alkali content of the surrounding solution. Thus, these methods will identify some aggregates to be reactive, even though they may have good performance in the field and in concrete prism tests. For instance, Shayan et al. [47] tested 49 aggregates in Australia using both AMBT and CPT methods. Twenty-one of the 39 aggregates identified as reactive by AMBT would not be considered aggressive according to the results of CPT.

Therefore, AMBT is more suitable to be a screening method, where non-reactive aggregates can be clearly identified and where potentially reactive aggregates can be identified for further testing by CPT, which is regarded as a more reliable test. Thomas et al. [48] reported that only 3 of 184 tested aggregates passed AMBT but failed in the CPT method. Sancherz et al. [36] also found one aggregate in Brazil that passed AMBT but showed deleterious behaviors in the field.

Table 2.4 Comparison of different AMBT methods.

	ASTM C 1260	AASHTO T 303	CSA A23.2-25A	RILEM TC 106-2	CAMBT
Water/cement ratio (mass)	0.47	0.50	0.44 (nature sand) 0.50(crushed sand)	0.47	0.33
Cement alkalis (Na_2O eq.)	Not required	Not required	0.9±0.1%	1.0%	1.5%
Aggregate size (mm)	0.15-4.75	0.15-4.75	0.16-5.0	0.125-4.0	0.15-0.80
Cement-aggregate ratio	1:2.25*	1:2.25	1:2.25	1:2.25	10:1, 2:1, 1:1
Bar size (mm)	25×25×285	25×25×285	25×25×285	25×25×285	40×40×160
Curing conditions	23℃, ≥95% RH for 24 hours	23℃,≥95% RH for 24 hours	23℃,≥95% RH for 24 hours	20℃, ≥90% RH for 24 hours	23℃,≥95% RH for 24 hours
Storage temperature	80℃	80℃	80℃	80℃	80℃
Storage solution	1.0N NaOH	1.0N NaOH	1.0N NaOH	1.0N NaOH	1.0N NaOH
Initial reading	24 hours after water@80℃	24 hours after water@80℃	24 hours after water@80℃	24 hours after water@80℃	4 hours after 1N NaOH@80℃
Criteria	<0.1% innocuous 0.1%-0.2% potentially reactive >0.2% reactive (@14 days)	<0.1% innocuous >0.1% potentially deleterious expansion (@14 days)	>0.15% reactive (except limestone) >0.1% reactive (limestone) (@14 days)	<0.1% non-reactive 0.1%-0.2% potentially reactive >0.2% reactive (@14 days)	>0.10% reactive (@7 days)

* cement-aggregate ratio is 1:2.25 for aggregate with a density at or over 2.45
For aggregates with a relative density below 2.45, aggregate proportion = 2.25×D/2.65 (D is relative density)

Recently, the U.S. Federal Highway Administration (FHWA) proposed a more quantitative approach to correlate the AMBT and CPT results for a specific aggregate. If the results of an aggregate fall within the region indicated in Figure 2.1, the AMBT results of this aggregate have a good correlation with the CPT results. This approach could be used to determine the efficiency of SCMs and chemical admixtures [10]. Overall, it is recommended that the AMBT methods should only be employed to accept, not reject, aggregates. Any aggregate claimed reactive or potentially reactive by the AMBT should be confirmed by concrete prism tests and petrographic analysis before being rejected.

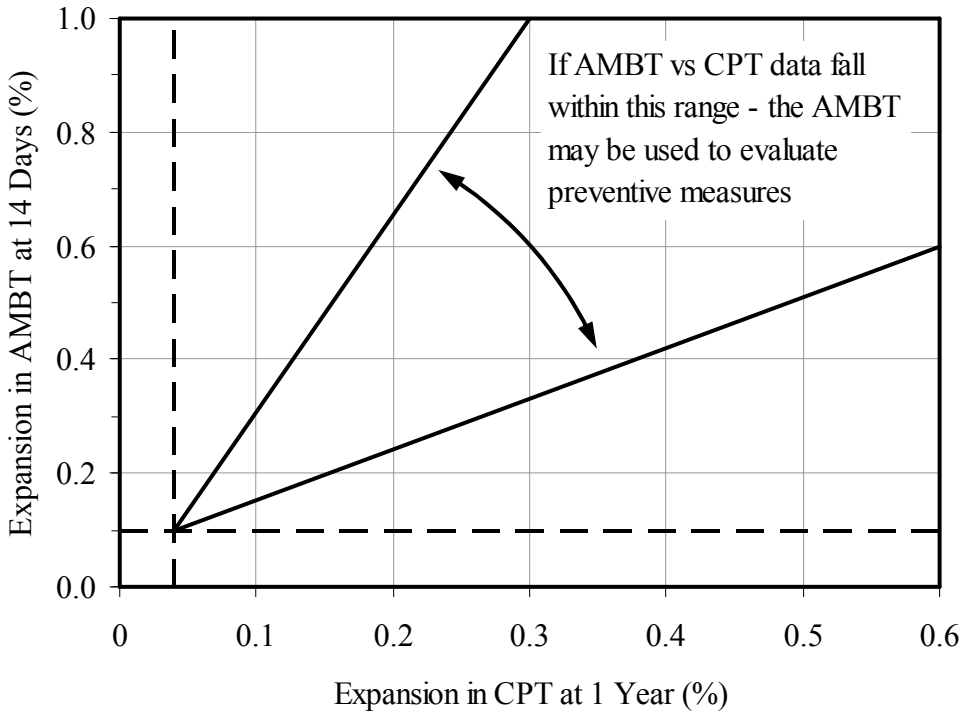

Figure 2.1 Correlation between AMBT results and CPT results for a specific aggregate (adopted from Folliard et al. [10]).

2.1.2 Concrete Prism Test (CPT) Methods

The concrete prism test is recognized as the most reliable test method for the assessment of ASR. When the AMBT results contradict CPT results, the latter shall govern [49]. However, the duration of the test is significantly longer than any of the AMBTs. Many organizations have standard CPT methods, including ASTM, CSA and RILEM. These concrete test methods are summarized and compared below.

2.1.2.1 ASTM C 1293

ASTM C 1293 [14] can be used for ASR assessment of both fine and coarse aggregates. A non-reactive fine aggregate is used to evaluate the reactivity of a coarse aggregate, and a non-reactive coarse aggregate is used to evaluate the reactivity of a fine aggregate. Here, the non-reactive aggregates are defined as aggregates satisfying the expansion limit in ASTM C 1260 (0.10% at 14 days). When evaluating the reactivity of a fine aggregate, the coarse aggregates should conform to the grading requirement in Table 2.5 and the fine aggregates are used with the grading as delivered to the laboratory.

Table 2.5 Grading requirement in ASTM C 1293.

Sieve Size		Mass %
Passing	Retained on	
19 mm (3/4-in.)	12.5 mm (1/2-in.)	33
12.5 mm (1/2-in.)	9.5 mm (3/8-in.)	33
9.5 mm (3/8-in.)	4.75 mm (No. 4)	33

Table 2.6 Classification of aggregate reactivity.

Aggregate-Reactivity Class	Description of aggregate reactivity	One-Year Expansion in CPT (%)
R0	Non-reactive	< 0.040
R1	Moderately reactive	0.040 – 0.120
R2	Highly reactive	0.120 – 0.240
R3	Very highly reactive	> 0.240

In this test, concrete is cast with a cement content of 420kg/m^3 and w/c in the range of 0.42-0.45. The cement used must have total alkali content between 0.8% and 1.0%, with NaOH added to the mixing water to bring the alkali content of mixture to 1.25% by mass of cement, which corresponds to an alkali level of 5.25 kg/m^3 of concrete. Concrete prisms (75×75×275mm) are made and cured with a plastic cover at 23°C for 24 hours. After demolding, the initial reading is conducted. Thereafter, the specimens are stored over water in sealed containers at 38°C. The typical test lasts for one year and the expansion measurements are taken at regular intervals. The expansion limit which indicates an alkali-reactive aggregate is 0.04% at one year in ASTM C 1293. A recent FHMA report [10] provides a more detailed classification of aggregate reactivity corresponding to different expansion values measured in CPT tests, as seen Table 2.6. Others, however, use stricter limits to define aggregate reactivity during CPT. The

Department of Defense, for example, uses an expansion of 0.03% at one year as a limit for non-reactive aggregates.

The use of SCMs in ASTM C 1293 is mentioned shortly in a report by FHWA [10] but has not yet been included in ASTM specification. According to FHWA, cement is partially replaced by SCMs while the total cementitious content is maintained at 420kg/m^3. The alkali content of the Portland cement component only shall be raised to 1.25% Na_2O_e. The water-to-binder ratio remains in the range of 0.42-0.45 and a high-range water-reducing admixture may be added to avoid low workability. The expansion of combinations of SCMs and aggregates is acceptable if less than 0.04% at two years.

2.1.2.2 CSA A23.2-14A

As a concrete prism test, CSA A23.2-14A [50] can be also used to assess the reactivity of both fine and coarse aggregates. A non-reactive coarse aggregate should be used for the assessment of reactivity of a fine aggregate and a non-reactive fine aggregate should be used for the assessment of reactivity of a coarse aggregate. The definition of non-reactive aggregates is same as in ASTM C 1293 (expansion less than 0.10% at 14 days during CSA A23.2-25A). When evaluating the reactivity of a fine aggregate, the grading of coarse aggregates is according to Table 2.7, and the fine aggregates are tested with the grading delivered to the laboratory. The casting and curing of specimens in CSA A23.2-14A is same as in ASTM C 1293. When the expansion of specimens is below 0.04% at one year, aggregates are classified as non-reactive; expansion is over 0.12% at one year, aggregates are reactive; expansion is in between 0.04% and 0.12% at one year, aggregates are moderately reactive.

Table 2.7 Grading requirement in CSA A23.2-14A.

Sieve Size		Mass %
Passing	Retained on	
20 mm	14 mm	33
14 mm	10 mm	33
10 mm	5 mm	33

The use of SCMs as a preventive measure of ASR is discussed in CSA A23.2-27A [51]. Changes of water-binder ratio and adjustment of alkali content are the same as described in CSA A23.2-25A. The effectiveness of a specific SCM is justified through the following criterion: the expansion of specimens containing a combination of the SCM and reactive aggregates must be below 0.04% at two years to limit ASR damage.

2.1.2.3 RILEM TC 106-3 (RILEM AAR-3)

RILEM TC 106-3 is the CPT method used in Europe. In this test [52], the aggregates fractions shall have a combination in mass proportions of 30% fine aggregates 0-4 mm, 30% 4-10 mm, and 40% 10-20 mm. The non-reactive fine or coarse aggregates are defined to have expansions less than 0.05% at 14 days in RILEM TC 106-2. The concrete mixture in this case shall be combined in the following way based on volume proportions: cement 14%, water 20%, fine aggregates 20% and coarse aggregates 46%. The concrete is cast with a cement content of 440kg/m^3, which is a little higher than in the ASTM and CSA tests. This results in a corresponding higher alkali level of the mixture at 5.5kg/m^3. The increased alkali content in the mixture compared to ASTM and CSA may also cause a higher expansion limit. RILEM TC 106-3 suggests a 0.05% expansion at one year for the non-reactive aggregates. According to FHWA [10], the use

of SCMs in RILEM will be introduced in RILEM ASR-7 which is not officially published yet to date.

2.1.2.4 Limitation of Concrete Prism Tests

A comparison of different CPT methods is summarized in Table 2.8. The concrete prism tests are generally considered the most accurate in predicting the field performance of aggregates. Thomas et al. [48] indicated that no aggregates so far which passed CPT (ASTM C 1293 and CSA A23.2-14A) test had caused ASR damage in concrete structures. In addition, the CPT methods are also broadly used to evaluate the effectiveness of both the SCMs [39, 48] and lithium compounds [48, 52] for mitigating ASR. Despite the reliable information that CPT provides, the CPT methods have one obvious disadvantage, the long period to run the test. The running time is one year for CPT without SCMs and lithium compounds and two years with SCMs and lithium compounds. The extremely time-consuming testing process sometimes largely limits the application of CPT methods when the reactivity of aggregates needs to be identified in a timely manner. Furthermore, Thomas et al. [48] and Ideker [20] reported two other problems of current CPT methods, which are the leaching of the alkalis due to the size effect and the reduction of expansion due to selection of non-reactive aggregates in the mixing. These problems may cause confusion about the aggregate reactivity when the aggregates are slowly reactive and the expansion at one year is near the limit 0.04% [53].

2.1.3 Accelerated Concrete Prism Test (ACPT)

To shorten testing time, a modified version of CPT, namely the accelerated concrete prism test (ACPT) has been examined by different research groups around the world. The biggest change in the ACPT over conventional CPT is the increase in exposure temperature (change from 38°C to 60°C). The elevated temperature could accelerate the reaction and boost the expansion of specimens at a shortened duration of 3 or 4 months. The ACPT was first proposed by Ranc and Debray [54] and since then has been of great interest. Although ASTM and CSA has yet to establish such standards for the ACPT (possibly because of insufficient experimental data), RILEM has started to develop a recommended ACPT method – RILEM AAR-4 [55] which has been used in some preliminary work on ASR in several participating countries of RILEM programs [17,56].

Since most of the work using ACPT tested limited sources of aggregates, the expansion limits are not consistent with each other and remains a topic of discussion among researchers. For instance, Ranc and Debray [54], Fournier et al. [57] reported a 0.04% expansion at three months as the limit of reactive aggregates, while DeGrosbois and Fontaine [58] suggested a 0.025% expansion at three months as the limit. Most recently, the results of Shayan's work [17] indicating a limit of 0.03% at 4 months would correctly classify a great majority of reactive aggregates tested. Although these ACPT methods were seen as a reasonable correlation with reliable CPT methods [17, 57, 59], the ACPT methods still face big challenges to the questions about their reliability. As Ideker et al. [20] showed, the elevated temperature will further worsen the leaching of

alkalis in samples, which could reduce the expansion significantly. In fact, the resulting reduction of expansion due to increased temperature in ACPT has been observed [20].

Table 2.8 Comparison of various CPT methods.

	ASTM C 1293	CSA A23.2-14A	RILEM TC 106-3
Water/cement ratio (mass)	0.42-0.47	0.42-0.45	0.45
Mixture alkalis (Na_2O eq.)	1.25%	1.25%	1.25%
Aggregate size (mm)	4.75-19	5-20	0-20
Cement Content(kg/m^3)	420±10	420±10	440
Bar size (mm)	75×75×275	75×75×275	75×75×250±50
Curing conditions	23℃, ≥95% RH for 24 hrs	23℃, 100% RH for 24 hrs	23℃, ≥90% RH for 24 hrs
Storage temperature	38℃	38℃	38℃
Initial reading	24 hrs	24 hrs	24 hrs
Criteria	>0.04% reactive <0.04% non-reactive (@1 year)	>0.12% highly reactive 0.04%-0.12% marginally reactive <0.04% non-reactive (@1 year)	>0.10% reactive 0.05%-0.10% potentially reactive <0.05% non-reactive (@1 year)

Another issue of ACPT is the selection of non-reactive aggregates in the mixing, which has been a problem in CPT as stated earlier. Based on the significant discrepancy [20, 60] found between CPT results and ACPT results for a wide variety of aggregates in the United States and Canada (i.e., Figure 2.2), researchers at the University of Texas state that ACPT is an insufficient, inappropriate, and inaccurate approach for the ASR evaluation [20].

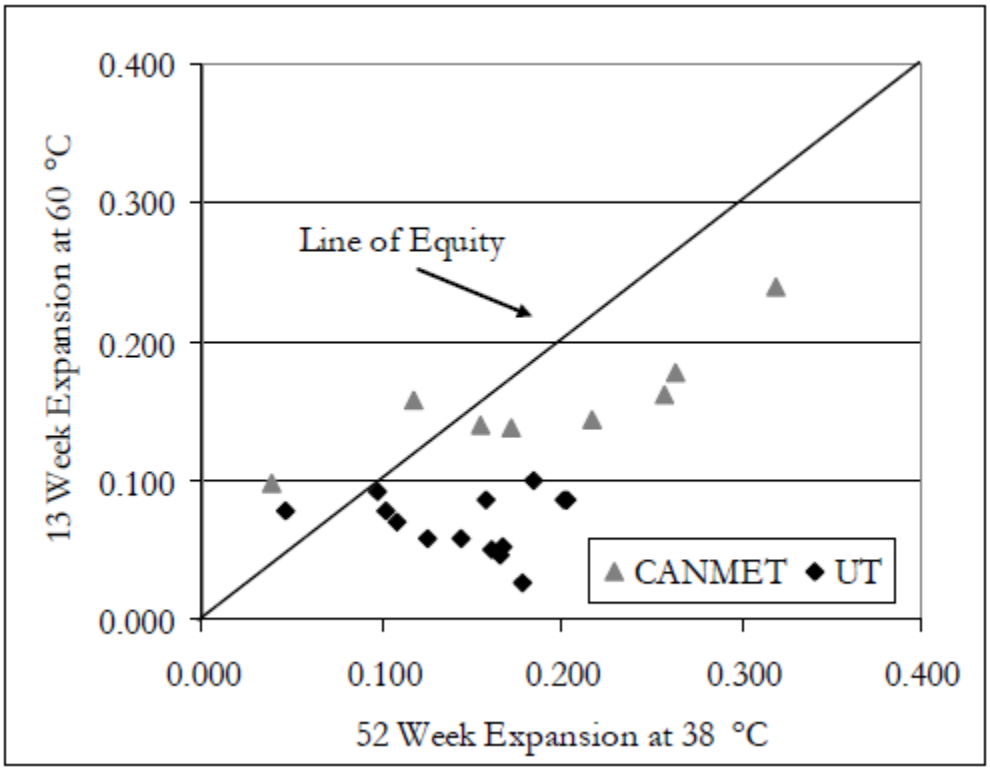

Figure 2.2 Discrepancy between ACPT results and CPT results reported by Ideker et al. [20].

2.1.4 Remarks on Expansion Test Methods

The most common laboratory tests for assessing the reactivity of aggregates based upon mortar and concrete expansion tests have been described in detail. Generally, the AMBT is fast, but overly strict to classify reactive aggregates. CPT can provide the most reliable results among all laboratory methods, but its long testing duration is not practical for the rapid screening of aggregates. ACPT has shown some encouraging results yet is still tainted by its unproved reliability. For all expansion methods, the correlation between the expansion measured and the degree of reaction and the potential for further reaction has been challenging to establish [61-63]. Given that advantages and

disadvantages exist for each method, test methods should be selected based on the particular project requirements.

Furthermore, the objective of expansion methods is to provide decision-makers information on aggregate reactivity, to determine the remedy actions necessary for existing structures, and provide preventive measures for new structures. Thus, the interpretation of expansion measurements and the limits by which alkali-reactivity is determined is a critical issue. Although different expansion limits have been suggested in different methods, it should be kept in mind that no single expansion limit is universally applicable and even for the same method, the interpretation of expansion could be different for varying concrete structure types or surrounding environments. CSA A23.2-27A [49] provides a systematic procedure to combine the expansion methods, as well as field examination/petrographic analysis with different environmental conditions and requirement of structure service life to determine what kind of preventive measures should be used for aggregates. Four levels of ASR risk are classified based on the expansion tests (AMBT or CPT) and surrounding environment of concrete structures. Then, five levels of prevention are decided based upon different level of ASR risk and expected service life of structure. Different preventive measures including rejection, decrease of alkali contents in cement, and use of SCMs and chemical admixtures are described according to the defined prevention level. Most recently, the FHWA proposed a series of protocols to mitigate ASR in existing and new concrete structures [10, 64]. The schematic steps for the preventive measures are similar as in CSA A23.2-27A except that FHWA uses a more detailed classification, based on categories provided in RILEM TC 191-ARP [41], in every step including one more class of aggregate reactivity (Table

2.6), two more in ASR risk (Table 2.9), one more in concrete environment (Table 2.9) and one more in structure type (Table 2.10). In this way, the aggregate reactivity can be related to risk for damage (which depends on the size of the concrete element and exposure conditions as seen in Table 2.11). Once the risk level has been defined, mitigation options are described, based upon the severity of consequences should ASR occur, which depends on the type of structure in which the aggregates will be used. There are two options available in FHWA's protocols, which are limiting the alkali content of the concrete and using SCMs. The details on how to adopt these two preventive measures are discussed in Table 2.12 and Table 2.13, respectively.

Table 2.9 Determination of ASR risk levels based on aggregate-reactivity class and size and exposure conditions [10].

Size and exposure conditions	Aggregate-Reactivity Class			
	R0	R1	R2	R3
Non-massive[1] concrete in a dry[2] environment	Level 1	Level 1	Level 2	Level 3
Massive[1] elements in a dry[2] environment	Level 1	Level 2	Level 3	Level 4
All concrete exposed to humid air, buried or immersed	Level 1	Level 3	Level 4	Level 5
All concrete exposed to alkalis in service[3]	Level 1	Level 4	Level 5	Level 6

[1]A massive element has a least dimension > 0.9 m

[2]A dry environment corresponds to an average ambient relative humidity lower than 60%, normally only found in buildings

[3]Examples of structures exposed to alkalis in service include marine structures exposed to seawater and highway structures exposed to deicing salts (e.g. NaCl) or anti-icing salts (e.g. potassium acetate, sodium formate, etc.)

Table 2.10 Structure classifications based on the severity of the consequences should ASR[†] occur [10].

Class	Consequences of ASR	Acceptability of ASR	Examples
S1	Safety, economic or environmental consequences small or negligible	Some deterioration from ASR is acceptable	▪ Non-load-bearing elements inside buildings ▪ Temporary structures (e.g. < 5 years) ▪ Small numbers of easily replaced elements ▪ Most low-rise domestic structures
S2	Some safety, economic or environmental consequences if major deterioration	Moderate risk of ASR is acceptable	▪ Most building and civil engineering structures ▪ Sidewalks, curbs and gutters ▪ Highway barriers ▪ Culverts ▪ Service-life < 40 years
S3	Significant safety, economic or environmental consequences if minor damage	Minor risk of ASR acceptable	▪ Pavements ▪ Rural, low-volume bridges ▪ Large numbers of precast elements where economic costs of replacement are severe ▪ Service life normally 40 to 75 years
S4	Serious safety, economic or environmental consequences if minor damage	ASR cannot be tolerated	▪ Major bridges ▪ Dams ▪ Tunnels ▪ Nuclear installations ▪ Structures retaining hazardous materials ▪ Critical elements that are very difficult to inspect or repair ▪ Service life normally > 75 years

[†]Note: this table does not consider the consequences of damage due to Alkali-Carbonate Reaction.

Table 2.11 Determination of various prevention levels based on ASR risk levels and classification of structure [10].

Level of ASR risk (Table 2.9)	Classification of structure (Table 2.10)			
	S1	S2	S3	S4
Risk Level 1	V	V	V	V
Risk Level 2	V	V	W	X
Risk Level 3	V	W	X	Y
Risk Level 4	W	X	Y	Z
Risk Level 5	X	Y	Z	ZZ
Risk Level 6	Y	Z	ZZ	††

††It is not permitted to construct a Class S structure (see Table 2.10) when the risk of ASR is level 6. Measures must be taken to reduce the level of risk in these circumstances.

Table 2.12 Minimum levels of SCM to provide various levels of prevention except ZZ [10].

Type of SCM	Alkali level of SCM (% Na_2Oe)	Minimum replacement level (% by mass)				
		Level W	Level X	Level Y	Level Z	Level ZZ
Fly ash ($CaO \leq 18\%$)	< 3.0	15	20	25	35	Table 2.13
	3.0 – 4.5	20	25	30	40	
Slag	< 1.0	25	35	50	65	
Silica Fume† ($SiO_2 > 85\%$)	< 1.0	2.0 × KGA	2.5 × KGA	3.0 × KGA	4.0 × KGA	

†The minimum level of silica fume (as a percentage of cementing material) is calculated on the basis of the alkali (Na_2Oe) content of the concrete contributed by the portland cement and expressed in kg/m^3 (KGA in Table 2.12).

Table 2.13 Two preventive measures corresponding to levels of prevention Z and ZZ[10].

Prevention Level	SCM as sole prevention	Limiting concrete alkali content plus SCM	
	Minimum SCM level	Maximum alkali content, kg/m^3	Minimum SCM level
Z	SCM level shown for Level Z in Table 2.12	1.8	SCM level shown for Level Y in Table 2.12
ZZ	Not permitted	1.8	SCM level shown for Level Z in Table 2.12

In conclusion, the characterization of aggregate reactivity and corresponding preventive actions are complicated procedures, and the expansion methods cannot solely serve the purpose due to the inherent limitations discussed in this section. Therefore, it is of critical importance to explore a new testing method which can provide accurate and reliable results in a reasonable time scale.

2.2 Acoustic Techniques for Cementitious Materials

With a long successful history in crack detection for metallic materials, acoustic techniques have been widely used in recent decades for the assessment of damage in cement-based materials. The acoustic techniques fall into two categories according to the principal assumption of material constitutive laws; generally termed linear acoustic techniques and nonlinear acoustic techniques.

2.2.1 Linear Acoustic Techniques

The underlying assumption of all linear acoustic techniques is that the elastic modulus of materials remains independent of the body deformation. Therefore, the frequency of probing signal is assumed not to change throughout the propagation. The following sections discuss several linear acoustic techniques used for damage assessment of materials.

2.2.1.1 Pulse-echo Method

The pulse-echo method characterizes flaws or inclusions in materials by detecting the echo of pulsed stress waves. Acoustic theory states that the incident signal will be reflected back on an interface between two media which have different acoustic impedance. When the material contains forms of damage, such as voids or flaws, the medium of wave propagation cannot be considered the same any more and some of the acoustic energy is reflected at a location of flaws. It is obvious that the larger the reflecting surface (i.e., the size of crack or inclusion) the more acoustic energy will be echoed back. Therefore, the formation and relative size of flaws may be measured by the strength of echoed signals. The principle of pulse-echo methods is easily understood, but it should be noted that there exists a limit for the detectable size of flaws in this technique [65]. It may be a solution to increase the frequency of signal to get a smaller size resolution. However the attenuation effect of medium on wave propagation will be significantly increased given a higher frequency signal which may decrease the signal-noise ratio in practice.

2.2.1.2 Pulse-velocity Method

The pulse-velocity method refers to the measurement and comparison of phase velocity of a pulsed stress wave propagating a certain distance along defined samples [66]. In this method, a transducer emits a probing signal which travels through the sample and is caught by a received transducer. The travel time is obtained by observation of the phase difference of incident signal and received signal, and thus the phase velocity can be calculated by the division of path length over the travel time. If there is a flaw or crack inside the material, the wave may be delayed and cause a decrease in the phase velocity. Unfortunately, the pulse-velocity method was found to have low sensitivity to early-damage of concrete materials. For example, phase velocities only began to have a substantial change when the loading reached approximately 80% of the compressive capacity of concrete [67].

2.2.1.3 Pulse-amplitude Method

Due to the attenuation effect of material, the amplitude of probing signals will be decreased with the propagation throughout samples. The increase of this attenuation effect because of the presence of material damage is the theoretical background of the pulse-amplitude method used to detect defects in cementitious materials. Although the pulse-amplitude method could be more sensitive to damage state of materials [68], the testing results are highly dependent on the coupling condition between transducers and samples which make the reliability of the pulse-amplitude method questionable [69].

2.2.1.4 Limitation of Linear Acoustic Techniques

It has been shown that the linear acoustic techniques are generally simple from an operational perspective, and the analysis remains within the time domain which reduces computationally inefficient signal processing. Nevertheless, linear acoustic techniques still have their problems, such as their sensitivity and repeatability. More importantly, the assumption of linear constitutive relation in linear acoustic techniques is typically not true for heterogeneous materials like concrete and mortar, particularly with damage in the microstructure.

2.2.2 Nonlinear Acoustic Techniques

To more accurately describe the heterogeneous nature of cement-based materials and better capture the progress of material damage, the nonlinear terms in the constitutive relation of materials should be taken into account. Different nonlinear acoustic phenomena take place as the stress waves propagate throughout the specimens including the occurrence of higher order harmonics, modulation effects of two waves, and shift of the resonance frequency of samples. The nonlinear acoustic techniques introduced below are developed on the basis of these nonlinear acoustic phenomena.

2.2.2.1 Second Harmonic Generation Method

The theoretical study of harmonic generation can be traced back three decades ago. Buck et al. [70] and Richardson [71] studied the case of the travel of a monochromatic sinusoidal wave across an unbounded planar interface and concluded that the opening and closing of the interface was the origin of nonlinearity and then induced

the generation of a second harmonic wave. Sutin and Nazarov [72] expanded their work to the case of unbounded rough interfaces and were also able to produce additional harmonics. The second harmonic generation method was then rapidly applied in the assessment of fatigue damage in various materials [73-77].

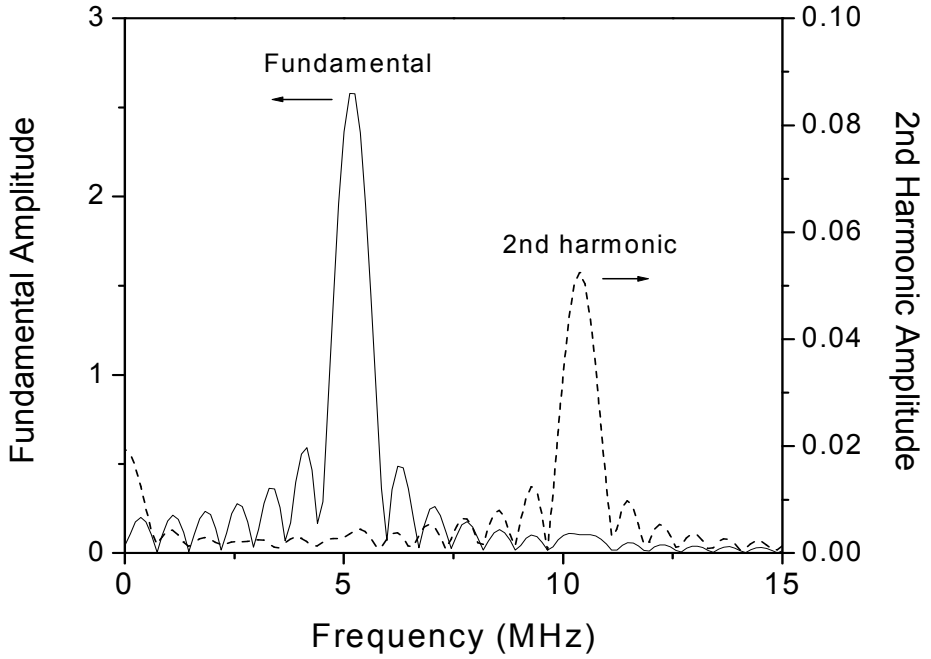

Figure 2.3 Second harmonic occurring in nonlinear ultrasonic experiments for metallic materials [29].

Due to the nonlinearity intrinsically present in materials and instruments, it was difficult to accurately measure the second harmonic component caused by fatigue damage in a quantitative manner. Recently, a novel experimental procedure was successfully developed to isolate the damage nonlinearity from the measurement system nonlinearity [29-31]. Both longitudinal waves and Rayleigh surface waves were employed in this research and the measured second order nonlinear parameter for fatigue damage of alloy materials had good agreement with each other.

2.2.2.2 Wave Modulation Method

In the light of second harmonic generation method, Sutin and Nazarov [72] and Van Den Abeele et al. [78] further suggested that two waves with different frequency would interact with each other when they travel across a nonlinear material within the same time frame. These interactions were termed the wave modulation effect. If the second harmonic could be considered as the modulation effect of a mono-frequency signal itself, the modulation result of dual-frequency signals is easily understood, i.e., the generation of sidebands at the location of summation and subtraction of incident frequencies. In practical experiments, the frequency difference of two incident waves was fairly large to avoid the blur effect of harmonics on the observation of sidebands. Thus the high frequency signal was normally an ultrasound and the low frequency signal could be induced either by a continuous wave source (e.g., a shaker) [79] or an impact vibration (e.g., an instrumented hammer) [80].

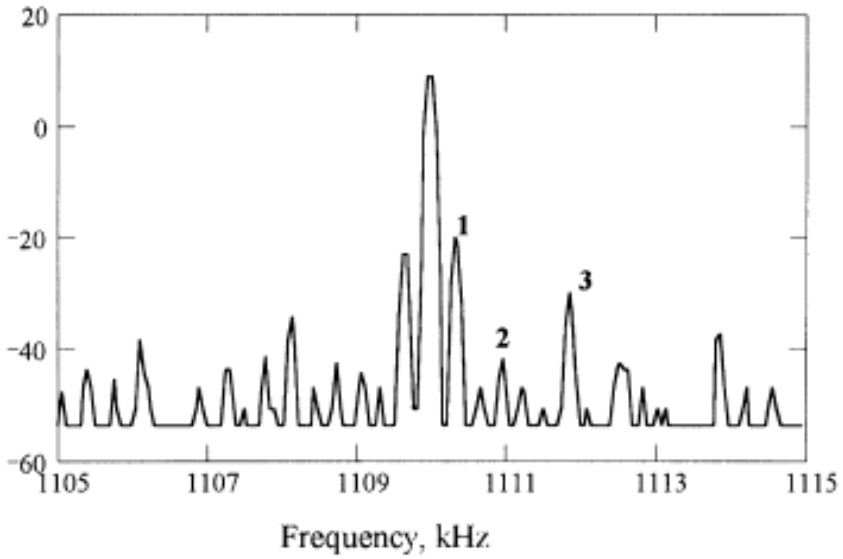

Figure 2.4 Wave modulation effect shown in nonlinear ultrasonic experiments for steel samples [32].

Much research has been conducted in recent years on the application of the wave modulation method. For example, Donskoy et al. [32] developed an experimental setup with impact modulation techniques to detect fatigue cracks in steel samples. Zumpano and Meo [81] used two continuous signal sources to measure the sidebands caused by impact damage on a sandwich plate. Van Den Abeele [78, 82] applied the wave modulation methods to discern damage of varying materials including Plexiglas, sandstone, cracked automobile parts and cementitious roofing tiles.

2.2.2.3 Resonance Frequency Shift Method

In linear theory, the resonance frequency of samples is determined by their material properties (elastic modulus and density) and dimension, regardless of the excitation level of vibration. However, in nonlinear acoustics the resonance frequency is not independent of strain excitation and may shift during increased excitations. Recent research [83-87] indicated that classical nonlinear theory [88], which attributes the nonlinearity to solely anharmonic terms in constitutive relations, may not sufficiently describe the complicated nonlinear mechanisms of brittle materials like rock and concrete. Additional terms related to hysteresis and discrete memory should be incorporated in the constitutive relations of materials. Van Den Abeele [85] found that the shift of resonance modes was linearly proportional to strain excitation for the hysteresis effect while having a quadratic relation of strain excitation for the anharmonic effect. The shift of resonance mode was mostly contributed by the hysteresis effect, with lesser contributions by the anharmonic effect because the strain excitation in the resonance displacement method was very small (far less than unity). The resonance

displacement method has been successfully used to diagnose different damage forms in rocks and concrete [28, 89, 90].

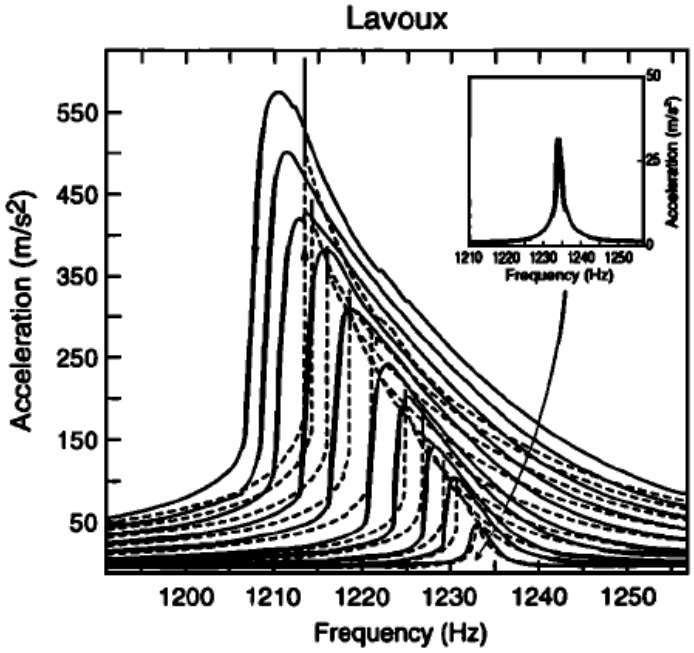

Figure 2.5 Displacement of resonance frequency shown in nonlinear acoustic experiments for rock samples [89].

2.3 Advantages of Nonlinear Acoustic Techniques

It was mentioned that experiment techniques based on the principle of nonlinear acoustics are much more sensitive to the material degradation than experimental techniques based upon linear acoustics. The change of damage parameters defined in nonlinear acoustic techniques is at least ten times the change of linear parameters responsive to the development of material damage [28, 76]. For example, Figure 2.6 shows the comparison between the change of nonlinearity parameters and linear parameters measured for the fatigue in ABS polymer materials [76]. It is seen that nonlinearity parameters increase about 20 times while the variation of linear parameters is about 20%. Another example is

shown in Figure 2.7, which indicates that the change of nonlinearity parameters is as high as 100 times the change of linear parameters with respect to the progressive cracking in concrete samples subjected to consecutive loading steps. It is thus a significant advantage of these nonlinear acoustic techniques when an early characterization of material damage is in priority need, such as in the case of ASR.

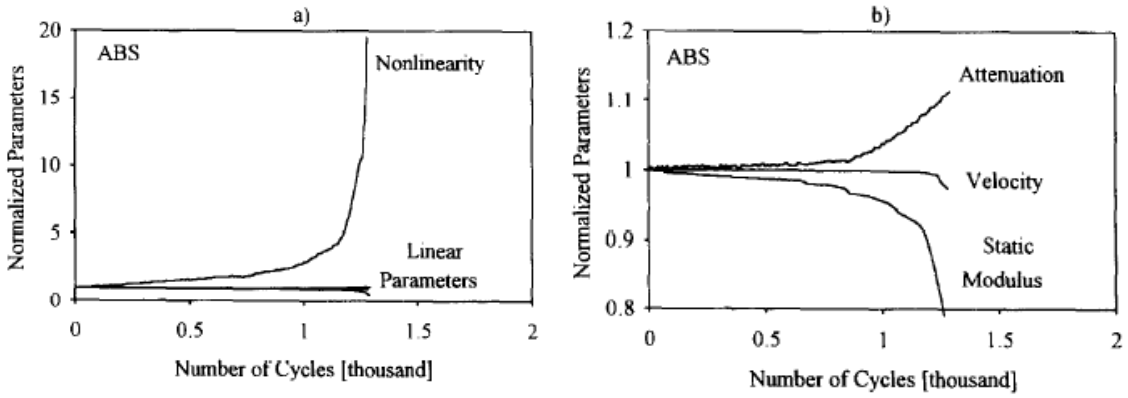

Figure 2.6 Variation of nonlinear and linear parameters with respect to the fatigue in ABS polymer [76].

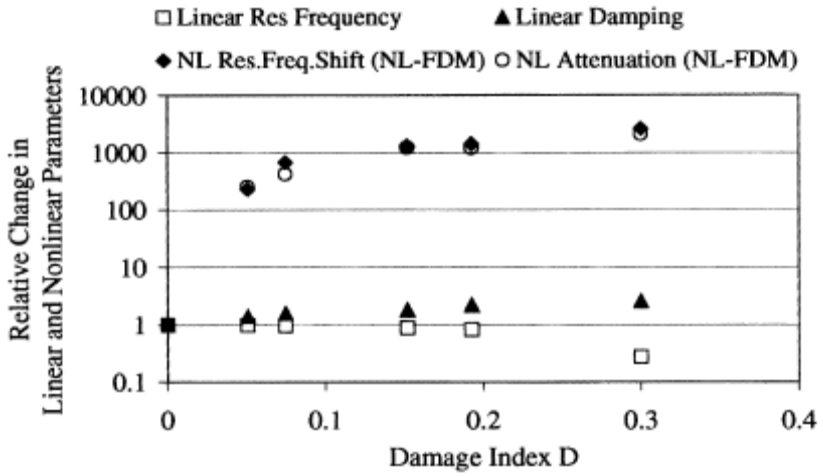

Figure 2.7 Variation of nonlinear and linear parameters as a function of damage due to progressive loadings [28].

2.4 ASR and Acoustic Techniques

Although acoustic or ultrasonic techniques have been widely used for the deterioration assessment of cement-based materials, little research utilizing acoustic techniques have been conducted for the assessment of ASR-induced damage, to the best of author's knowledge. The majority of published research describes the application of linear acoustic methods such as the pulse velocity method and attenuation measurement method for the assessment of ASR damage in drilled cores, fragments from concrete structures and laboratory specimens [23-25]. However, as stated earlier, the sensitivity and reliability of linear acoustic methods are still a concern for damage evaluation of cementitious materials. Actually, the decreased measurement of pulse velocity due to ASR damage has a non-negligible variation among different research. For instance, Bengey [24] observed a loss of 24% of pulse velocity with a sample expansion of 0.2%, while Ahmed et al. [23] measured the same loss with a sample expansion of 0.1%. In Saint-Pierre's work [25], only a highly-reactive aggregate and a non-reactive aggregate were examined by the attenuation measurement. The obvious difference of the reactivity of two studied aggregates could also be identified well by conventional expansion methods, which makes the attenuation measurement little advantageous.

Recently, Chen et al. [91] applied the nonlinear modulation method in the differentiation of ASR-damaged mortar samples and control samples. Their work showed the promising potential of nonlinear acoustic techniques for ASR damage assessment but was only preliminary work which did not quantitatively track the progress of ASR damage and was limited to few mortar samples. Therefore, it is recommended that further research develop a more robust and reliable acoustic technique based on nonlinear theory

to quantify the progression of ASR damage for different aggregates with varying reactivity.

CHAPTER 3

MATERIALS AND EXPANSION TESTS

3.1 Materials

The materials used in the research are described in this chapter, including aggregates, cement and SCMs. A total of ten different fine aggregates, three different coarse aggregates, one cement and one fly ash were used in the experiments. The mineralogy and contents of materials are concluded in this section.

3.1.1 Fine Aggregates

A total of ten different sands were used in the experiments. Table 3.1 provides the source and mineralogy of each. These sands were graded according to AASHTO T 303 when used for mortar samples, where a constant fineness modulus of 2.9 was therefore specified for all sands except F9. F9 was used as delivered in mortar samples (a fineness modulus of 2.35) due to the insufficient larger size particles. The specific gravity of these sands is listed in Table 3.2.

3.1.2 Coarse Aggregates

Three coarse aggregates were used in the experiments. The source and mineralogy of these coarse aggregates are presented in Table 3.3. The specific gravity of these coarse aggregates is listed in Table 3.4.

Table 3.1 Mineralogy and source of fine aggregates.

ID	Mineralogy	Source
F1	Mixed quartz/chert/feldspar sand	El Paso, TX
F2	Mixed quartz/clay/feldspar sand	Moscow, PA
F3	Mixed quartz/amphibole/feldspar sand(crushed from C1)	Augusta, GA
F4	Mixed quartz/chert/feldspar sand	Gadsden, AL
F5	Mixed quartz/biotite mica/feldspar/ amphibole sand	Talbotton, GA
F6	Mixed quartz/amphibole/feldspar sand (crushed from C2)	Junction City, GA
F7	Mixed dolostone/calcite sand (crushed from C3)	Adairsville, GA
F8	Quartz sand	North Augusta, SC
F9	Quartz sand (crushed)	Junction City, GA
F10	Quartz sand	Lithonia, GA

Table 3.2 Specific gravity and absorption of fine aggregates.

ID	SG_{bulk}	SG_{SSD}	$SG_{apparent}$	Absorption (%)
F1	2.565	2.592	2.635	1.03
F2	2.66	2.69	2.74	1.16
F3	2.575	2.608	2.663	1.28
F4	2.558	2.587	2.638	1.17
F5	2.766	2.782	2.810	0.56
F6	2.715	2.742	2.790	0.99
F7	2.800	2.814	2.840	0.45
F8	2.607	2.620	2.643	0.53
F9	2.620	2.631	2.649	0.42
F10	2.628	2.635	2.648	0.33

Note: Data of F2, F5 and F9 were from coarse aggregates. Data of F4, F5, F7, F8 and F9 were provided by Mandi Reinshagen at Georgia Department of Transportation. Data of F2 was provided by Dr. Jason Ideker at Oregon State University.

Table 3.3 Mineralogy and source of coarse aggregates.

ID	Mineralogy	Source
C1	Mixed quartz/amphibole/feldspar	Augusta, GA
C2	Mixed quartz/amphibole/feldspar sand	Junction City, GA
C3	Mixed dolostone/calcite	Adairsville, GA

Table 3.4 Specific gravity and absorption of coarse aggregates.

ID	SG_{bulk}	SG_{SSD}	$SG_{apparent}$	Absorption (%)
C1	2.625	2.645	2.680	0.75
C2	2.741	2.754	2.777	0.47
C3	2.814	2.823	2.841	0.34

Note: Data were provided by Mandi Reinshagen at Georgia Department of Transportation.

Table 3.5 Chemical oxide analysis and Bogue potential composition of cement.

Oxide/Phase	Wt(%)	Oxide/Phase	Wt(%)
Silicon Dioxide (SiO_2)	20.13	Phosphorus Pentoxide (P_2O_5)	0.12
Aluminum Oxide (Al_2O_3)	5.23	Strontium Oxide (SrO)	0.20
Iron Oxide (Fe_2O_3)	3.15	Barium Oxide (BaO)	0.03
Calcium Oxide (CaO)	61.23	Sulfur Trioxide (SO_3)	3.69
Magnesium Oxide (MgO)	3.61	Loss on Ignition	1.13
Sodium Oxide (Na_2O)	0.25	Insoluble Residue	N/A
Potassium Oxide (K_2O)	0.88	Tricalcium Silicate (C_3S)	46.11
Total Alkali (Na_2O_{eq})	0.83	Tricalcium Aluminate (C_3A)	8.52
Titanium Oxide (TiO_2)	0.21	Dicalcium Silicate (C_2S)	22.93
Manganic Oxide (Mn_2O_3)	0.15	Tetracalcium Aluminoferrite (C_4AF)	9.59

3.1.3 Portland Cement

The cement used in ABMT methods met ASTM C 150, as required, with no additional requirement for the alkali content. For the cement used in CPT methods, the alkali content is required to be 0.9±0.1% Na_2O_{eq}. Thus, for consistency, a typical Type I cement with a high alkali content was used in both sets of experiments. The cement alkali equivalent and composition was verified by chemical analysis performed by Wyoming

Analytical in Golden, Colorado. Table 3.3 presents chemical oxide analysis and Bogue potential composition of the cement.

3.1.4 Fly Ash

A Class C fly ash following Specification ASTM C 668 was used in the experiments. The chemical analysis of this fly ash is shown in Table 3.4. The sum of the silicon, aluminum, and iron oxides was 60.77%.

Table 3.6 Chemical oxide analysis of fly ash.

Oxide	Wt(%)	Oxide	Wt(%)
Silicon Dioxide (SiO_2)	35.47	Titanium Oxide (TiO_2)	1.41
Aluminum Oxide (Al_2O_3)	18.38	Manganic Oxide (Mn_2O_3)	0.03
Iron Oxide (Fe_2O_3)	6.92	Phosphorus Pentoxide (P_2O_5)	1.27
Calcium Oxide (CaO)	25.01	Strontium Oxide (SrO)	0.39
Magnesium Oxide (MgO)	5.71	Barium Oxide (BaO)	0.71
Sodium Oxide (Na_2O)	1.95	Sulfur Trioxide (SO_3)	1.89
Potassium Oxide (K_2O)	0.50	Loss on Ignition (LOI)	0.36

3.2 Sample Preparation

The cast and curing of mortar bar samples conformed to AASHTO T 303 [34]. Prior to the mixing, fine aggregates were dried in an oven for 12 hours to remove any moisture. A planetary (Hobart N-50) mixer was used for the mixing, as shown in Figure 3.1. The molds filled with mortar were sealed in a plastic container under sufficient humidity for the next 24 hours, as shown in Figure 3.2. After demolding, the samples were stored in water in a sealed container at 80°C. After another 24 hours, the zero reading of sample length was performed using a comparator (Humboldt), as seen in

Figure 3.3. Samples were then placed in a 1N NaOH solution at 80°C as seen in Figure 3.4 and the subsequent readings of mortar bar length were conducted periodically.

Figure 3.1 A planetary mixer for the casting of mortars.

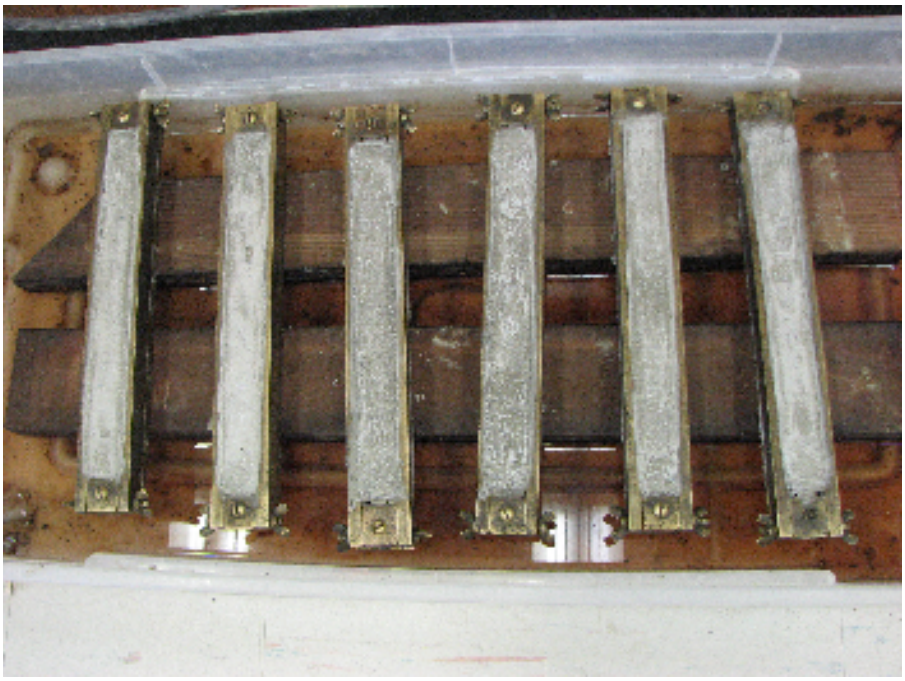

Figure 3.2 Molds for mortar samples in a humid container.

Figure 3.3 Zero reading of mortar sample length.

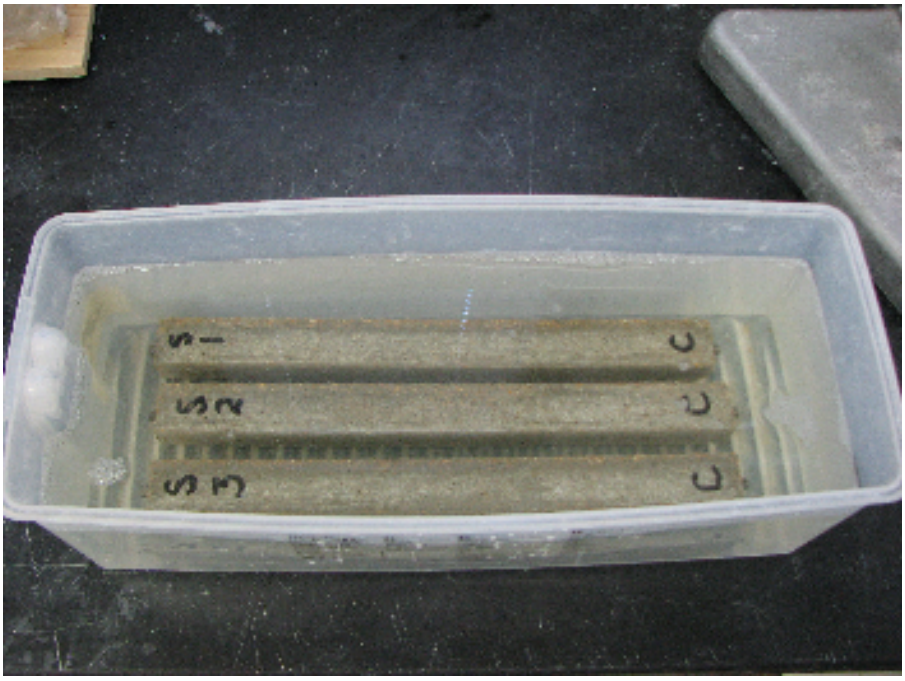

Figure 3.4 Mortar samples in NaOH solution to accelerate ASR.

The casting and curing of concrete prism samples were done in compliance with ASTM C 1293. (There is no AASHTO standard currently for concrete prism test.) Three

aggregates, F1, C1 and C2, were examined in the concrete prism tests. For the testing of reactive aggregate F1, coarse aggregate C3 was used as the non-reactive aggregate. For the testing of reactive aggregates C1 and C2, fine aggregate F10 served as the non-reactive aggregate. A high shear mixer (Eirich R08W) was used for the concrete mixing, as shown in Figure 3.5. After demolding, concrete prism samples were placed on the plastic pads in a sealed plastic bucket, which were filled with water on the bottom as shown in Figure 3.6. The zero reading was taken right after demolding and then samples were stored in an environment chamber at 38°C for the test duration. Prior to each length measurement, concrete prism samples were placed in a fog room at 21°C for 16 hours.

Figure 3.5 Mixer for the casting of concrete prisms.

Figure 3.6 Concrete prisms in a plastic container.

3.3 Expansion Results of Accelerated Mortar Bar Tests

3.3.1 Effect of Out-of-exposure Time

AMBT standards state that samples should be placed back to the NaOH solution immediately after the expansion measurements. But it will be seen in Chapter 7 and Chapter 8 that samples used for the nonlinear acoustic techniques are actually out of the NaOH exposure for a while during each test procedure. First these samples sit in an ambient environment for about 30 minutes to minimize the effect of temperature difference between the storage environment (80°C) and the test environment (room temperature). The acoustic tests additionally take about 15 minutes to be completed. Thus totally these samples for nonlinear acoustic techniques need a 45 minutes out-of-exposure time.

Since the AMBT expansion tests in our experiments are conducted with the acoustic tests in a time-parallel manner, samples used for AMBT measurements have to wait for samples used for acoustic techniques during each test procedure. Hence, samples for expansion measurements in our experiments actually do not strictly follow the AMBT standards, and instead have a out-of-exposure time of 45 minutes.

To observe the effect of the out-of-exposure time on the AMBT expansion results, a comparison between two groups of samples is carried out. The two groups of samples were both cast with aggregate F1 and other parameters for mix design were the same as well. The first group of samples strictly followed AASHTO T 303, and the second group of samples underwent a 45-minute out-of-exposure time intentionally. The expansions were measured periodically and the results were shown in Figure 3.7. It is obvious that the expansion behavior between the two sets of samples is nearly the same. Hence, the effect of out-of-exposure time in our experiments can be considered negligible.

3.3.2 AMBT Results

The 14-day expansion results in AMBT tests for aggregates F1-F10 are presented in Figure 3.8. The *x*-axis represents the exposure time of mortar samples in the NaOH solution. The *y*-axis represents the expansion of mortar samples. For each aggregate, the average expansions of three specimens are plotted in Figure 3.8. Standard deviation bars are also included for each average. Two horizontal dash lines at 0.1% and 0.2% in the plot refer to the threshold values for the aggregate reactivity stated in AMBT specifications.

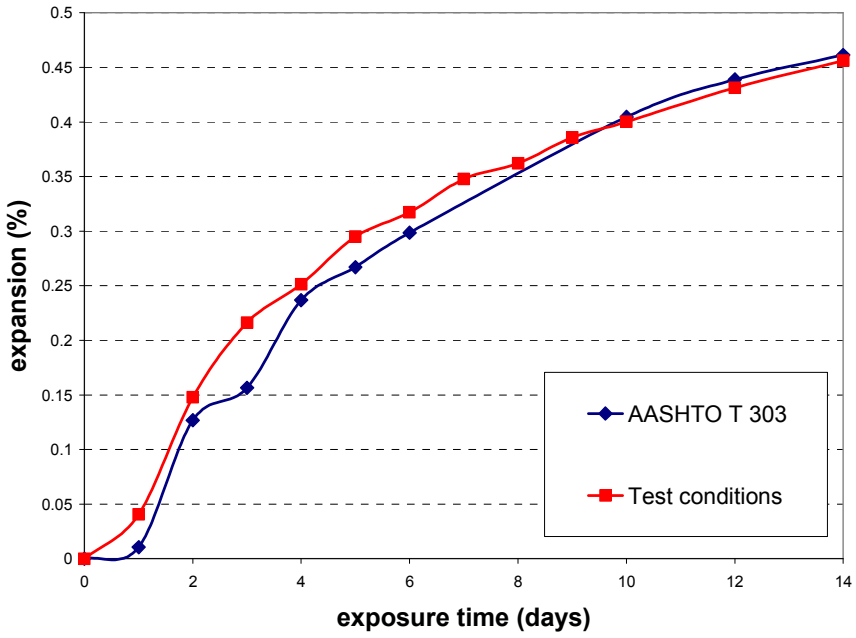

Figure 3.7 Comparison of expansion of mortar samples (aggregate F1) under standard AASHTO T 303 and acoustic experiment test conditions.

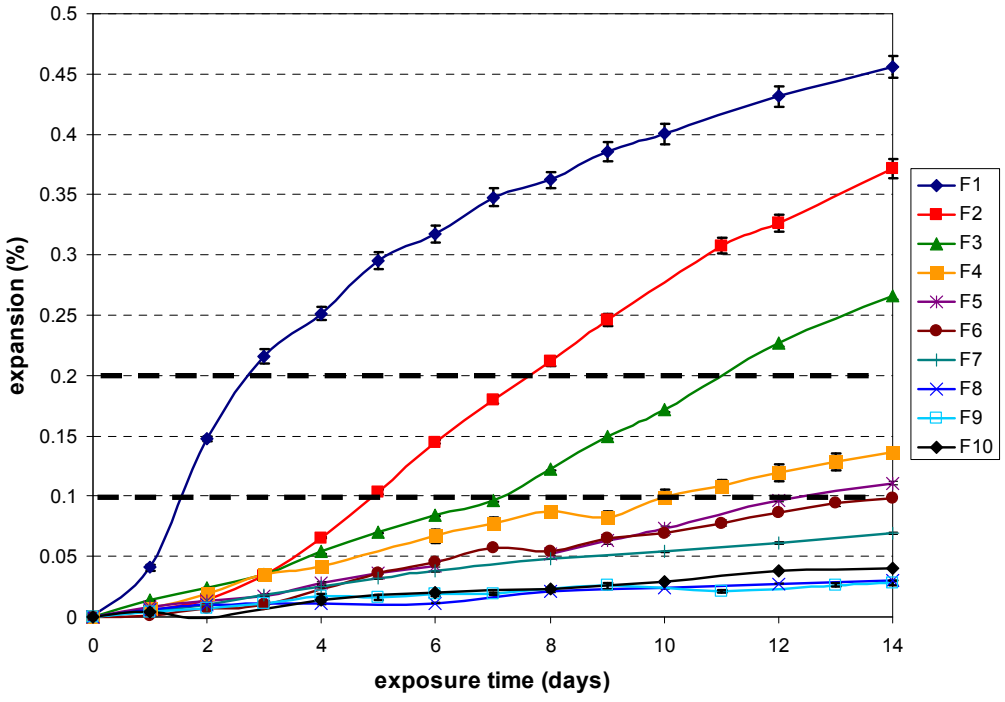

Figure 3.8 AMBT expansion results for aggregates F1-F10.

It is seen that aggregates F1-F3 are clearly highly reactive with an expansion well beyond 0.2% at the end of 14 days. Aggregates F4-F6 are considered as moderately reactive since their 14-day expansion values fall between 0.1% (or very close to 0.1%) and 0.2%. Aggregates F7-F9 are considered to have innocuous behaviors because the expansions are less than 0.1% at the end of 14 days.

Figure 3.9 presents the comparison of AMBT expansion results for aggregate F1 with and without the Class C fly ash specified previously. The fly ash was blended in cement with a 20% replacement rate. For the highly reactive aggregate F1, the expansion of specimens decreases 70% with the introduction of fly ash. However, a greater dosage of the Class C ash or the use of a Class F ash would be necessary to mitigate the expansion of aggregate F1 in practice, based upon data in Figure 3.9.

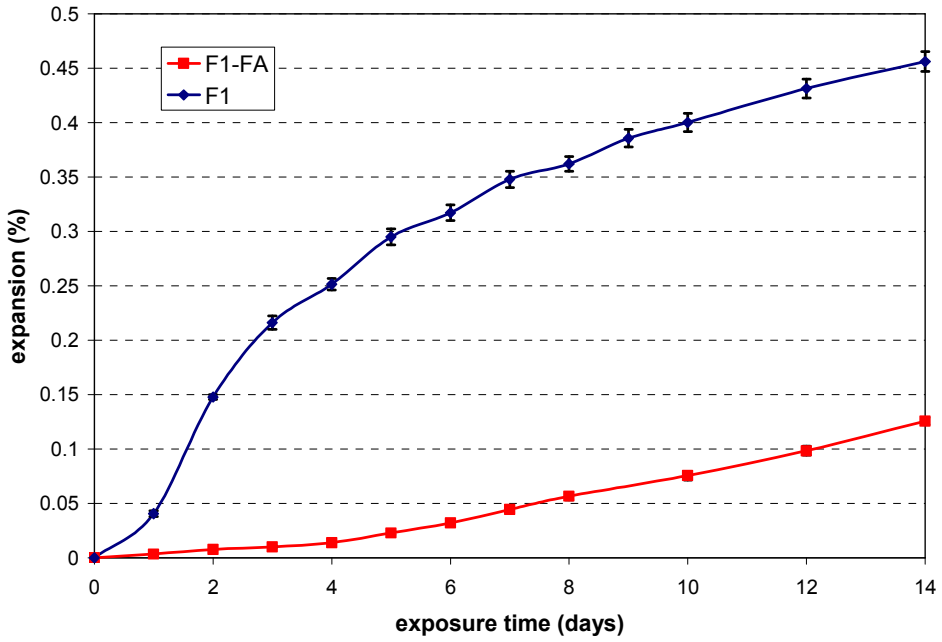

Figure 3.9 AMBT expansion results for aggregate F1 with and without fly ash.

3.4 Expansion Results of Concrete Prism Tests

The one-year expansion results of CPT tests for aggregates F1, C1 and C2 are presented in Figure 3.10. The average expansion is plotted and standard deviations are also included. The threshold values for the aggregate reactivity stated in CPT specifications are indicated by two horizontal dash lines at 0.04% and 0.12%, respectively.

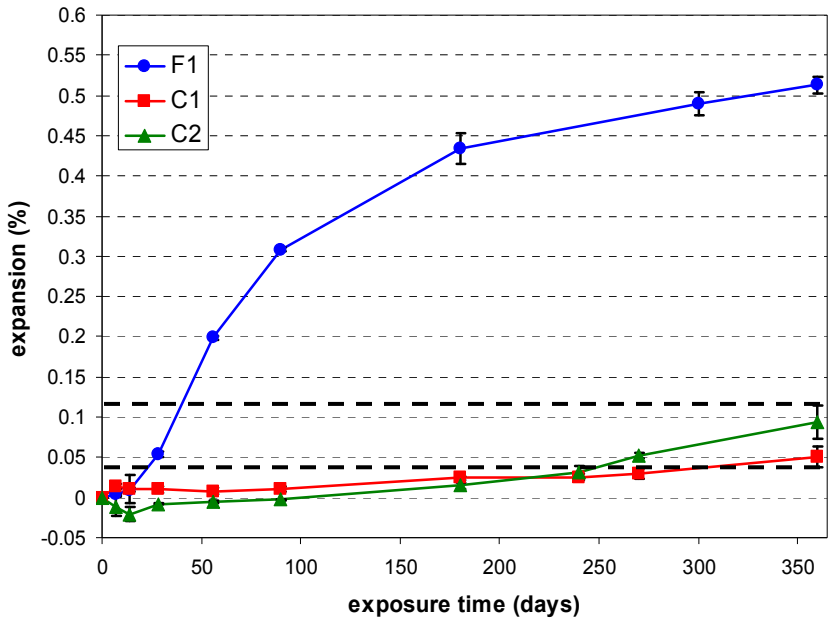

Figure 3.10 CPT expansion results for aggregates F1, C1 and C2.

It is seen in Figure 3.10 that the CPT expansion of aggregate F1 rapidly exceeds 0.12% in two months, indicating its strong reactivity consistent with the previous AMBT expansion result. The CPT expansion of aggregate C1 is marginally over 0.04% at the end of 12 months while the CPT expansion of aggregate C2 reaches nearly 0.1% at the end of 12 months. It is noteworthy that the relative reactivity of coarse aggregates C1 and

C2 indicated by the CPT measurements is opposite to what is reflected by the corresponding fine aggregates (F4 and F6) in the previous AMBT measurements.

CHAPTER 4

PETROGRAPHIC ANALYSIS

4.1 Experimental Equipments and Procedure

As introduced in Chapter 1, petrographic analysis is a supplemental tool for the ASR characterization in addition to expansion methods. Accompanying petrographic analysis is thus carried out in the research parallel to AMBT and acoustic measurements to provide direct image evidences of progressive ASR damage.

A method of sample preparation for the mortars was developed which would retain, as much as possible, any ASR gel formed, while avoiding the introduction of cracks or other artifacts, as is common with many methods which require drying or exposure to vacuum. Such care was necessary so that the damage induced from ASR could be clearly examined and compared to results of expansion measurements and developed nonlinear acoustic techniques. Thus, the samples cast for microscopy were cut to a length of ~1.25cm using a low speed saw (Figure 4.1) and ethanol as a lubricant. The microscopy specimens were then polished on a grinder/polisher (Figure 4.2) down to 600 grit size with water, such that the surface was highly polished and the aggregate clearly visible. The polished samples were then subjected to the same curing and aggressive exposure regimen as the samples prepared for expansion and acoustic techniques (i.e., AMBT by AASHTO T303/ASTM C 1260 conditions).

Prior to imaging, the samples were gently wiped with a damp cloth. When necessary, the imaging surface was polished for ~30 seconds at 600 grit. Digital images

(1600 by 1200 pixels) of the surfaces were taken at different locations on each specimen using a stereomicroscope (Leica MZ6) at magnifications of 40X and 80X (Figure 4.3).

Figure 4.1 A low-speed saw used for cutting samples.

Figure 4.2 A grinder used for polishing samples.

Figure 4.3 A stereomicroscope, with an indexible stage, for petrographic analysis.

Imaging was carried out at the same specimen locations using an indexible stage, allowing characterization of ASR damage over the exposure period. Thus, the extent of the formation of alkali-silica gel, aggregate/paste debonding, aggregate degradation, crack initiation and crack propagation at the same location were studied through the repeated imaging.

The sample preparation and imaging methods were developed to minimize the introduction of artifacts (e.g., due to drying) and to minimize perturbations of the mortar composition and structure, such that the progressive damage occurring in the mortar could be imaged over time. However, some alterations to the material and damage patterns may have occurred, despite the considerations described in this section. For example, due to the nature of polishing process itself, some friable or water-soluble material could have been removed. Also, by exposing the aggregates at the surface of the

mortar, the conditions of restraint were changed and may, thus, affect cracking patterns. For example, the presence of aggregates at the free surfaces may decrease the amount of aggregate cracking in favor of increased interfacial and paste cracking. Overall, despite these concerns, the petrographic imaging methodology described here is believed to be relatively successful in capturing the progression of ASR damage occurring in mortars during AMBT.

4.2 Petrographic Results

As stated earlier, the petrographic images were taken for the same samples at certain intervals through a duration of 14 days. Figure 4.4 presents petrographic images of a mortar sample cast with aggregate F1 at six different ages. Here day 0 refers to the initial day of the test (i.e., day of casting), when the sample was yet not placed into the NaOH solution. No substantial material degradation is found in Figure 4.4a, indicating an intact condition for the sample at day 0, as expected. After two days of exposure, when expansion measured 0.148%, ASR has begun to occur and the initial reaction product – ASR gel – is found between the aggregate and cement paste, as indicated by the arrow in Figure 4.4b. The early formation of ASR also validates the high reactivity of aggregate F1. Presumably, the ASR gel expands, and microcracks are apparent in the paste and debonding between the paste and aggregate is evident. For example, the initiation of a microcrack is seen in Figure 4.4c (the corresponding expansion at that age is 0.252%) on the same region where ASR gel was seen in Figure 4.4b. Figure 4.4d-f further show that the microcrack occurring on day 4 (Figure 4.4c) grows (becomes wider) when the sample receives progressive exposure in the NaOH solution. Correspondingly, the expansions

measured increased with the exposure time, which were 0.348% on day 7, 0.400% on day 11 and 0.456% on day 14. Another microcrack also initiates and grows wider on the upper left of petrographic images in Figure 4.4d-f. It is interesting to note that the color of an aggregate particle in Figure 4.4 changes over time, particularly during the first 4 days. The reason for the color change is not yet determined, but may be related to changes in the composition resulting from the high temperature, alkaline exposure.

Figure 4.5 shows a set of petrographic images for a mortar cast with aggregate F4. For comparison with the image for F1, the previous AMBT results showed that the expansion of aggregate F4 was only 0.02% when the expansion of aggregate F1 exceeded the 0.1% threshold after 2 days of exposure. While the expansion of aggregate F4 exceeded 0.1% at the end of 11 days, the corresponding expansion of aggregate F1 was as much as 0.4%. The AMBT results obviously indicated that aggregate F4 was less reactive than aggregate F1. As a result, ASR damage should occur in the sample cast with aggregate F4 later than in the sample cast with aggregate F1. The slower rate of ASR for aggregate F4 is supported by the petrographic images shown in Figure 4.5. A microcrack due to ASR is first apparent at day 6 as seen in Figure 4.5c when the corresponding expansion was 0.067%. The growth of this microcrack and initiation of a new microcrack are also shown in Figure 4.5d-f. The expansions measured at different intervals kept increasing and were included in Figure 4.5. It is also observed that an aggregate (in a region of interest at center-left of the images) disintegrates and grows more porous with increasing exposure periods; this is likely a weathered cherty particle, which is particularly susceptible to material loss in alkaline solutions. The damage within the

aggregate is observed to start at day 6 of exposure, and by day 8 a significant portion of the aggregate is observed to disintegrate.

Figure 4.6 shows a set of petrographic images for a mortar sample cast with aggregate F3. The 14-day expansion of aggregate F3 was 0.266%, around 2 times the 14-day expansion of aggregate F4. Thus AMBT results indicated a higher reactivity of aggregate F3 than aggregate F4. However, aggregate/paste debonding is not visible until day 10. After debonding, extensive microcracking occurs throughout the observed region, as marked by arrows in Figure 4.6e and Figure 4.6f. The age at which debonding and microcracking occurred in aggregate F3 is later than that of aggregate F4, which does not coincide with the relative reactivity of these two aggregates indicated by AMBT results. The discrepancy here reveals that the petrography tools could be used to verify the ASR products, but may not have enough accuracy in terms of discerning the relative reactivity of aggregates.

Figure 4.7 shows a set of petrographic images for a mortar sample cast with aggregate F6. The 14-day expansion of aggregate F3 was 0.099%, less than the expansion of previous three aggregates. Microcracks are visible in the microstructure only from day 14 as seen in Figure 4.7f. In contrast to other aggregates, debonding is not observed in any of the images.

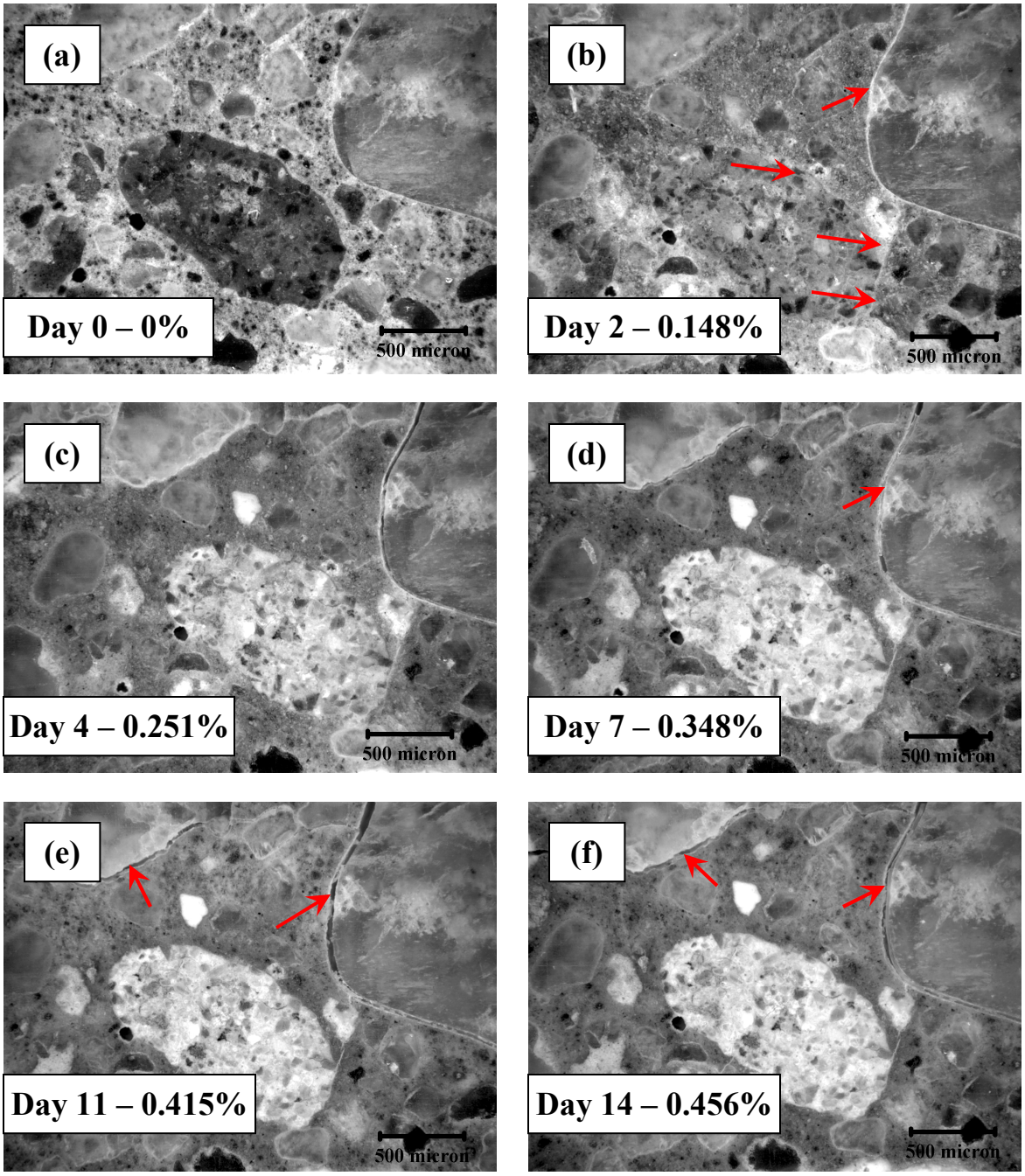

Figure 4.4 A set of petrographic images of samples cast with aggregate F1.

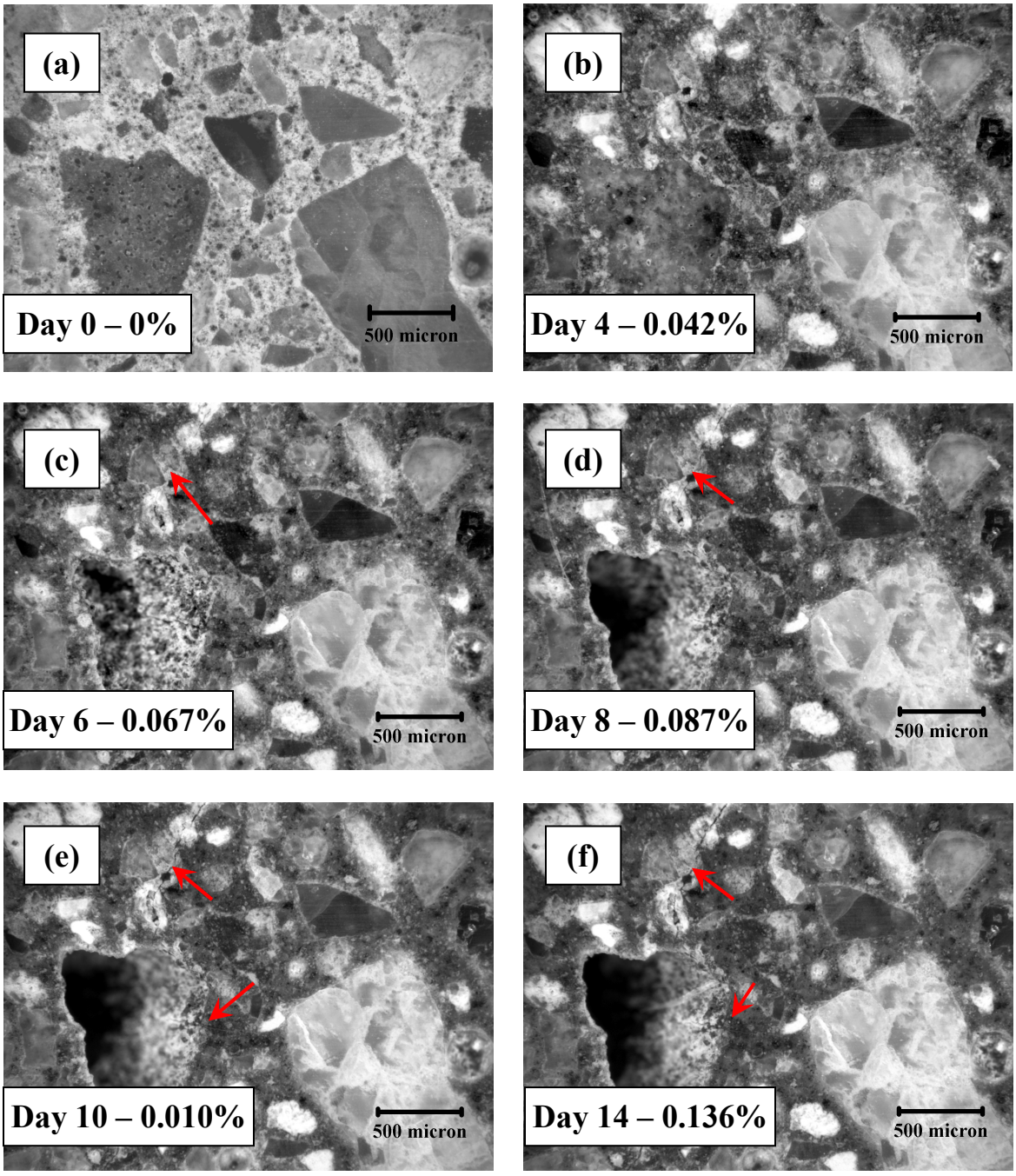

Figure 4.5 A set of petrographic images of samples cast with aggregate F4.

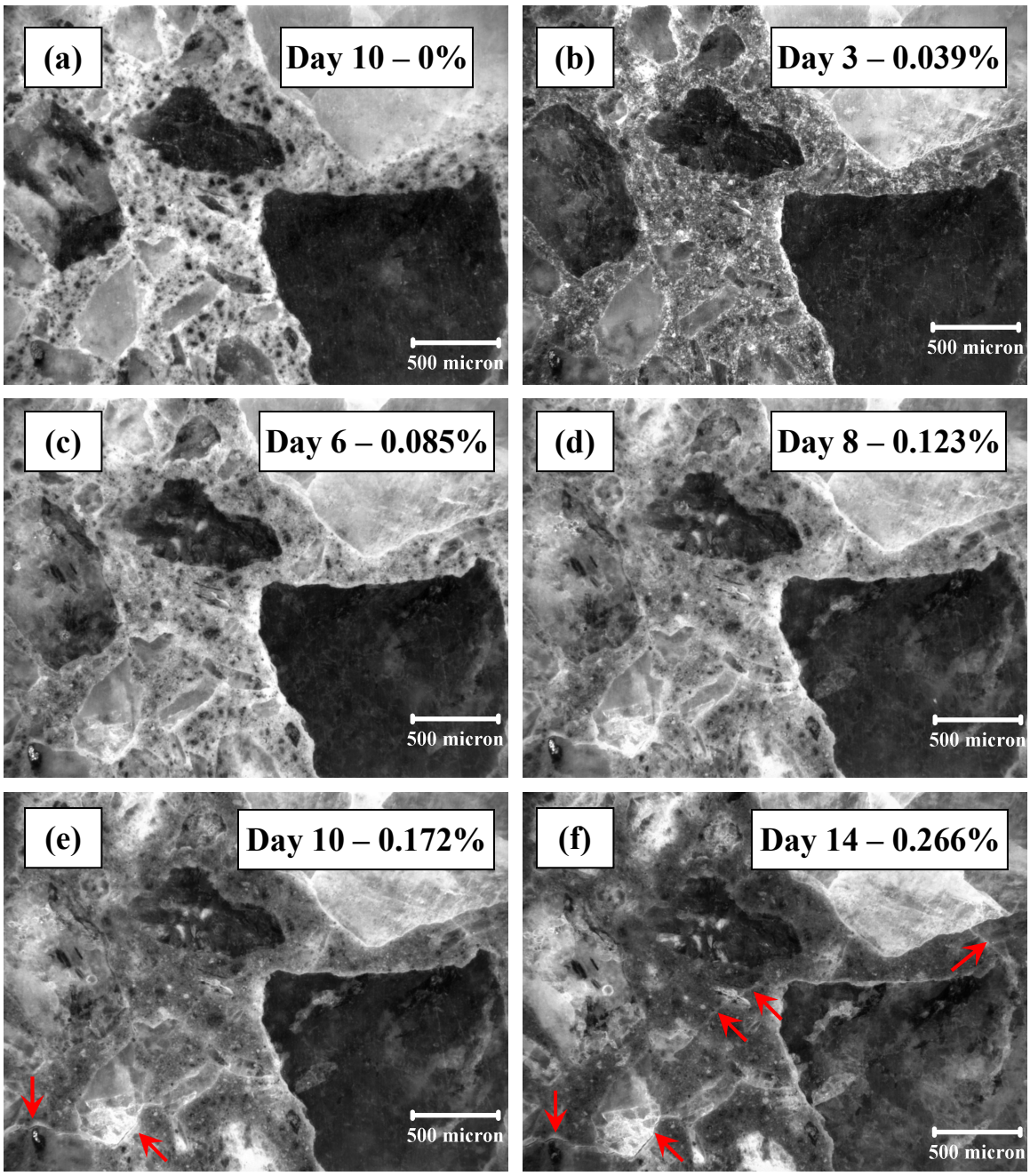

Figure 4.6 A set of petrographic images of samples cast with aggregate F3.

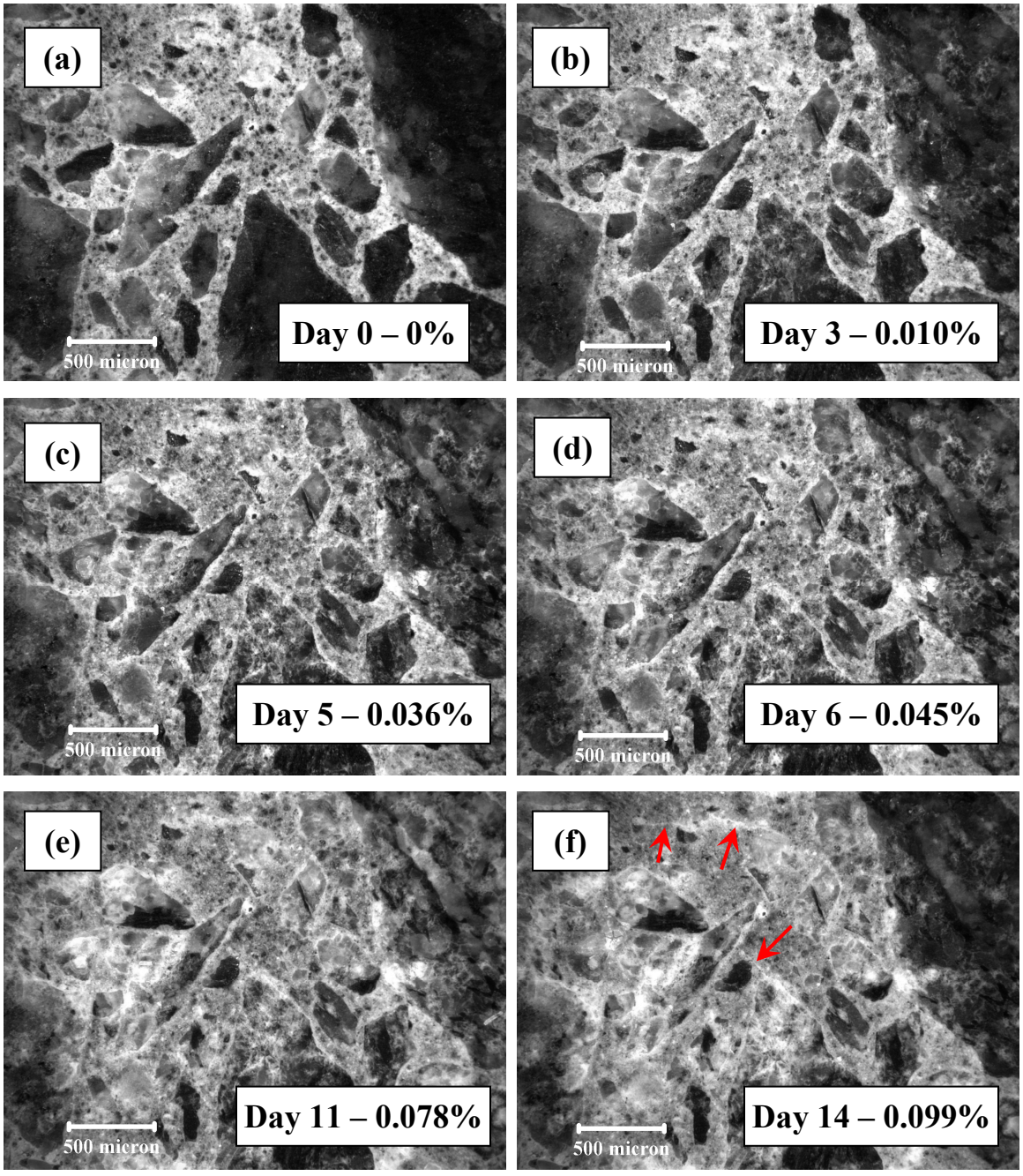

Figure 4.7 A set of petrographic images of samples cast with aggregate F6.

CHAPTER 5

LINNEAR MEASUREMENTS

In this chapter, two conventional linear measurements - Young's modulus and ultrasonic pulse velocity - are made on mortar samples as they experience progressive ASR damage during AMBT. The main purpose of these linear measurements is to examine the response of linear parameters to the ASR damage development in mortar samples. The comparison with the response of nonlinear parameters defined in nonlinear acoustic/ultrasonic techniques is presented in Chapter 8.

5.1 Measurements of Young's Modulus

The elastic moduli of mortars were calculated based on the stress-strain measurements made during compression tests performed over the 14-day accelerated exposure period. Compression tests were conducted on mortars prepared with four aggregates F1, F4, F6 and F7. The water-to-cement ratio was 0.5 and the aggregate-to-cement ratio was 2.25. For each aggregate, a ~90mm long specimen was cut from one mortar bar when the specimens were taken from the water after the 24-hour curing period. The stress-strain behavior of the specimens under compressive loading was recorded using a 100-kN universal testing machine and an extensometer (with a 0.004 strain accuracy) affixed on the specimen's surface. The specimens were loaded up to 40% of the initial (24-hr.) compressive strength, which was measured after the curing in water. Five measurements were made for each specimen at each age to minimize the variability

in the tests, and the average of the calculated modulus at each age was used. A picture of the testing apparatus is shown in Figure 5.1.

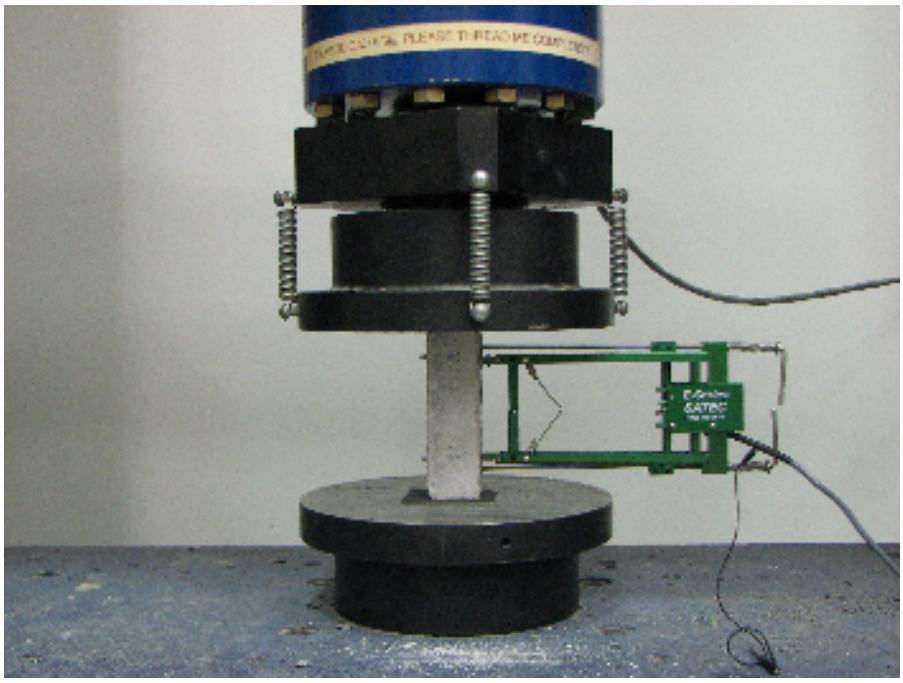

Figure 5.1 A picture for the compression tests of mortar samples.

The variation of elastic modulus of mortar samples with respect to the exposure time for these four aggregates is shown in Figure 5.2. The standard deviations for each of the modulus measurements are generally very small. It is seen in Figure 5.2 that the modulus of mortars containing aggregates F1 and F7 is substantially different from those of aggregate F4 and F6 even before the exposure to aggressive solution (day 0). This variation at day 0 could be attributed to the differences in the aggregates themselves (e.g., elastic modulus) and their bond with the surrounding paste, which can be influenced by factors such as the aggregate surface texture, angularity, and maximum size as shown in Figure 5.3.

In general, the measured modulus of elasticity decreases with exposure time for the potentially reactive aggregates, and increases (presumably due to continued cement hydration) for the innocuous aggregate F7. The modulus of the highly reactive aggregate F1 is seen to decrease most rapidly during the first 4 days when compared to that of the other aggregates. It is consistent with the previous AMBT expansion test shown in Figure 3.8 where the expansion of aggregate F1 has a fast growth rate during the first 4 days. The rapid drop of modulus of aggregate F1 at the beginning can be explained by the petrographic images in Chapter 4, where cracks were found for aggregate F1 very early (2-4 days). Previous research has indicated that the elastic modulus of cement-based materials is a property affected by defects, such as ASR-induced microcracking and debonding [92, 93]. However, the variations in elastic modulus between the moderately reactive aggregate F4 and marginally reactive aggregate F6 are indistinguishable from each other in the data in Figure 5.2. Overall, although such tests might provide an indication of the influence of the ASR damage on the mechanical response in the cases of highly reactive or innocuous aggregates, these results suggest that mechanical measurements of elastic modulus are not suitable as a practical method for distinguishing among aggregates of moderate to marginal reactivity.

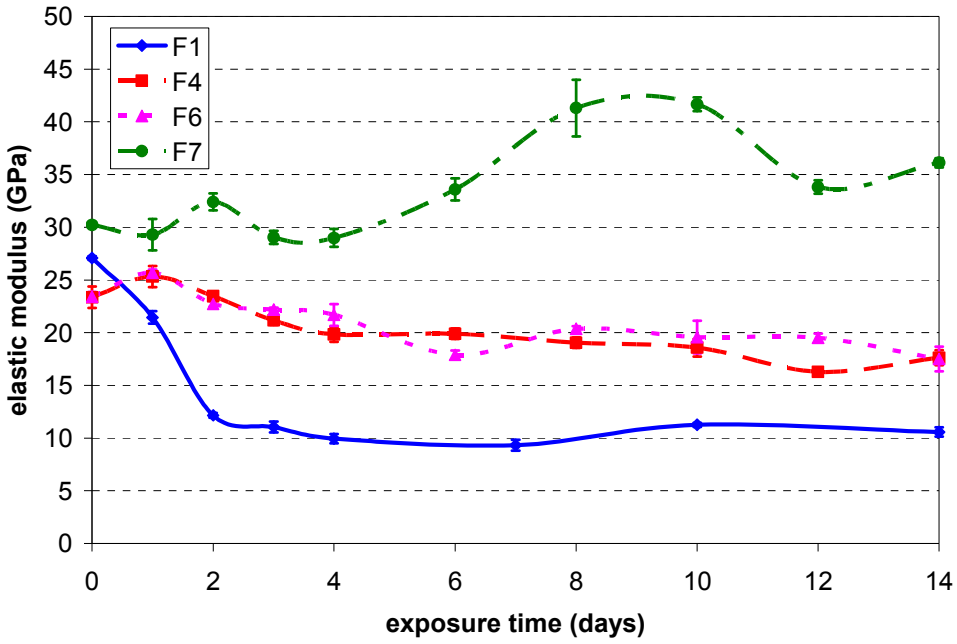

Figure 5.2 Variation of elastic modulus with respect to exposure time for four aggregates, where the aggregate reactivity – based upon 14-day expansion - varied F1>F4>F6>F7.

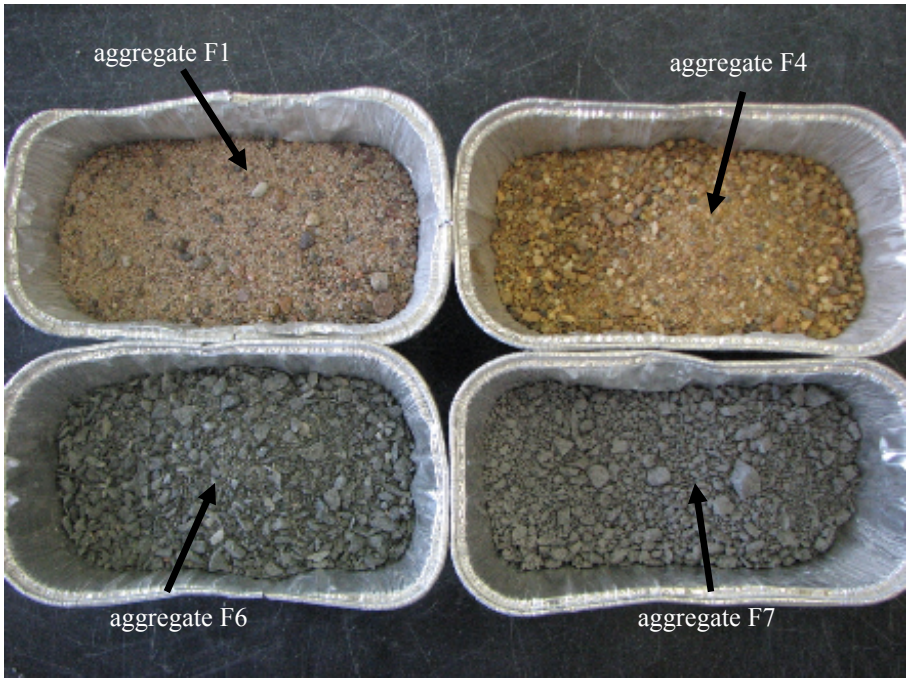

Figure 5.3 A photograph showing the difference in aggregate angularity and size for the four aggregates tested.

5.2 Measurements of Pulse Velocity

Ultrasonic pulse velocity was also measured when a pulse signal was transmitted across a cut mortar cube. The 25.4 cubic mm. mortar cubes were cut from the original mortar bars and were immersed into the NaOH solution together with samples for other linear and nonlinear measurements to induce the ASR damage. In the pulse velocity measurements, a pair of ~12.5mm (radius) ultrasonic transducers was affixed to the top and bottom surfaces of samples with a support fixture to excite and receive the pulse signal, respectively (Figure 5.4). The surfaces were appropriately ground and some coupling grease was also applied on the surfaces to provide a better contact with transducers. The incident pulse signal and received signal were both transmitted to an electronic oscilloscope. The propagation time of the signal through samples was calculated based on the time delay between incident and received signals.

Figure 5.4 Experimental set-up for the measurements of pulse velocity.

The variation of measured pulse velocities with respect to exposure time is shown in Figure 5.5. It is seen that the initial values of pulse velocities (prior to the exposure of samples to the strong alkaline solution) are different from each other, which is expected as in the case of Young's modulus since the pulse velocity is determined by elastic properties of materials given the identical geometrical conditions of samples. The pulse velocity of aggregate F1 has a substantial drop during the first 4 days, which also occurs in the measurements of Young's modulus of aggregate F1. The pulse velocity of aggregate F7 keeps a distinguishable distance from the pulse velocity of other three aggregates, which is also similar to the plot of Young's modulus. The pulse velocities of aggregate F4 and aggregate F6 are not differentiated from each other until day 8. Overall, the variations of measured pulse velocities shown in Figure 5.5 have a strong similarity to the variations of measured Young's modulus shown in Figure 5.2. It indicates that the pulse velocity method, originating from the principle of linear acoustics, is also not appropriate to serve as a rapid and reliable technique for the screening of moderately reactive aggregates and marginally reactive aggregates in terms of their alkali-reactivity.

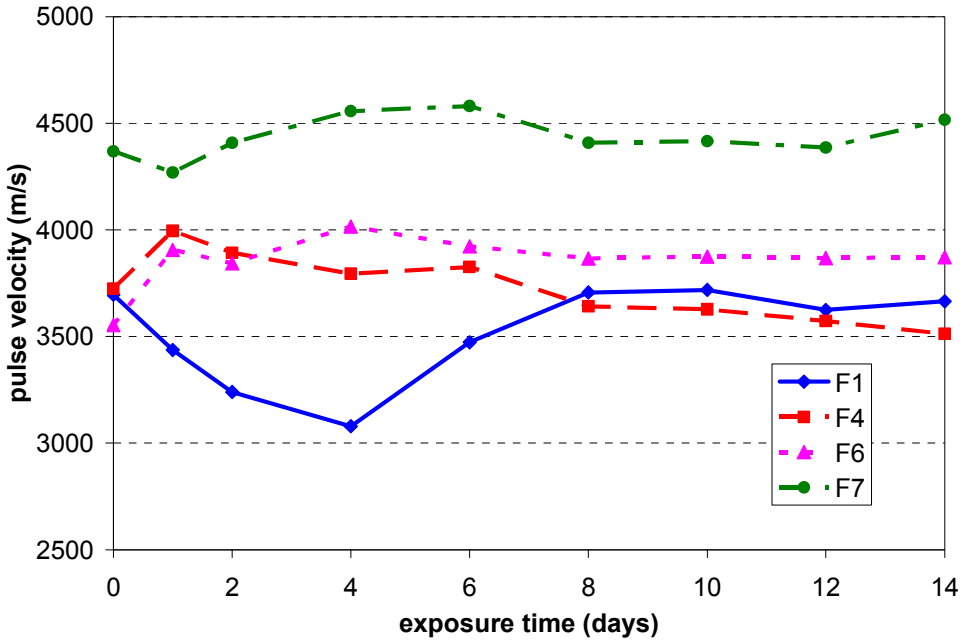

Figure 5.5 Variation of pulse velocity with respect to exposure time for four aggregates, where the aggregate reactivity – based upon 14-day expansion - varied F1>F4>F6>F7.

CHAPTER 6

NONLINEAR ACOUSTIC THEORY

6.1 Material Nonlinearity

The classical wave propagation theory assumes linear material media, which follow Hooke's law, i.e., the linear stress-strain relationship. The most characteristic example is that two waves can be simply superposed without disturbing each other. Another example is that the resonance vibration modes of samples made of a linear material are constants determined only by the material properties, geometry of samples and boundary conditions of the motion.

In reality, however, materials are usually not perfectly linear even without damages. Linear elasticity considers the elastic energy as a function of strain up to the second order, omitting the higher orders which actually cause the so-called atomic nonlinearity [79] in metals and crystals. Practically, the atomic nonlinearity is too small to measure so that the material is reasonably deemed as the linear medium in the intact condition. When the material undergoes microstructural damage such as imperfections (inclusions) and defects (cracks), the nonlinear signature in the material constitutive relation significantly increases. The interaction between separate waves makes the linear superposition not valid under the circumstance that the material nonlinearity manifests the constitutive relation of propagation media. In the following theoretical derivations for the different nonlinear wave propagation phenomena, different material nonlinearities are

thus considered in the constitutive relation. In addition, only the one-dimensional case is adopted in the derivations for the mathematical simplicity.

6.2 Nonlinear Wave Modulation Theory

In this section, a theoretical study is conducted for the nonlinear wave modulation effect of two propagating longitudinal waves. The general governing equation for 1-D longitudinal waves is expressed as

$$\rho \frac{\partial^2 u}{\partial t^2} = \frac{\partial \sigma}{\partial x} \tag{6.1}$$

where u is the particle displacement, σ is the corresponding stress, ρ is the mass density, t is time, and x is Cartesian coordinate.

With the classical atomic nonlinearity, the stress is expressed in terms of displacement as

$$\sigma = E_0 \left[1 + \beta \frac{\partial u}{\partial x} + \delta \left(\frac{\partial u}{\partial x} \right)^2 + \cdots \right] \frac{\partial u}{\partial x} \tag{6.2}$$

where E_0 is linear Young's modulus, β and δ are cubic and the quartic material nonlinearity coefficients, respectively. In this section, only the cubic nonlinearity β is considered in the derivation. Eq. (6.2) is thus simplified as

$$\sigma = E_0 \left(1 + \beta \frac{\partial u}{\partial x} \right) \frac{\partial u}{\partial x} \tag{6.3}$$

Substituting Eq. (6.3) into (6.1), a governing equation for the propagation of 1-D longitudinal waves in nonlinear media is derived as

$$\frac{\partial^2 u}{\partial t^2} = c_L{}^2 \frac{\partial^2 u}{\partial x^2} \left(1 + \beta \frac{\partial u}{\partial x} \right) \tag{6.4}$$

where $c_L = \sqrt{E_0 / \rho}$ is the phase velocity of longitudinal waves.

A perturbation analysis is carried out to get an approximate solution of Eq. (6.4). If the nonlinearity parameter β is zero, then Eq. (6.4) is downgraded to the linear case and a time-harmonic solution is easily obtained as

$$u^{(0)} = A\sin\left(k_L x - \omega t\right) \tag{6.5}$$

where A represents the amplitude, k_L is the wave number and ω is the angular frequency. We then can assume the solution of nonlinear equation (6.4) as

$$u = u^{(0)} + u^{(1)} \tag{6.6}$$

where $u^{(1)}$ is the first correction term and satisfies $\left|u^{(1)}\right| << \left|u^{(0)}\right|$.

A solution including the second harmonic is assumed for the first correction term as

$$u^{(1)} = B(x) + C(x)\sin 2\left(k_L x - \omega t\right) + D(x)\cos 2\left(k_L x - \omega t\right) \tag{6.7}$$

where $B(x) = B_0 x$, $C(x) = C_0 x$ and $D(x) = D_0 x$

Substituting (6.6) into (6.4), we have

$$\frac{\partial^2 u^{(0)}}{\partial t^2} + \frac{\partial^2 u^{(1)}}{\partial t^2} = {c_L}^2\left(\frac{\partial^2 u^{(0)}}{\partial x^2} + \frac{\partial^2 u^{(1)}}{\partial x^2}\right) + {c_L}^2\beta\frac{\partial}{\partial x}\left[\left(\frac{\partial u^{(0)}}{\partial x}\right)^2 + 2\left(\frac{\partial u^{(0)}}{\partial x}\right)\left(\frac{\partial u^{(1)}}{\partial x}\right) + \left(\frac{\partial u^{(1)}}{\partial x}\right)^2\right] \tag{6.7}$$

Since $\left|\frac{\partial u^{(1)}}{\partial x}\right| << \left|\frac{\partial u^{(0)}}{\partial x}\right|$, Eq. (6.7) can be approximated as

$$\frac{\partial^2 u^{(0)}}{\partial t^2} + \frac{\partial^2 u^{(1)}}{\partial t^2} = {c_L}^2\left(\frac{\partial^2 u^{(0)}}{\partial x^2} + \frac{\partial^2 u^{(1)}}{\partial x^2}\right) + {c_L}^2\beta\frac{\partial}{\partial x}\left[\left(\frac{\partial u^{(0)}}{\partial x}\right)^2\right] \tag{6.8}$$

Linear solution $u^{(0)}$ satisfies $\frac{\partial^2 u^{(0)}}{\partial t^2} = {c_L}^2\frac{\partial^2 u^{(0)}}{\partial x^2}$, and thus the following equation regarding the correction term is obtained

$$\frac{\partial^2 u^{(1)}}{\partial t^2} = {c_L}^2 \frac{\partial^2 u^{(1)}}{\partial x^2} + {c_L}^2 \beta \frac{\partial}{\partial x}\left[\left(\frac{\partial u^{(0)}}{\partial x}\right)^2\right] \tag{6.9}$$

Substituting Eqs. (6.5) and (6.7) into (6.9) and equaling the coefficients of both sides, the following expressions are obtained

$$B_0 = -\frac{1}{8}\beta {k_L}^2 A^2,\ C_0 = 0,\ D_0 = \frac{1}{8}\beta {k_L}^2 A^2 \tag{6.10}$$

Eq. (6.6) is further elaborated as

$$u = -\frac{1}{8}\beta {k_L}^2 A^2 x + A\sin(k_L - \omega t) + \frac{1}{8}\beta {k_L}^2 A^2 x \cos 2(k_L - \omega t) \tag{6.11}$$

It is seen that a second harmonic of incident signal would be generated if the incident signal goes through a nonlinear medium described by Eq. (6.3). The amplitude of second harmonic component A_2 is proportional to the square of amplitude of incident signal A and the cubic nonlinearity parameter β as below

$$A_2 = \frac{\beta {k_L}^2 x A^2}{8} \tag{6.12}$$

In the nonlinear wave modulation theory, two wave sources having different amplitudes and different frequencies interact with each other through the propagation in the nonlinear media. The second harmonic can be considered as the modulation effect of two identical waves having the same amplitude A and frequency f. The modulated interaction of two identical waves results in a new signal component (second harmonic) having a frequency located at the summation of two incident signal frequencies ($2f=f+f$). The amplitude of new signal component is proportional to multiplication of amplitudes of two incident signals ($A_2 \propto \beta \cdot A \cdot A$). In analogy, the nonlinear modulation of the two waves having different frequencies produces frequency components occurring at the location $f_1 \pm f_2$, which are called "sidebands" in the frequency domain. The amplitude of

sidebands is expected to be proportional to the amplitudes of both incident waves as well as the cubic nonlinearity parameter

$$U_3 \propto \beta U_1 U_2 \tag{6.13}$$

where U_3 is amplitude of sidebands, U_1 and U_2 are amplitudes of high frequency and low frequency waves, respectively.

A schematic diagram of sidebands due to the nonlinear wave modulation effect is shown in Figure 6.1. The frequencies of two incident signals are 5 and 40 kHz, respectively. The sidebands occur at the locations of 35 and 45 kHz.

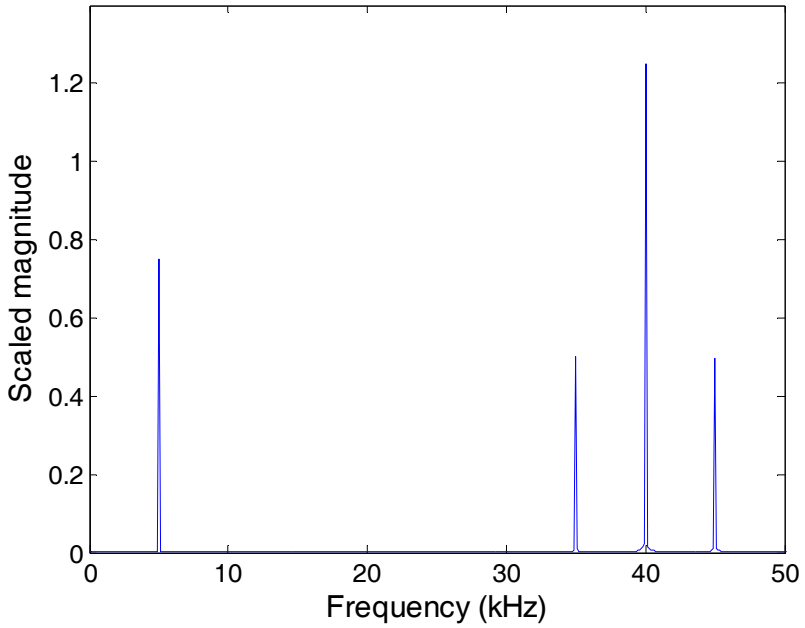

Figure 6.1 A schematic diagram of sidebands due to the wave modulation effect.

6.3 Nonlinear Impact Resonance Theory

In this section, a theoretical study is conducted for the nonlinear resonance theory of transverse vibrations of cantilever beams subjected to an impulse force. The geometric

and material parameters used in the theoretical derivation are pre-defined as: beam length L, cross-section area S, width of cross-section b, thickness of cross-section h, density of material ρ, Young's modulus E_0. The bending vibration of the beam is driven by an impulse impact force applied on the middle spot of the beam.

As stated in the nonlinear wave modulation theory, the traditional material nonlinearity is described by the classical atomic anharmonic constants. Recent studies [84, 85] show that the hysteresis effect is also very important for the nonlinear acoustics, particularly for the phenomenon of nonlinear resonance shift. A constitutive relation considering both the classical anharmonicity and the new hysteresis effect is thus assumed in this section

$$\sigma = E_0\left[1 + \beta\varepsilon + \delta\varepsilon^2 + \alpha(\Delta\varepsilon + \varepsilon \cdot \mathrm{sgn}(\dot{\varepsilon}))\right]\varepsilon \tag{6.14}$$

where ε is the strain, $\Delta\varepsilon$ is the strain amplitude, $\dot{\varepsilon}$ is the strain rate, α is the strength of hysteresis, and *sgn* is the sign function. In the derivation below, nonlinear parameters α, β are δ are assumed to be uniform throughout the volume of specimen and independent of the geometric location.

Defining y as the distance of an element area dS in the cross section to the neutral axis, the bending moment M of cross-section S is calculated below according to the classical beam bending theory

$$M = -\int_S \sigma_x y dA = -E_0 \int_S [1 + \beta\varepsilon + \delta\varepsilon^2 + \alpha(\Delta\varepsilon + \varepsilon \cdot \mathrm{sgn}(\dot{\varepsilon}))]\varepsilon \cdot y dS \tag{6.15}$$

With the assumption of small transverse deformation $u(x)$, the strain ε of the element area dS is expressed by

$$\varepsilon = -\frac{\partial^2 u}{\partial x^2} y \tag{6.16}$$

Substituting Eq. (6.16) into Eq. (6.15), we have

$$\begin{aligned} M &= E_0 b \int_{-h/2}^{h/2} \left[u'' y^2 - \beta (u'')^2 y^3 + \delta (u'')^3 y^4 + \alpha \cdot \Delta u'' \cdot u'' \cdot |y| \cdot y^2 - \alpha (u'')^2 y^3 \cdot \mathrm{sgn}(\dot{\varepsilon}) \right] dy \\ &= E_0 b \left[\frac{1}{12} h^3 u'' + \frac{1}{80} \delta h^5 (u'')^3 + \frac{1}{32} \alpha h^4 \cdot \Delta u'' \cdot u'' + \frac{1}{32} \alpha h^4 (u'')^2 \right] \\ &= E_0 I \left[u'' + \frac{3}{20} \delta h^2 (u'')^3 + \frac{3}{8} \alpha h \left(\Delta u'' \cdot u'' + (u'')^2 \right) \right] \end{aligned} \tag{6.17}$$

where $I = \frac{1}{12} bh^3$ is the moment of inertia and $\Delta u''$ represents the amplitude of second derivative of vertical displacement.

The equilibrium equation of flexural vibrations for a beam subjected to an impact force at the middle point is given as

$$\frac{\partial^2 M}{\partial x^2} + \frac{1}{\tau_0} \frac{\partial u}{\partial t} + \rho A \frac{\partial^2 u}{\partial t^2} = F(t) \delta (x - \frac{L}{2}) \tag{6.18}$$

in which τ_0 is the damping coefficient and $F(t)$ is force per unit length. Substituting Eq. (6.17) into Eq. (6.18) we have the equilibrium equation in terms of displacement

$$\begin{aligned} & E_0 I \left(1 + \frac{3}{8} \alpha h \cdot \Delta u'' \right) \frac{\partial^4 u}{\partial x^4} + \frac{9}{20} \delta h^2 E_0 I \left[2 \frac{\partial^2 u}{\partial x^2} \cdot \left(\frac{\partial^3 u}{\partial x^3} \right)^2 + \left(\frac{\partial^2 u}{\partial x^2} \right)^2 \cdot \frac{\partial^4 u}{\partial x^4} \right] \\ & + \frac{3}{4} \alpha h E_0 I \left[\left(\frac{\partial^3 u}{\partial x^3} \right)^2 + \frac{\partial^2 u}{\partial x^2} \cdot \frac{\partial^4 u}{\partial x^4} \right] + \frac{1}{\tau_0} \frac{\partial u}{\partial t} + \rho A \frac{\partial^2 u}{\partial t^2} = F(t) \delta (x - \frac{L}{2}) \end{aligned} \tag{6.19}$$

The excitation of vibrations studied here is an impulse signal which has a broad band covering multiple resonant modes of the object bar in the spectrum. For the simplicity of calculations, only the fundamental resonance mode is considered in the derived solution and the external excitation in Eq. (6.18) can thus be assumed as a harmonic signal having an angular frequency at the fundamental resonance mode ω

$$F(t) = F \cos(wt) \tag{6.20}$$

The free-clamp boundary conditions for the cantilever beam in the coordinate system can be expressed as

$$u\big|_{x=0} = 0 \quad \frac{\partial u}{\partial x}\big|_{x=0} = 0 \quad \frac{\partial^2 u}{\partial x^2}\big|_{x=L} = 0 \quad \frac{\partial^3 u}{\partial x^3}\big|_{x=L} = 0 \tag{6.21}$$

To satisfy the above boundary conditions, an approximate displacement field separating the spatial function and temporal function is assumed as

$$u(x,t) = \Psi(x)\eta(t) \text{ where } \Psi(x) = U(6L^2x^2 - 4Lx^3 + x^4) \text{ and } \eta(t) = \cos(\omega t + \phi) \tag{6.22}$$

Since Eq. (6.22) is not the rigorous solution, there is a residual value when it is substituted into Eq. (6.19). Defining the residual value as $R(x, t)$, then the following equation is obtained based on the Ritz method

$$\int_0^L R(x,t)\Psi(x) = 0 \tag{6.23}$$

Substituting Eq. (6.22) into Eq. (6.19), the residual value is calculated

$$\begin{aligned} R(x,t) &= 24E_0I(1+4.5\alpha hL^2U)U\cos(\omega t+\phi) + 7776E_0I\delta h^2(x-L)^4U^3\cos^3(\omega t+\phi) \\ &+ 648E_0I\alpha h(x-L)^2U^2\cos^2(\omega t+\phi) - \frac{\omega}{\tau_0}(6L^2x^2 - 4Lx^3 + x^4)U\sin(\omega t+\phi) \\ &- \rho A\omega^2(6L^2x^2 - 4Lx^3 + x^4)U\cos(\omega t+\phi) - F\cos(\omega t)\delta(x-\frac{L}{2}) \end{aligned} \tag{6.24}$$

Substituting Eqs. (6.22) and (6.24) into (6.23), the following equation regarding the amplitude U is obtained

$$\begin{aligned} &28.8E_0I(1+4.5\alpha hL^2U)L^5U\cos(\omega t+\phi) + 342.1E_0I\delta h^2L^9U^3\cos^3(\omega t+\phi) \\ &+ 92.7E_0I\alpha hL^7U^2\cos^2(\omega t+\phi) - 2.3\frac{\omega}{\tau_0}L^9U\sin(\omega t+\phi) \\ &- 2.3\rho A\omega^2UL^9\cos(\omega t+\phi) = 1.1FL^4\cos(\omega t) \end{aligned} \tag{6.25}$$

To split Eq. (6.25) and equate the coefficients of harmonic terms about frequency ω, a couple of equations in terms of the amplitude U and the phase ϕ can be obtained as below

$$[28.8E_0I(1+4.5\alpha hL^2U)LU+128.3E_0I\delta h^2L^5U^3-2.3\rho A\omega^2L^5U]\cos\phi-2.3\frac{\omega}{\tau_0}L^5U\sin\phi=1.1F$$

$$[28.8E_0I(1+4.5\alpha hL^2U)LU+128.3E_0I\delta h^2L^5U^3-2.3\rho A\omega^2L^5U]\sin\phi+2.3\frac{\omega}{\tau_0}L^5U\cos\phi=0 \tag{6.26}$$

Thus the amplitude U can be eventually solved as

$$U=\frac{\widetilde{F}}{\sqrt{\left(1+\lambda_1U+\lambda_2U^2-\left(\frac{\omega}{\omega_0}\right)^2\right)^2+\left(\frac{\omega}{\rho A\tau_0\omega_0^2}\right)^2}} \tag{6.27}$$

where $\widetilde{F}=\frac{0.038F}{E_0IL}$, $\lambda_1=4.5\alpha hL^2$, $\lambda_2=4.5\delta h^2L^4$, and $\omega_0=\frac{1}{\sqrt{0.08}}\sqrt{\frac{E_0I}{\rho AL^4}}=3.54\sqrt{\frac{E_0I}{\rho AL^4}}$ which is the linear bending mode corresponding to the defined displacement field of Eq. (6.22).

Defining normalized frequency $\Omega=\omega/\omega_0$ and quality factor $Q=\rho A\tau_0\omega$, Eq. (6.27) can be further revised as

$$U=\frac{\widetilde{F}}{\sqrt{\left(1+\lambda_1U+\lambda_2U^2-\Omega^2\right)^2+\left(\frac{\Omega^2}{Q}\right)^2}} \tag{6.28}$$

The solution is consistent with what Van Den Abeele [86] and Guyer et al. [87] derived for the longitudinal resonance modes of one-dimensional bars.

In linear resonance case, nonlinear parameters λ_1 and λ_2 are equal to zero, and the expression of amplitude is simplified to

$$U = \frac{\widetilde{F}}{\sqrt{\left(1-\Omega^2\right)^2 + \left(\frac{\Omega^2}{Q}\right)^2}} \tag{6.29}$$

The maximum amplitude response occurs when the first derivative of amplitude to normalized frequency is equal to zero ($dU/d\Omega = 0$). The linear resonance frequency with consideration of the damping effect is thus calculated as

$$\omega_{lin} = \frac{\omega_0}{\sqrt{1+\frac{1}{Q^2}}} \tag{6.30}$$

When the nonlinear resonance is considered, the terms containing nonlinear parameters in the denominator of Eq. (6.28) are small compared to the unity and counted as constants. Then the nonlinear resonance frequency with consideration of the attenuation effect can be solved from Eq. (6.28) in a fashion similar to in the linear case

$$\omega = \frac{\omega_0}{\sqrt{1+\frac{1}{Q^2}}}\sqrt{1+\lambda_1 U+\lambda_2 U^2} \approx \omega_{lin}\left[1+0.5\left(\lambda_1 U+\lambda_2 U^2\right)\right] \tag{6.31}$$

Eq. (6.31) is easily converted to

$$\frac{\omega-\omega_{lin}}{\omega} \approx 0.5\left(\lambda_1 U+\lambda_2 U^2\right) \tag{6.32}$$

or in terms of ordinary frequency

$$\frac{f-f_{lin}}{f} \approx 0.5\left(\lambda_1 U+\lambda_2 U^2\right) \tag{6.33}$$

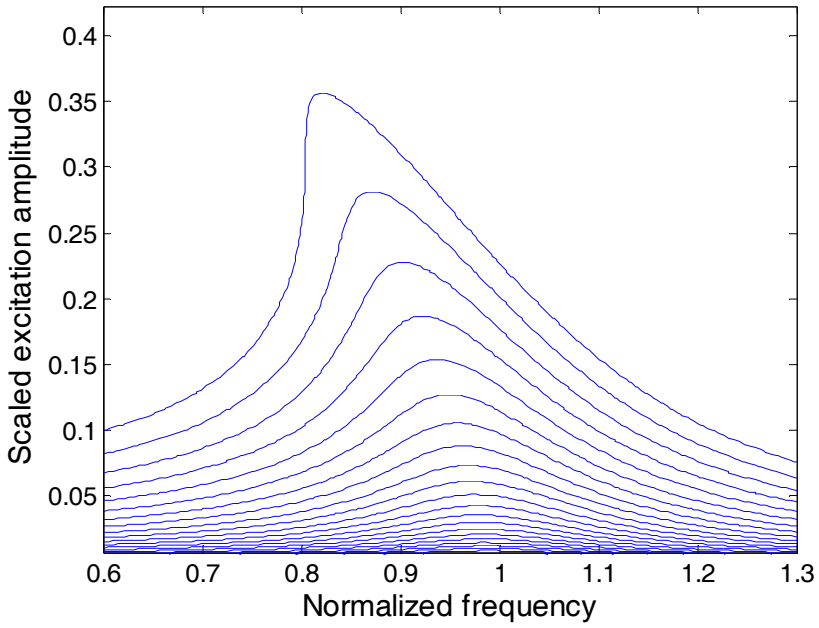

Figure 6.2 A schematic diagram of resonance frequency shift.

A simple numerical simulation is implemented first by utilizing the above nonlinear flexural vibration model to schematically demonstrate the shift of resonance frequency with the increased excitation (correspondingly increased resonance displacement). For cement-based materials studied in the work, nonlinear parameters λ_1 and λ_2 are negative due to the strain softening characteristics [87] and resonance frequencies have a downward shift from their linear values. In this preliminary numerical implementation, these nonlinear parameters and quality factor are assumed as $\lambda_1 = -0.5$, $\lambda_2 = -1$ and $Q = 5$. The vibration amplitude U is plotted in Figure 6.2 against the normalized frequency Ω with the increased scaled impact force $\widetilde{F}$. It is clearly shown that a shift of resonance frequency occurs when the impact is large enough to excite the nonlinear response of materials. The shift moves downward indicating that the nonlinear resonance frequency becomes smaller compared to the initial linear value. In addition, the

rate of resonance frequency shift becomes larger when the excitation increases to a certain range, which is explained as below by further analyzing Eq. (6.33).

When the materials suffer damage, the linear term related to hysteresis λ_1 in Eq. (6.33) is dominant for the shift of resonance frequency if the resonance amplitude U is under a relatively low level (much less than the unity). When the resonance amplitude grows to a large scale (about the order of the unity), the quadratic term related to λ_2 attributes the nonlinearity and has to been taken into consideration. The shift of resonance frequency will be off the linear trend with respect to the resonance amplitude. The effects of λ_1 and λ_2 on the shift of resonance frequency in different scales of resonance amplitude are shown in Figure 6.3.

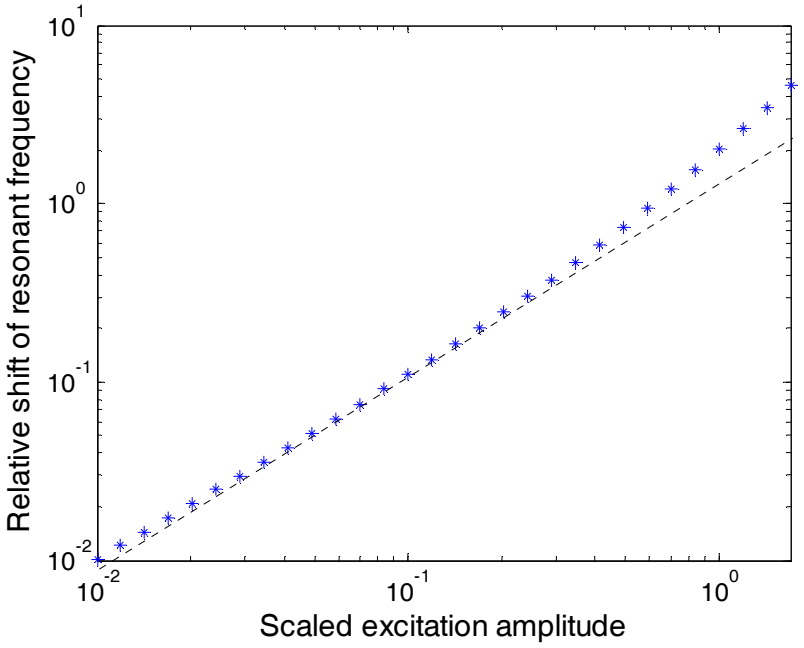

Figure 6.3 Relation between relative shift of resonance frequency and excitation amplitude.

CHAPTER 7

NONLINEAR WAVE MODULATION SPECTROSCOPY

7.1 Experimental Setup

In this chapter, the nonlinear wave modulation spectroscopy (NWMS) is presented for the ASR characterization [94]. The NWMS technique is an experimental application of nonlinear wave modulation theory presented in Chapter 6. The experimental setup is schematically shown in Figure 7.1, and a photograph of experimental instrumentation is shown in Figure 7.2.

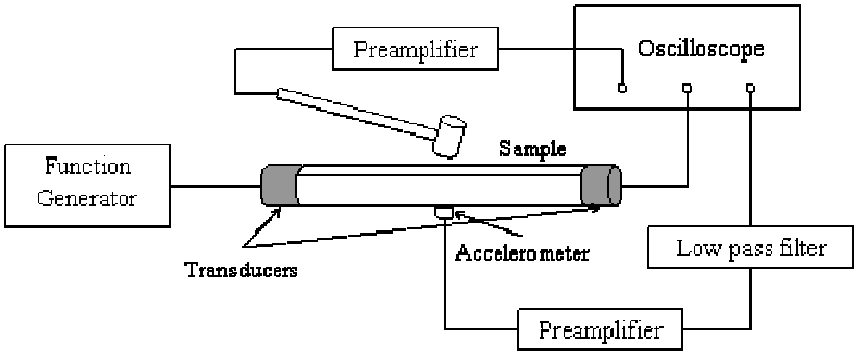

Figure 7.1 A schematic diagram of NWMS experimental setup.

As stated in Chapter 6, the nonlinear wave modulation theory considers the interaction effect of two different signals having different frequencies. A high frequency and a low frequency signal are thus needed for the NWMS technique. In the NWMS

experiments the probing high frequency signal was generated by a function generator (Wavetek 185) as a continuous sinusoidal wave with a frequency of 39 kHz. The selection of this 39 kHz is based on a compromise between reducing attenuation of cement-based materials and avoiding overlap with the low frequency signal. As stated earlier in Chapter 2, cement-based materials have a much stronger attenuation on the wave propagation than the metallic materials, which is increasingly severe at higher frequencies. Thus the selected signal has to be as low as possible ideally to get the best transmission. However, the low frequency signal considered in this study is an acoustic vibration which has a broadband spectrum up to 10 kHz. Therefore, the selected frequency of continuous wave has to be sufficient apart from the upper limit of the low frequency signal as well.

The high frequency wave traveled along the longitudinal direction of mortar bars, which was coupled with the narrowband piezoelectric transducer (Panametrics X1021 50 kHz) at both ends. The low frequency signal was produced by the resonance of specimens when it was impacted by an instrumented hammer (PCB 086C03). An accelerometer (PCB 309A) was affixed on the opposite surface of specimens to record the low frequency signal. Both the high frequency modulated signal from the output transducer and the low frequency impact signal from the accelerometer were transmitted to an oscilloscope (Tektronix TDS 5034) and were recorded.

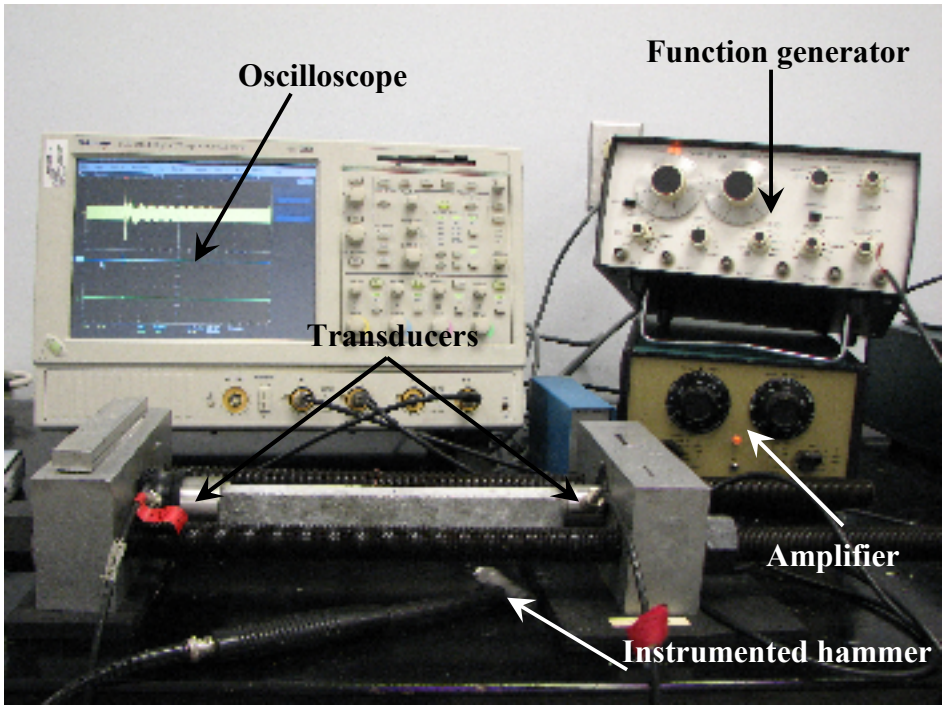

Figure 7.2 Photograph of NWMS experimental instrumentation.

7.2 Results and Discussion of Mortar Samples

7.2.1 Nonlinearity Parameter in NWMS Technique

In the NWMS tests for mortar samples, aggregates F1, F4 and F6 were used and three samples were cast for each aggregate. The sample preparation for the NWMS tests is the same as for the AMBT expansion measurements.

As described in the above, the signals from transducer and accelerometer were acquired by the oscilloscope in the time domain. To obtain a high frequency resolution, the duration of signals was set to 0.1s. A typical plot of the modulated probing wave and impact wave in the time domain is shown in Figure 7.3. The time-domain signals were

then rectangular windowed and transformed to the frequency domain with standard Fast Fourier Transform (FFT). The resulting signals are shown in Figure 7.4. It was seen in the frequency domain of modulated probing signal that the frequency of fundamental signal is at 39 kHz, and some sidebands were observed around this central frequency. Due to the high attenuation characteristic of cement-based materials, the peaks of these sidebands were not clearly distinguishable in the frequency domain as is commonly observed in the case of metals.

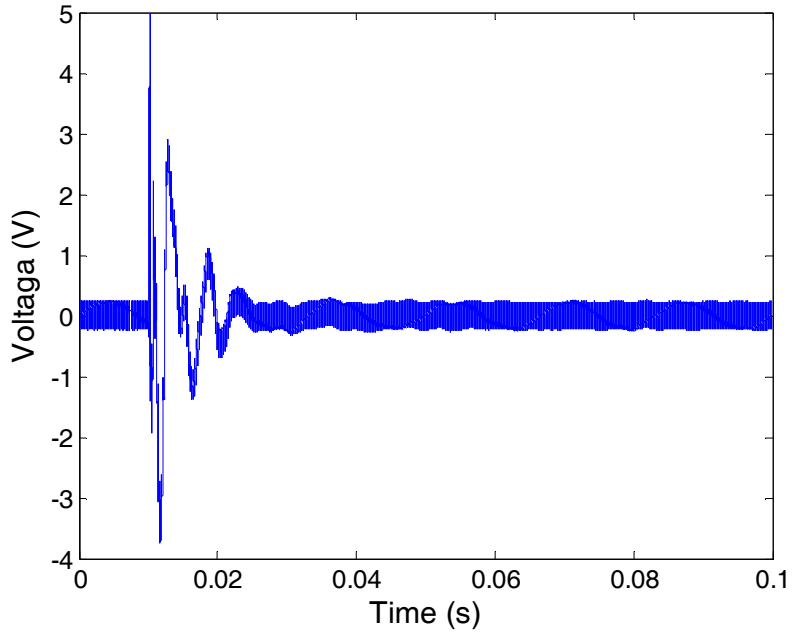

Figure 7.3(a) Modulated probing signal in the time domain.

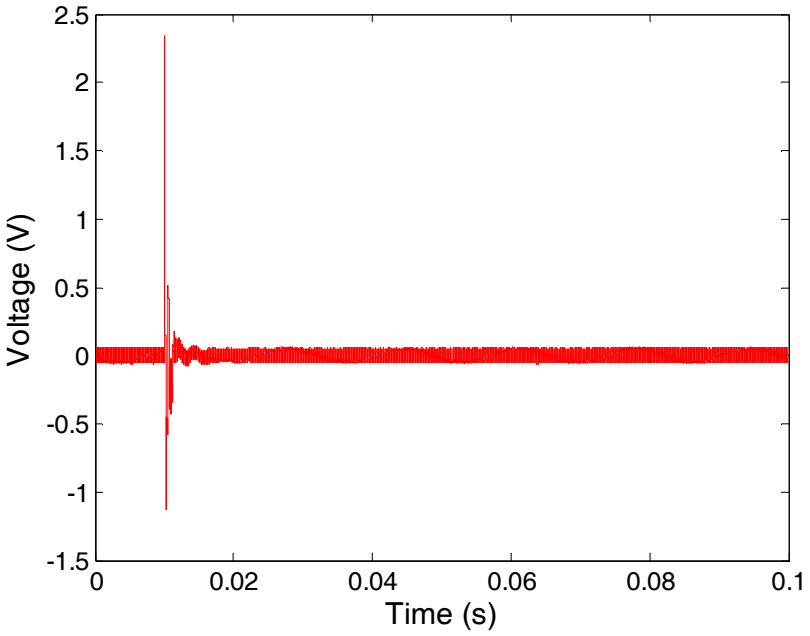

Figure 7.3(b) Impact signal in the time domain.

Therefore, the sideband amplitude could not simply be adopted here to derive the nonlinearity parameter β as in Eq. (6.13). An integration of magnitude of signal over a defined length in frequency domain, which was believed to cover the entire sideband domain, was performed. This integral was considered as a new variable "sideband energy" E_3 corresponding to U_3 in Eq. (6.13). The integration values corresponding to U_1 and U_2 were also carried out and termed "probing energy" E_1 and "impact energy" E_2. (Note that these "energies" are not true energies since they are integration of signal magnitude over frequency instead of integration of spectral power densities). Since E_1, E_2 and E_3 are proportional to U_1, U_2 and U_3, the relation among energies is derived based on Eq. (6.13)

$$E_3 \propto DE_1E_2 \tag{7.1}$$

where D is a defined nonlinearity parameter proportional to β.

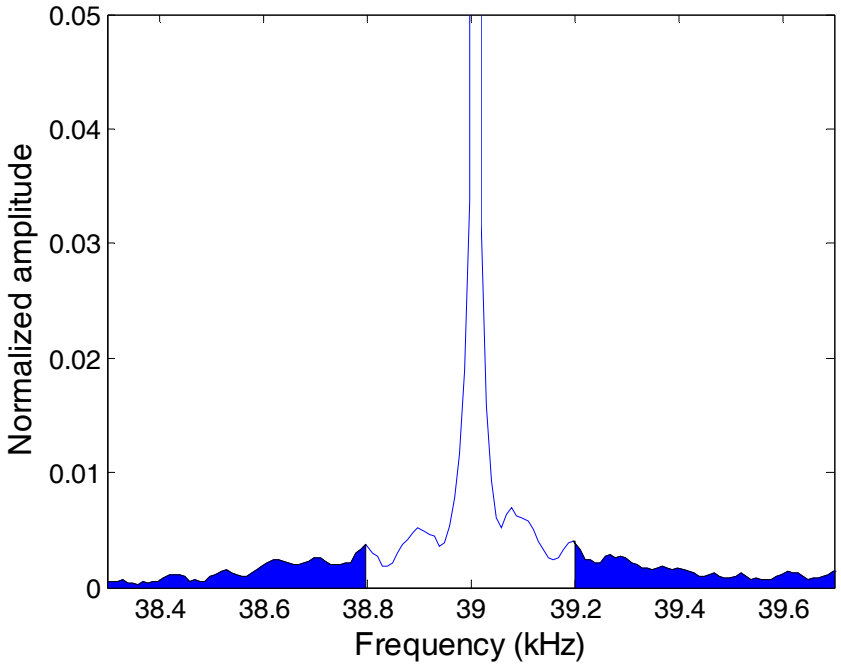

Figure 7.4(a) Modulated probing signal in the frequency domain.

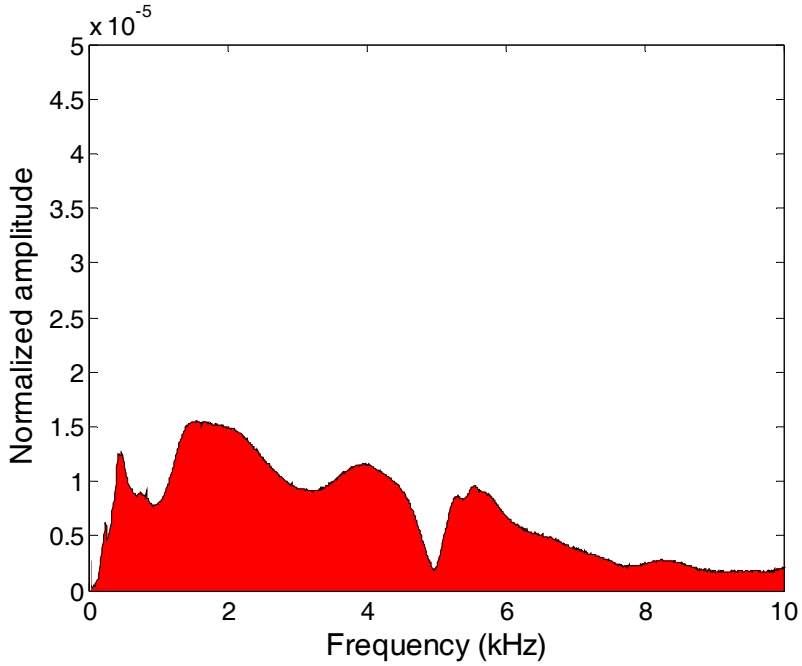

Figure 7.4 (b) Impact signal in the frequency domain.

It was found that when the probing wave was unchanged, the sideband energy had a linear relation with impact energy and the slope of this relationship can be considered proportional to the nonlinearity parameter D. The probing wave was generated by the function generator in the experiments, and it did not vary in ideal conditions. But since the impact of hammer may change the contact condition between the specimen and transducers and further affect the amplitude of probing wave, a normalization of magnitude of signal in frequency domain was conducted to ensure the invariability of the probing energy E_1. The integrated energies are shown as the shaded regions in Figure 7.4.

7.2.2 Linearity of Equipments

It is necessary to review the possible intrinsic nonlinearity of experimental equipments before the detailed study of ASR material nonlinearity in mortar samples. In addition, the leakage during the signal processing may also bring extra sidebands within the spectrum of interest, and it is important to determine the relative magnitude of sideband energy caused by signal processing. Thus, a generally-accepted linear material - polymethyl methacrylate (PMMA) - was used first for the NWMS test, and impacts of different magnitudes were applied on the PMMA bar in the test. The procedure introduced in Figure 7.3 and Figure 7.4 was used for the signal processing and calculation of sideband energy and impact energy of the PMMA bar. The spectrum of high frequency and the variation of sideband energy versus impact energy are shown in Figure 7.5. It can be observed that the sideband amplitudes in Figure 7.5a are negligible compared to the sidebands observed in Figure 7.4a (in the same scale). The sidebands in Figure 7.5a may be considered as the outcome of signal processing. But the corresponding sideband

energy for PMMA does not increase and has nearly a flat relationship with respect to increased impact energy as shown in Figure 7.5b. It will be shown later that the magnitude of sideband energy due to the signal processing is negligible compared to that of the sideband energy caused by true material nonlinearity such as ASR damage. Hence the sidebands due to signal processing would not affect the study of ASR damage in mortar samples.

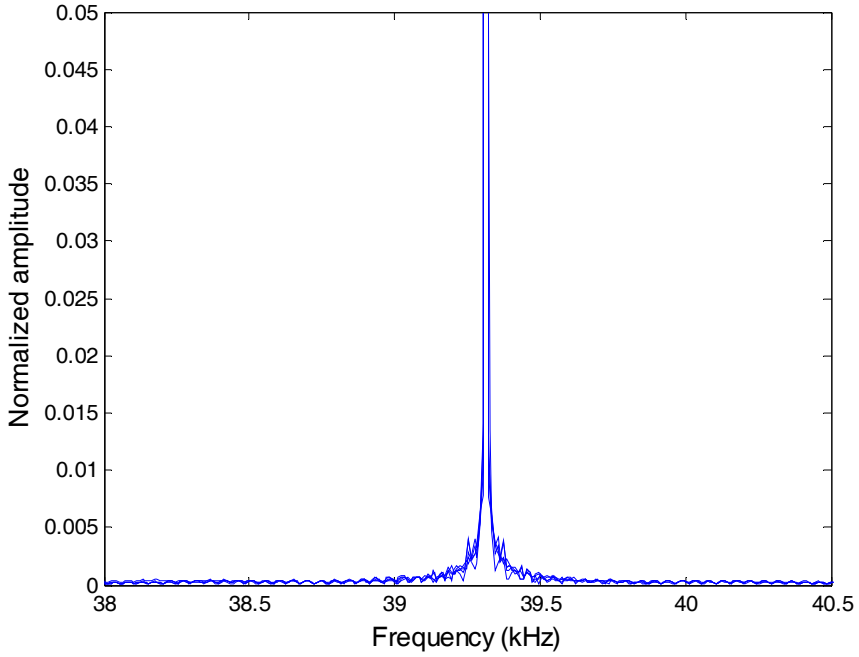

Figure 7.5(a) Spectra of modulated signal for PMMA bar.

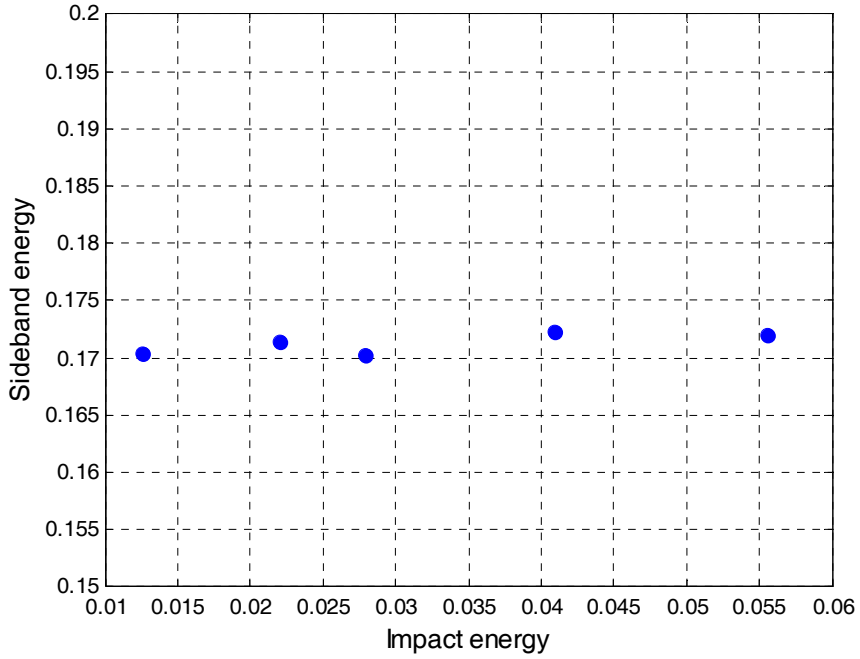

Figure 7.5(b) Flat relation between sideband energy and impact energy for PMMA bar.

The ASR damage in mortar samples were systematically studied using the developed NWMS method using the procedure given below. For each sample, a series of hammer impacts with different magnitudes were performed on the specimen on each day of exposure. The groups of impact and sideband energies were plotted, and the slope of their linear relationship was determined. An example of the energy relationship is plotted in Figure 7.6. This slope-of-energy in Figure 7.6 is the nonlinearity parameter *D* which was used in the NWMS measurement to represent the extent of ASR damage in mortar samples.

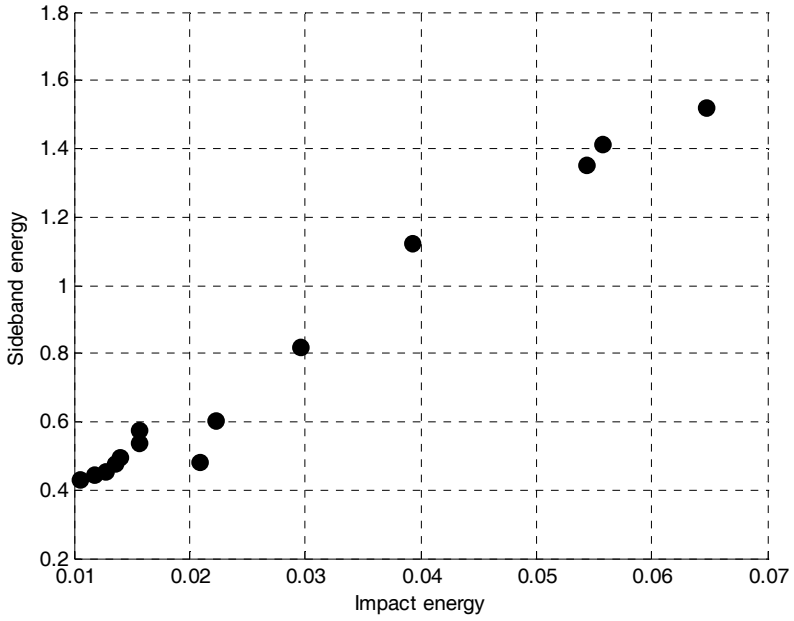

Figure 7.6 Linear relation between sideband energy and impact energy for ASR-damaged mortars.

It should be noted that the sideband energy corresponding to the maximum impact energy for the ASR-damaged sample is nearly 10 times greater than the sideband energy caused by the same magnitude of impact energy for the linear PMMA material. It indicates that the method of sideband integration used in this research truly measures the material nonlinearity caused by ASR. The nearly flat relationship between the sideband energy due to signal processing and impact energy shown in Figure 6.5b will also not affect the calculation of slope-of-energy *D* because the quasi-constant sidebands due to signal processing will only change the intercept and not the slope of the linear relationship of Eq. (7.1).

7.2.3 Distinction between Intact Sample and ASR-damaged Sample

For a single specimen, it is proposed that the nonlinearity parameter D varies with the progressive ASR-induced damage since it is proportional to the nonlinearity material parameter β. This parameter, in turn, has been shown to be an effective indicator of nonlinear phenomena in other materials, using techniques such as harmonics generation and the modulation effect of waves. As a preliminary step to validate the proposed NWMS technique, a comparison of experimental results for an intact control specimen and a companion specimen undergoing ASR damage was carried out. Samples were prepared with the same aggregate F1, but one set was exposed to AASHTO T 303 conditions, whereas the other set was not exposed to the highly alkaline sodium hydroxide solution. Figure 7.7 shows the plot of energy relationships at different periods for both control and damaged samples. The sideband energy of the control sample remains almost constant, regardless of the increase of impact energy or increasing number of days of exposure. In contrast, the sideband energy of sample undergoing ASR showed a linear increase with the increased impact energy and the slope-of-energy D changes, presumably with the development of ASR damage. The observations in Figure 7.7 are in agreement with the prediction of NWMS method in which the sidebands are assumed to be induced by material defects and have a linear relationship with incident signals.

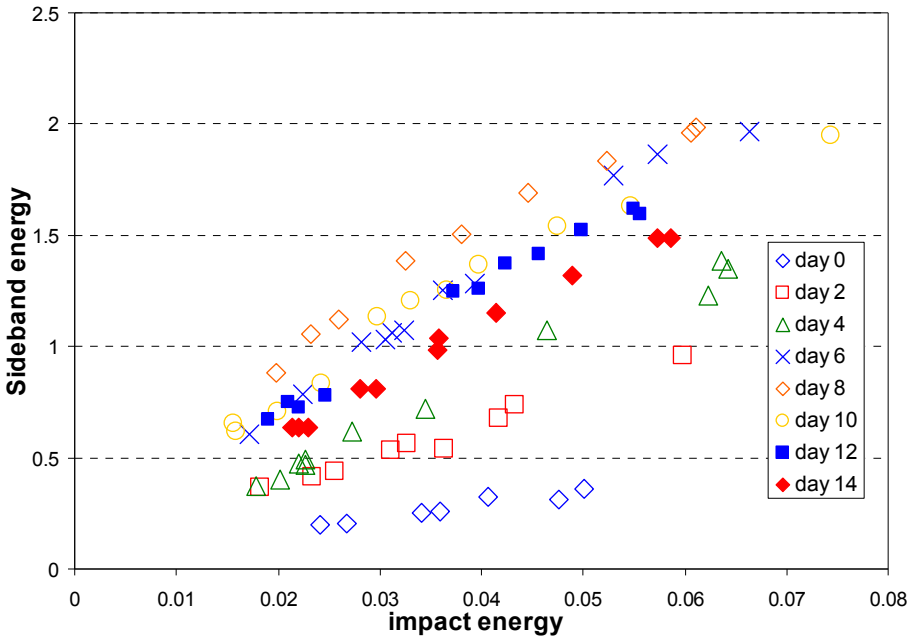

Figure 7.7(a) Energy relationship of damaged sample (aggregate F1).

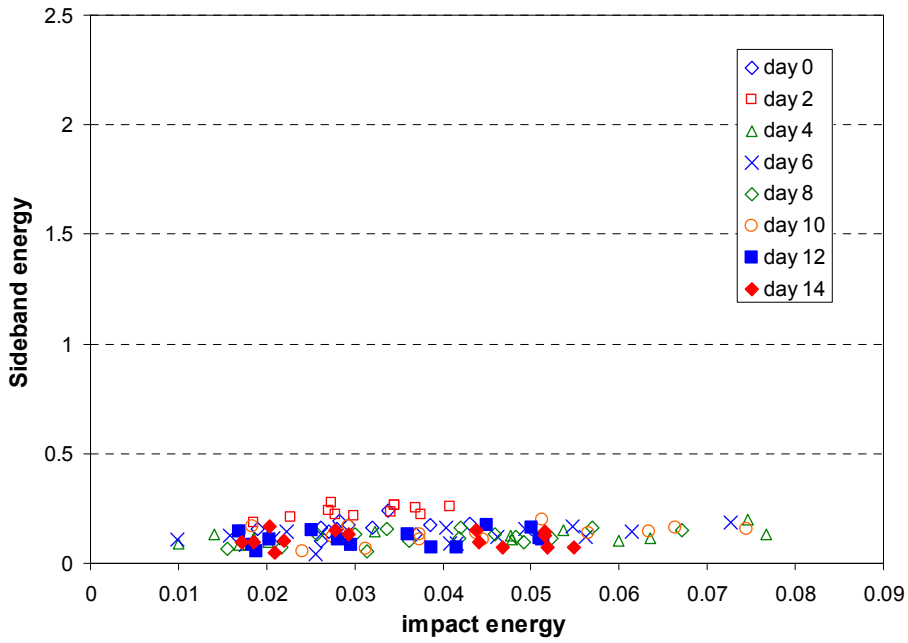

Figure 7.7(b) Energy relationship of control sample (aggregate F1).

Figure 7.8 demonstrates the relationship between the nonlinearity parameter slope of energy or *D* and duration of exposure for one of the aggregates examined (aggregate F6). Here *D* increases generally with increasing exposure time, and, hence, expansion measured using the companion samples. This direct relationship between the nonlinearity parameter *D* and exposure period further suggests the potential of the NWMS technique for the assessment of aggregate reactivity.

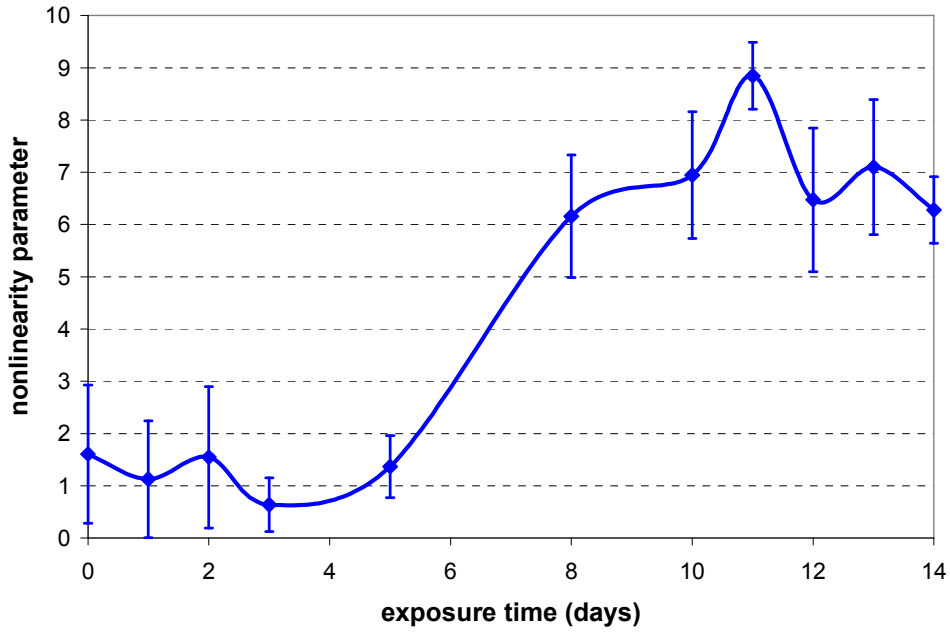

Figure 7.8 Relationship between nonlinearity parameter (D) and exposure period (aggregate F6). Standard deviation error bars for the slope of energy are also shown in the graph.

To investigate the repeatability of developed NWMS method, three specimens were cast for each aggregate and were exposed to the same storage conditions and experimental procedures. The average nonlinearity parameter *D* for the three samples for each aggregate was plotted against the exposure time up to 14 days. Figure 7.8 shows this plot for aggregate F6. The standard deviations in these results indicate good repeatability

for the NWMS method. It was seen that a larger measurement variation typically occurred at the early stages (0-2 days of exposure) of ASR damage where the material nonlinearity was still insignificant. The variation also increased after the damage substantially developed in the mortar bars.

7.2.4 Differentiation of Different Aggregates with Varying Reactivity

Subsequently, the NWMS method was used to examine the alkali-reactivity of three different aggregates F1, F4 and F6, of varying reactivity, to determine if the NWMS method could distinguish among their reactivities, as determined by expansion measurements. Figure 7.9 shows the variation of nonlinearity parameter *D* with exposure period for these three aggregates up to 14 days of exposure.

These three curves show that the nonlinearity parameter *D* generally increases with the accumulating ASR damage. For the most reactive aggregate F1, nonlinearity parameter *D* increases sharply during the initial days of exposure and then decreases after day 4. This decrease occurs after the expansion exceeded 0.1%, which is commonly considered to coincide with cracking in mortar and is often used as a limit between innocuous and potentially reactive aggregate in the mortar bar tests. In the final stages of the 14-day exposure period, the nonlinearity parameter *D* for aggregate F1 becomes irregular. This change in the relationship between *D* and exposure is possibly due to the formation of extensive cracks and paste/aggregate debonding in the mortar bars. This suggests that for very reactive aggregate, such as aggregate F1, NWMS measurements should be made every day at very early ages to accurately characterize behavior.

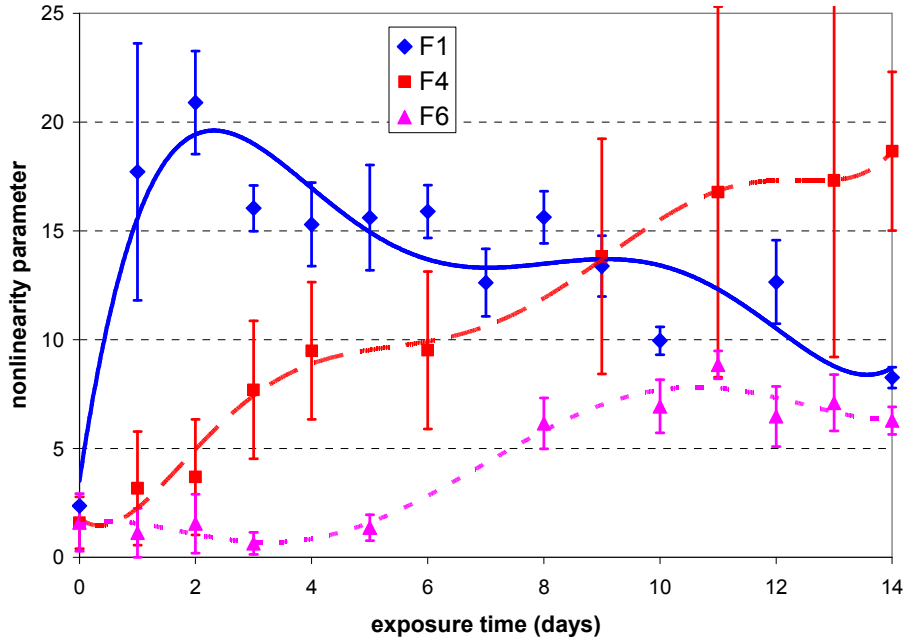

Figure 7.9 Correlation between nonlinearity parameter (D) and alkali-reactivity of three aggregates of varying reactivity over a 14-day exposure period.

The increase in nonlinearity parameter *D* with exposure time occurs differently for the three aggregates, suggesting that NWMS is able to distinguish among various aggregate reactivities. For instance, the nonlinearity parameter *D* for aggregate F1 increases rapidly within 2 days of exposure to the sodium hydroxide solution and reaches a value of 20. The nonlinearity parameter *D* of aggregate F4, on the other hand, comes close to this level only at the end of experimental period of 14 days, when the nonlinearity parameter *D* of aggregate F6 remains less than 10. The increase of nonlinearity parameter for three aggregates coincides with the distinction in their reactivity known by standard expansion measurements (Figure 3.7). Hence these results show that the nonlinearity parameter *D* (slope-of-energy), based on the proposed NWMS technique, is able to differentiate the alkali-reactivity of these aggregates.

In addition to this distinction of various aggregates, Figure 7.9 also indicates that the NWMS technique can accelerate the identification of ASR in mortar bars compared to conventional AMBT. It can be observed in the plot that the nonlinearity parameter *D* of highly reactive aggregate F1 has a tremendous increase as early as one day of exposure to sodium hydroxide solution. The nonlinearity parameter *D* of moderately reactive aggregate F4 also showed a considerable increase in energy slope value within 4 days of exposure, whereas aggregate F6, which showed low ASR reactivity, presents a lesser increase of *D* even at 6 days of exposure. Based upon this clear difference in ultrasonic parameters measured at early ages, it appears that the NWMS technique may be able to detect the alkali-reactivity of a specific aggregate as early as 4 days of exposure to AMBT conditions.

It is necessary to correlate the results from NWMS measurements with previous petrographic images in Chapter 4. As recalled in Figure 4.4b, at 2 days of exposure, formation of an apparent alkali-silica gel was first observed around the aggregate particles for aggregate F1. During the same initial two-day period, the ultrasonic tests showed that the nonlinearity parameter D increased continuously. This indicates that NWMS method is sensitive to the early formation of alkali-silica gel in the mortar bars and that the formation of the gel presumably increases the energy slope value.

After 4 days of exposure, microcracks were observed around aggregate particles in this sample and extensively grew, as indicated by arrows in Figure 4.4c-f. During this same period, in the ultrasonic measurements, the nonlinearity parameter D values started to decrease after the rapid increase for the initial 2 days of exposure. One of the possible explanations is that the material nonlinearity is dependent of the developing cracks. A

previous research [95] found that the material nonlinearity was decreased when the microcracks in materials became more open. Thus for the highly reactive aggregate F1, the growth of microcracks after 4 days could have a reverse effect on the material nonlinearity. More discussion on the correlation between the variation of measured nonlinearity parameters and the changed microstructure of materials shown in the petrographic images are provided in Chapter 8.

CHAPTER 8

NONLINEAR IMPACT RESONANCE ACOUSTIC SPECTROSCOPY

8.1 Experimental Setup

In this chapter, the nonlinear impact resonance acoustic spectroscopy (NIRAS) is presented for the ASR characterization [96]. NIRAS is an experimental application of nonlinear impact resonance theory described in Chapter 6. In the NIRAS tests, mortar bar samples were cut to a length of 254 mm The samples were then fixed at one end (embedded length was 25.4 mm using a clamping device and free at the other end so that it was a beam with a fixed-free boundary condition which is consistent with the boundary conditions set in Section 6.3. The cantilever length of the beam was 228.6 mm, and its thickness was 25.4 mm. An accelerometer was affixed to one surface near the free end, and the impact energy was applied in the middle of the opposite surface with an instrumented hammer. The impact signal and received vibration signal were captured and recorded by a digital oscilloscope. The experimental setup is schematically shown in Figure 8.1, and a photograph of experimental instrumentation is shown in Figure 8.2.

In previous research using the nonlinear resonance methods [28, 90], the resonance modes of the samples were excited by sweeping through a wide frequency range around the specific resonance mode of interest. Therefore, in such experiments, the value of resonance modes has to be known a priori in order to determine the appropriate frequency sweeping range. In contrast, for the proposed NIRAS technique, the resonance modes of mortar samples are generated simply by an impact excitation with an

instrumented hammer, and an initial estimate is not needed. This is an advantage, particularly since the resonance mode may change due to increasing damage in the sample with increasing exposure, such as the ASR deterioration in this research. Another advantage of the NIRAS technique is that multiple resonance modes can be obtained from the same signal generated by a single impact. NIRAS is more efficient than other techniques using continuous sine waves as excitation sources, in which different transducers with different center frequencies are needed to excite multiple resonance modes.

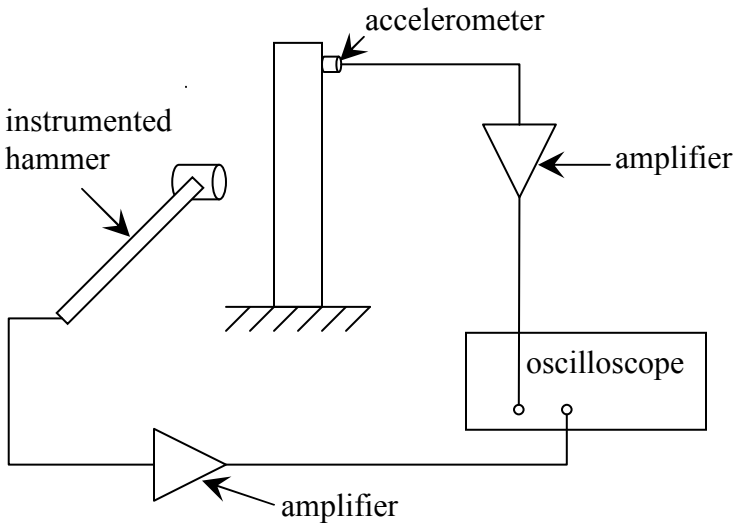

Figure 8.1 A schematic diagram of NIRAS experimental setup.

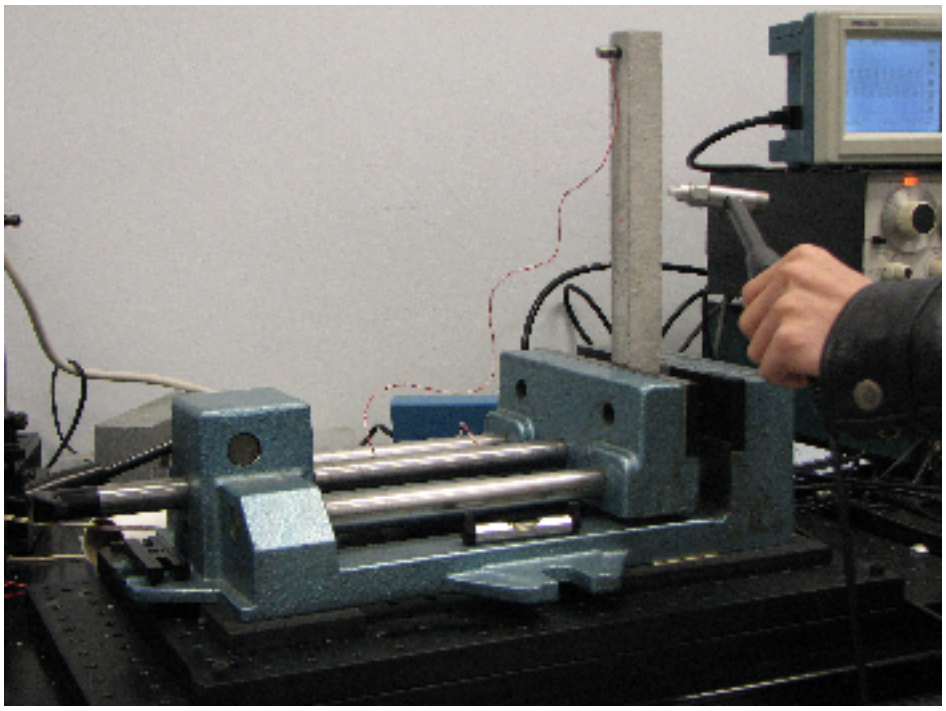

Figure 8.2 Photograph of NIRAS experimental instrumentation.

8.2 Linearity of NIRAS Experimental Setup

In general, there are a number of sources of nonlinearity inherent in the experimental setup, and these nonlinearities can be coupled with the material nonlinearity that is proposed to be measured. For example, since samples are fixed by a clamping device, the contacting surfaces (between the sample and the fixture) can produce a strong nonlinearity if not properly dealt with. In addition, all electronic devices and cables can produce spurious electrical nonlinearity. Therefore, it is important, at the beginning of the experiment, to confirm the linearity of the measurement system as a whole to ensure that only the nonlinearity of the mortar samples, and not the instrumentation nonlinearity, is being measured.

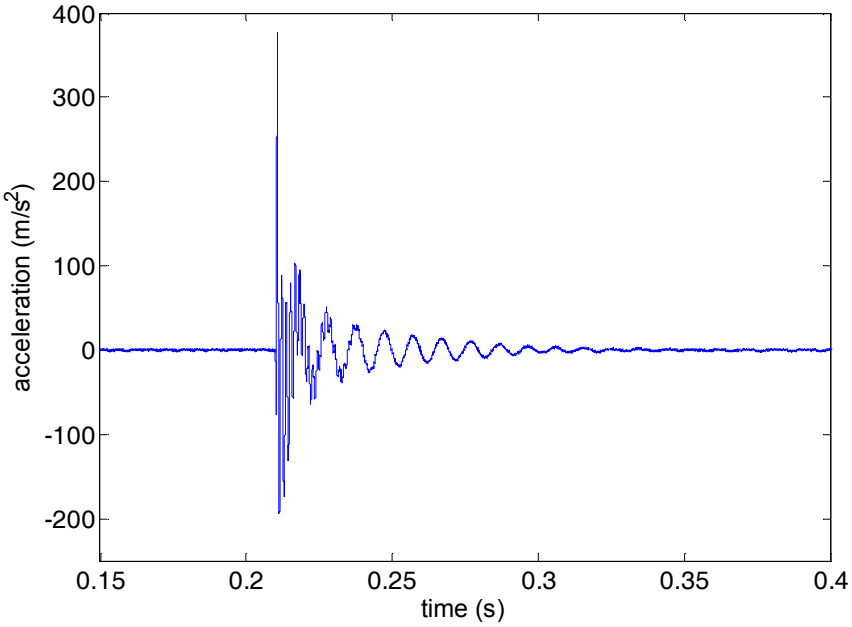

Figure 8.3 A typical vibration signal in time domain.

A polymethyl methacrylate (PMMA) slender bar, of approximately the same dimension as the mortar samples, was used in the system linearity test, assuming that the PMMA is linear at the same level of displacement (or excitation). A shift of resonance frequency of the PMMA bar will appear if any nonlinearity exists in the experiment setup or electronic devices. Twenty vibration signals for varying impact energies were acquired. A representative time-domain vibration signal from the PMMA bar is shown in Figure 8.3. The frequency spectra of these signals were obtained with the Fast Fourier Transform (FFT), and the spectra around the first resonance mode are shown in Figure 8.4. It is seen that the resonance frequency at different impact energies remains unchanged. This demonstrates that the total nonlinearity from the mechanical fixture and electronic devices is negligibly small, and thus the measured nonlinearity for mortar bars presented later in this paper is only due to the material, plus any damage to the material.

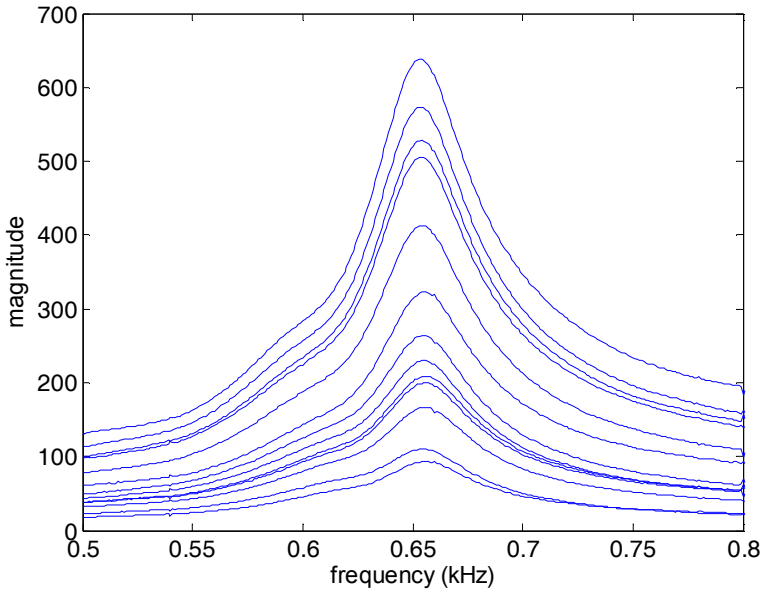

Figure 8.4 Resonance of PMMA bar for different levels of impact energy.

8.3 Results and Discussion of Mortar Samples

In NIRAS tests for mortar samples, aggregates F1, F4, F6 and F7 were used and three samples were cast for each aggregate. The sample preparation in NIRAS tests is the same as in AMBT measurements.

8.3.1 Sensitivity of NIRAS to ASR-induced Damage

The sensitivity of NIRAS to ASR-induced damage is examined by comparing measurements made on an ASR-damaged and an undamaged mortar bar. These results are then compared with the results from a conventional linear resonance vibration technique.

Two mortar samples were cast with aggregate F1 which is known to be highly reactive by AMBT expansion tests. Both were proportioned and cured per AASHTO T 303, and while one was stored in 80°C 1N NaOH solution to induce ASR damage, the other was immersed in deionized water at 80°C as a control specimen. Again in each test, twenty impacts were imparted to each bar with different energies, and the experiment was repeated at various intervals with the increasing exposure period. Figure 8.5 shows a comparison of the resonance frequencies for the control sample and damaged sample after 4 days of exposure. It is seen in Figure 8.5a, for the control sample, that there is a minor decrease of the resonance frequency over the increased excitation; this may be caused by the intrinsic nonlinearity of the mortar. In contrast, the shift of resonance frequency in the damaged sample is much more pronounced as shown in Figure 8.5b. It is proposed that this observed shift in resonance frequency is due to the development of ASR damage.

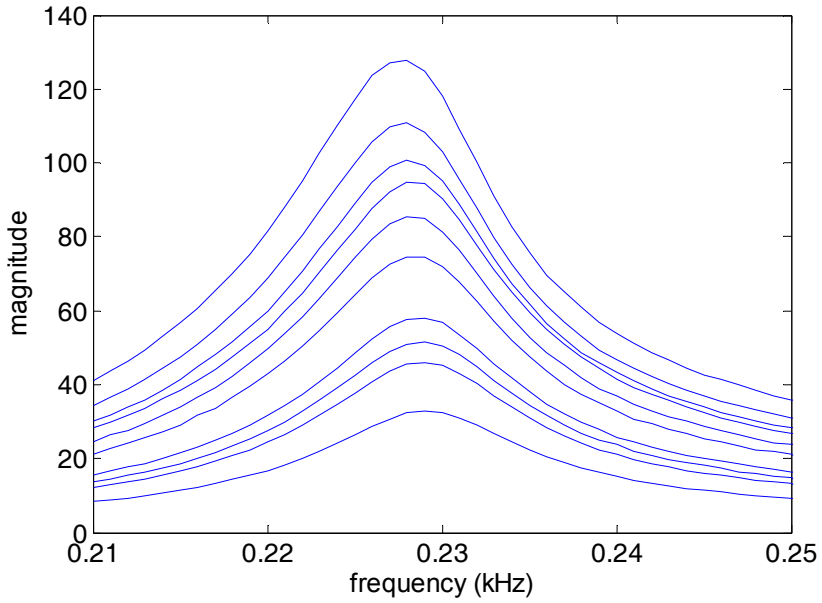

Figure 8.5(a) Resonance of intact mortar sample with increasing impact energy.

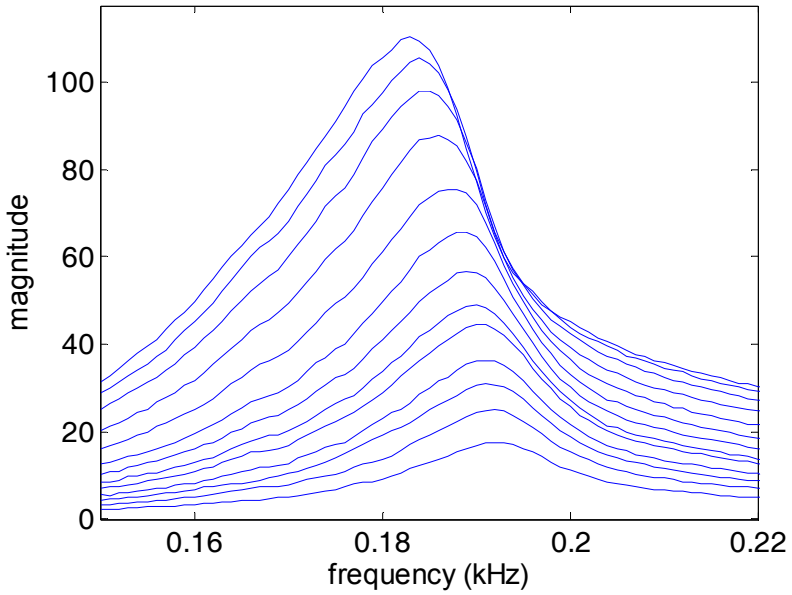

Figure 8.5(b) Resonance of damaged mortar sample with increasing impact energy.

As can be theoretically predicted, it is also observed in Figure 8.5 that the resonance frequency remains constant if the excitation is limited to values below a certain level (that is, when U in Eq. (6.30) is very small). Therefore, the resonance frequency at the smallest excitation in Figure 8.5 may be taken approximately as the linear resonance ω_0 of the sample. As a measure of nonlinearity, nonlinearity parameters can be defined as in Eq. (6.30) through a relationship between the shift of the resonance frequency $\Delta\omega = (\omega\text{-}\omega_0)$ normalized by the above-defined linear resonance frequency ω_0 and the excitation amplitude U. In addition, it is known from Eq. (6.30) that when the excitation is low, the quadratic term is negligible and the shift of resonance frequency is proportional to the excitation, where the slope corresponds approximately to the hysteresis constant λ_1.

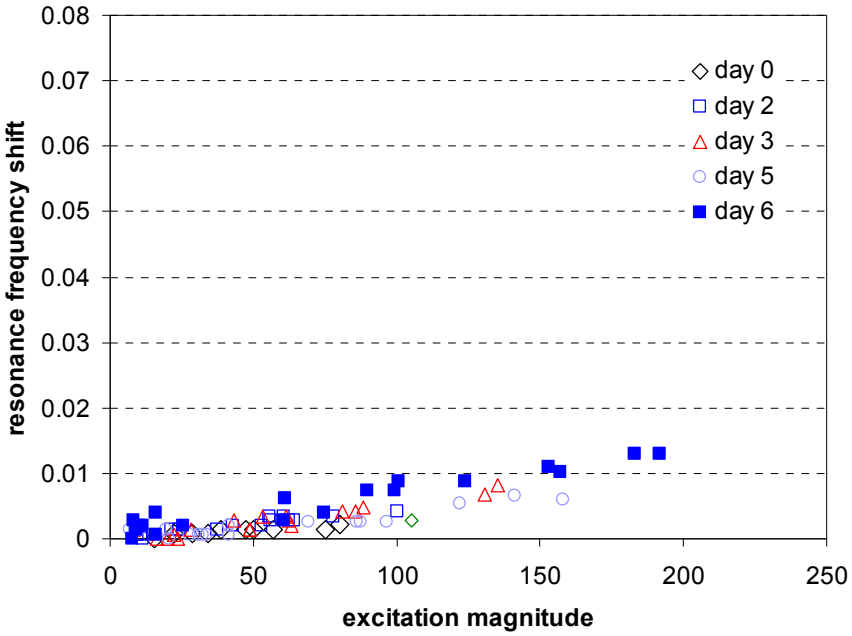

Figure 8.6(a) Resonance frequency shift versus excitation magnitude with increased exposure time for a non-damaged control sample.

Figure 8.6 presents the variation of the shifts of the resonance frequencies as a function of excitation magnitude up to 6 days of exposure time, for both the control and damaged samples. There is a clear linear relationship between the shift of the resonance frequency and the excitation magnitude for the ASR-damaged sample at every specific exposure time as shown in Figure 8.6b. The slope of this relationship, i.e., the nonlinearity parameter (being close to the hysteresis constant, λ_1), has a visible change (increase or decrease) with the increasing exposure time and, thus, with increasing ASR-induced damage. In contrast, Figure 8.6a shows that the shift of the resonance frequency has no obvious change versus excitation magnitude with an increase in exposure time. This indicates a satisfactory level of sensitivity for the increasing ASR damage in the mortar using the nonlinearity parameter obtained from this measurement.

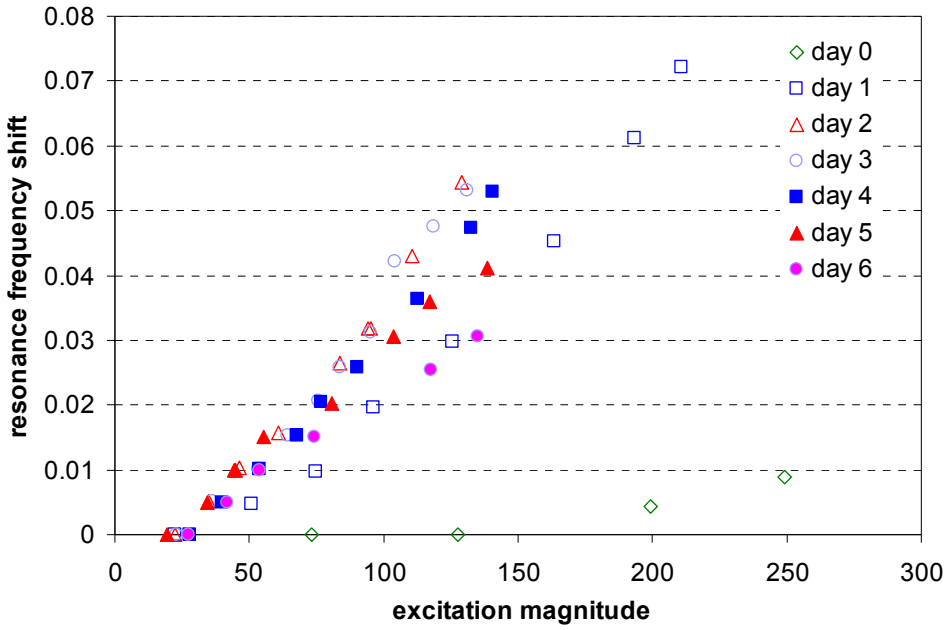

Figure 8.6(b) Resonance frequency shift versus excitation magnitude with increased exposure time for an ASR-damaged sample.

Furthermore, the sensitivity of the NIRAS technique is compared to the conventional linear vibration method. As is well-known in classical vibration theory [86], the linear resonance frequency of a sample is determined by the linear elastic modulus of the material used, plus the geometry and the boundary condition of the experimental specimen. The linear resonance frequency could thus be affected by the development of ASR damage, because ASR does induce changes in the elastic modulus of the tested specimens. Therefore, the resonance frequency at the smallest excitation on each exposure day (practically considered as the linear resonance frequency as described above) is selected as the representative parameter of the conventional linear vibration method for a comparison with the NIRAS results. Both the linear parameter (linear resonance frequency) and the nonlinearity parameter of the NIRAS technique (i.e., the slope in Figure 8.6) are normalized by their individual value before exposure (i.e., day 0)

and are plotted in Figure 8.7 up to six days of exposure time. It is observed in Figure 8.7 that the normalized linear resonance has a maximum of 10% variation, while the normalized nonlinearity parameter has an increase as much as 10 times its initial normalized value. The comparison in Figure 8.7 indicates that the proposed NIRAS technique is significantly more sensitive than the linear vibration method in quantifying ASR damage.

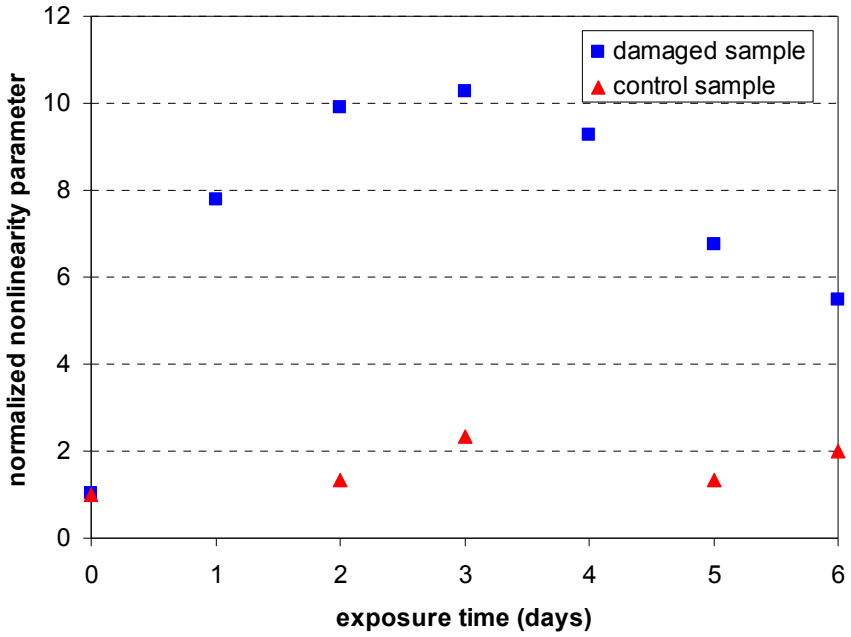

Figure 8.7(a) Sensitivity of NIRAS for differentiating ASR-damaged sample and control sample.

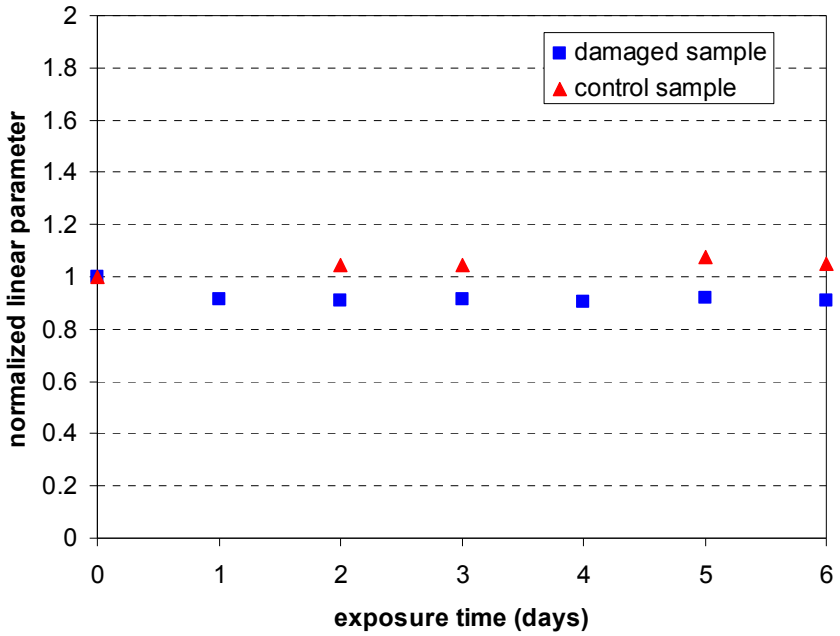

Figure 8.7(b) Sensitivity of linear resonance vibration method for differentiating ASR-damaged sample and control sample.

8.3.2 Differentiation of Aggregates with Varying Reactivity

After demonstrating that the proposed NIRAS technique can effectively differentiate the ASR-damaged sample from its intact counterpart, the NIRAS measurements are used to determine if the NIRAS technique can be used to distinguish aggregates (F1, F4, F6 and F7) with varying alkali-reactivity. Figure 8.8 shows the variation of normalized nonlinearity parameters of four aggregates over the 14-day exposure period, where the nonlinearity parameters were calculated in the same manner as in Figure 8.6, i.e., the slope of the linear relationship between the shift of the resonance frequency and excitation magnitude. The initial values of nonlinearity parameters for these four aggregates before the exposure (day 0) were slightly different, and the normalization by the initial value on day 0 was enforced for the nonlinearity parameters at each exposure age to eliminate the effect of different intrinsic material nonlinearity.

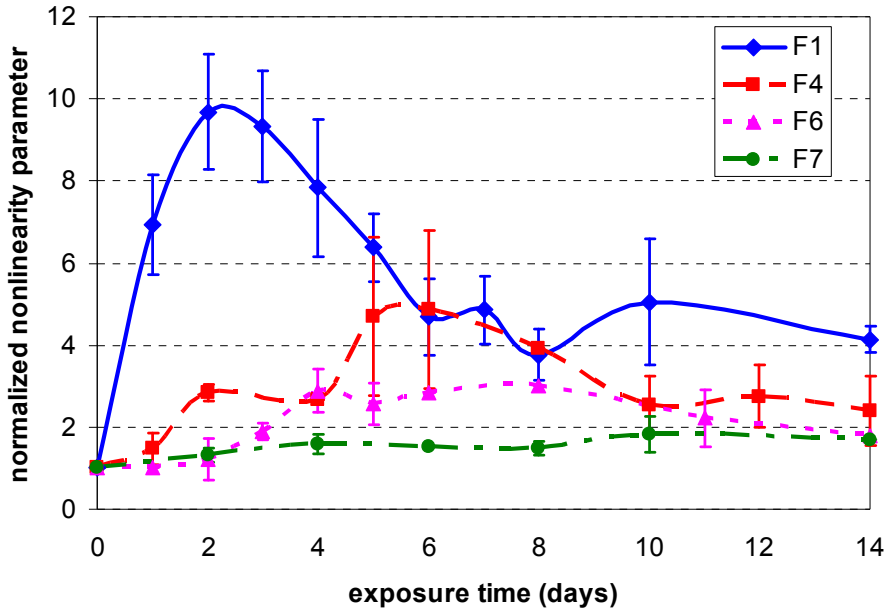

Figure 8.8 Variation of normalized nonlinearity parameter versus exposure time for mortar samples cast with four different aggregates.

First, the nonlinearity parameter of the innocuous aggregate F7 remains below a small value of 2, indicating that the material nonlinearity due to ASR throughout the exposure period did not significantly increase when compared to its initial value on day 0. The minor increase in nonlinearity parameter of aggregate F7 could be due to the heating-and-cooling cycle during tests or instrument nonlinearity. In contrast, the nonlinearity parameter of the highly reactive aggregate F1 increases rapidly during the initial 4 days of exposure, reaching nearly 10 and then decreases to a relatively stable value. The large difference of nonlinearity parameters between aggregate F1 and F7 indicates that the proposed NIRAS technique is sensitive to the ASR-induced damage of materials in these experiments, and not the other potential nonlinearity sources. The rapid increase in the nonlinearity parameter prior to day 4 for aggregate F1 indicates the

relatively rapid rate of reaction and damage with this highly reactive aggregate which is consistent with the expansion measurements in Figure 3.8, although the decrease of nonlinearity parameter after day 4 is not observed in expansion data. The highly reactive aggregate F1 and inert aggregate F7 can be considered to represent two relative extremes in behavior in this study, and their behavior observed by NIRAS is distinct at early test ages.

The nonlinearity parameters of aggregate F4 and F6 both increase steadily, but by day 6, aggregate F4 can be effectively distinguished from aggregate F6. Particularly from day 2 to day 6, the nonlinearity parameter of aggregate F4 has an average value of two times the nonlinearity parameter of aggregate F6. This relatively early differentiation of aggregate reactivity (i.e., moderate vs. marginal reactivity, based on 14-day expansion results) is one potential advantage of the developed NIRAS method. Further research is necessary to validate these results for a wide range of potentially reactive aggregates.

Together, these results highlight two key needs in terms of improving tests for aggregate screening: (1) tests are needed which are able to discriminate between aggregates of similar reactivity (e.g., moderately reactive vs. marginally reactive) and (2) tests are needed which can distinguish aggregate reactivity relatively rapidly (i.e., within short exposure durations).

8.3.3 Physical Interpretation of NIRAS Results

The NIRAS technique has been shown to distinguish ASR-damaged samples from undamaged samples and to distinguish among aggregates of varying alkali-silica reactivity. The measured nonlinearity parameter was observed to increase with increasing

damage due to ASR. But, as seen in Figure 8.8, the nonlinearity parameters of aggregate F1 and F4 do not monotonically increase with exposure, which is inconsistent with the increasing expansion measured over time for these aggregates (Figure 3.8). Thus, it is imperative to inter-relate the variation of the nonlinearity parameter with the changes occurring in the specimen during progressive ASR. The pattern of the changing nonlinearity parameter for the two more reactive aggregates F1 and F4 and the results obtained from microscopy will be used to relate the nonlinearity results with the observations of physical changes occurring in the microstructure.

The nonlinearity parameter of aggregate F1 reaches its peak by 4 days of exposure and decreases gradually afterwards, while the nonlinearity parameter of aggregate F4 has a slower progression, reaching the maximum value by 6 days of exposure, and decreasing and apparently stabilizing at low value by 10 days of exposure. In fact, the initial increase and eventual decrease of a different, complementary nonlinearity parameter (cubic coefficient β) of the same aggregate F1 was observed in Chapter 7, when using a different nonlinear technique based upon wave modulation. It has been suggested in Chapter 7 that the ASR-induced changes observed in the petrographic analysis in Chapter 5, such as the ASR gel formation and subsequent debonding at the aggregate-paste interface, as well as cracking in the paste, may be responsible for the initial increase and eventual decrease of the nonlinearity parameter.

Again, the change of material microstructure at different stages of ASR development may also contribute to the increase-then-decrease of the hysteresis parameter observed by the NIRAS technique in Figure 8.8. Recall that researchers have established that the ASR gel product has unique elastic properties which differ from those

of the aggregates and paste [26]. It may be proposed that as the amount of the ASR gel formed increases, it contributes to an increase in the overall heterogeneity of the mortar, resulting in an increase in the measured nonlinearity parameter. In addition, it has been found that the nonlinearity is closely related with the closing/opening of microcracks; the nonlinearity of microcracks is highest when the faces of a given microcrack are almost closed [94], which corresponds to initiation of microcracks. With expansion of ASR gel, new microcracks develop and grow in the paste and aggregate and interfacial debonding increases. Thus, the formation of microcracks during ASR could also contribute to the increase of nonlinearity parameter.

The cause of the relative post-peak decrease in nonlinearity parameter is not fully understood, but is likely the result of modifications to the material structure and properties. Two potential explanations for these measurements are presented from the perspective of gel formation and microcrack growth, respectively. First, the formation of crystalline products within the ASR gel due to interactions with calcium ions or carbonation, which could cause an overall stiffening effect, could cause the decrease of material nonlinearity. In addition, with continued soaking in high-temperature alkaline solutions, the ASR gel – which may be responsible for a large portion of the measured nonlinearity – becomes more fluid-like and/or may be largely lost to the surrounding solution, diminishing its influence on the measured nonlinearity. With respect to crack growth, previous research has found that the material nonlinearity becomes smaller when microcracks are open or not tightly closed [94]. Here, the continued formation and expansion of ASR gel can lead to widening of microcracks and coalescence into larger cracks. Crack widening was observed in mortar bars undergoing progressive ASR was

observed in the previous petrographic analysis in Chapter 4 for both aggregates F1 and F4.

It should be recognized, however, that ASR in cement-based materials is a complex process resulting in physical, chemical, and mechanical changes to the affected material. Such changes can have different and interactive effects on the measured acoustic nonlinearity, and it may be that the spatial variations in the microstructure (i.e., ASR-induced damage in the paste vs. aggregate) may influence the measured nonlinearity parameter. For example, Ben Haha et al. [61] found that the cracks developed within aggregates can slow the rate of expansion in laboratory samples; this decline in reaction rate could affect the measured nonlinearity measurements as well. However, cracking with in the aggregate particles was not commonly observed in these mortars, perhaps due to the lack of restraint afforded by the current petrographic set-up, and thus a definitive relationship between the location of the cracking and the measured nonlinearity parameter is not possible at this time. An apparent temporal correlation was found between the loss or apparent increased porosity (and presumable decreased modulus and strength) of highly reactive aggregate particles (Figure 4.5) and a decrease in the nonlinearity parameter.

Thus, from the previous discussions, it is believed that the increase in the nonlinearity parameter is strongly dependent on the initial formation of gel and microcracks. With the progress of ASR, the initially formed cracks widen, and the gel grown more fluid-like (under AMBT conditions) resulting in a lesser contribution (or even a reverse effect) on the nonlinearity parameter. This would result in a decrease of the nonlinearity parameter once the rate of reaction slows, as observed in Figure 10. In

such a scenario the nonlinearity parameter that is measured at each testing instance would correspond to the newly formed gel and microcracks (or growth rate). Hence, a cumulative value (i.e., area under the nonlinearity parameter versus exposure time graph) would approximately represent the total extent of gel and microcrack formation or a more generally-defined ASR damage state.

The variation of the cumulative nonlinearity parameter with increasing exposure duration is plotted in Figure 8.9. The cumulative nonlinearity parameters show very good correlations with measured AMBT expansions for all four aggregates, as shown in Figure 8.10. Also, it can be clearly seen from Figure 8.9 that the aggregates are distinguishable from each other as early as day 6 which was not evident in the expansion measurements (Figure 3.7). Thus, such a cumulative nonlinearity parameter can be used to differentiate aggregates of varying alkali silica reactivity in a much shorter testing duration, compared to the expansion measurements. Importantly, this cumulative nonlinearity parameter could be used to define prescriptive limits on the value of nonlinearity parameter for classifying aggregates of varying reactivity. However, further testing with a wide range of aggregates is required before these limits can be defined.

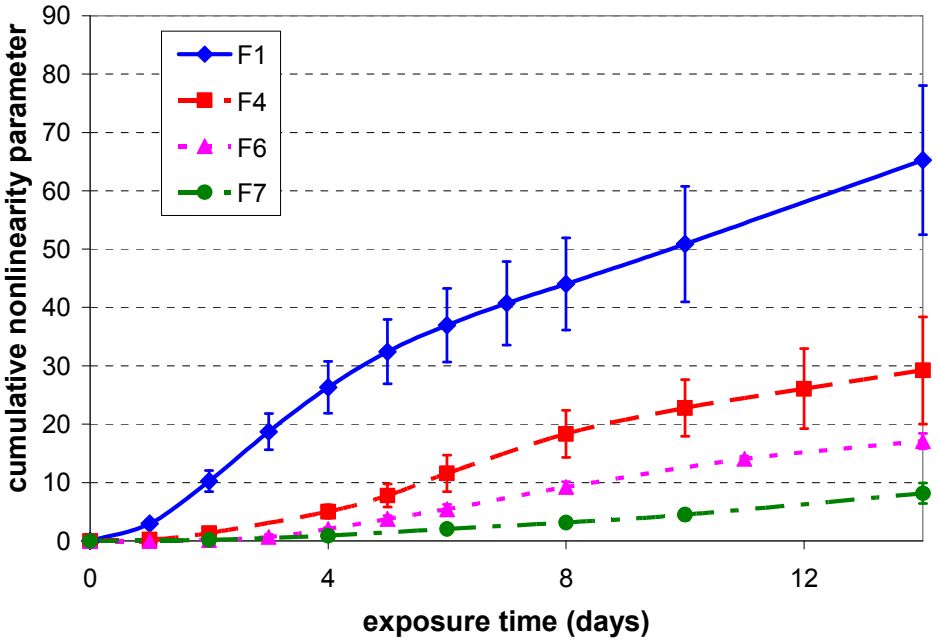

Figure 8.9 Variation of cumulative nonlinear parameter with increasing exposure time.

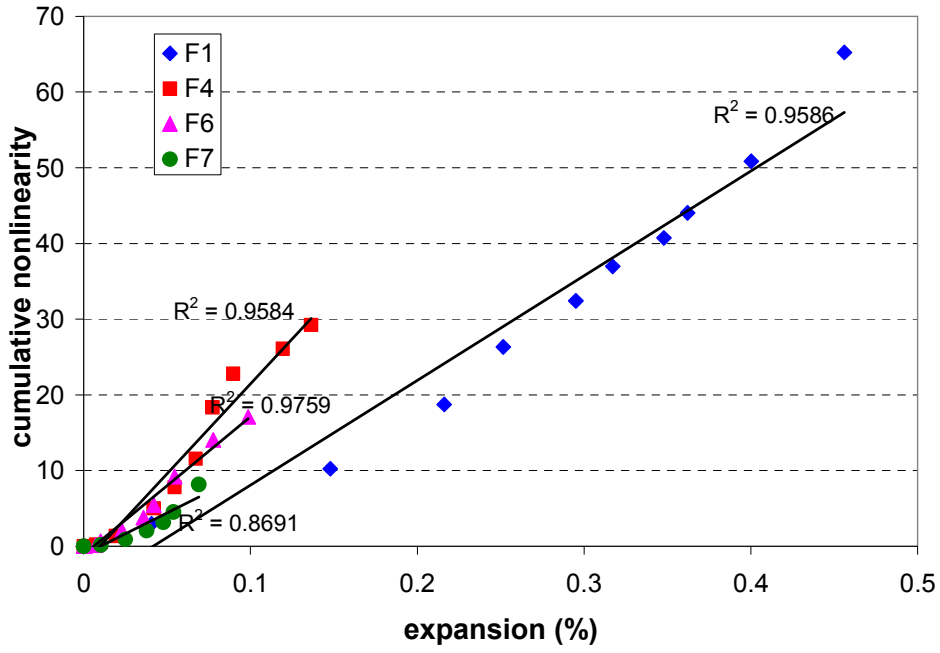

Figure 8.10 Correlation between cumulative nonlinearity parameters and AMBT expansion.

8.3.4 Comparison to Linear Measurements

It is insightful to compare the NIRAS results to the previous results obtained through linear measurement methods, presented in Chapter 5. Data in Figure 5.2 showed that aggregates the highly reactive aggregate F1 and the nonreactive aggregate F7 were relatively well distinguished by their elastic moduli, measured during compression testing. However, the elastic moduli of the marginally reactive aggregate F6 and the moderately reactive aggregate F4 were indistinguishable from each other throughout the test period. The decrease in elastic moduli over the exposure period was different for three reactive aggregates F1, F4 and F6. For marginally reactive aggregate F6 and moderately reactive aggregate F4, the maximal decrease of approximately 20% of their initial measured elastic modulus occurred at the end of 14-day exposure period. For highly reactive aggregate F1, the maximal decrease in elastic modulus occurred around 4 days of exposure and was about 60% of the initial value.

Another linear measurement, the pulse velocity method, also did not differentiate well among these aggregates. In particular, as shown in Figure 5.5, the pulse velocity for aggregate the highly reactive F1 dropped at the early exposure period and recovered to a higher range, making it difficult to be distinguished from the pulse velocity for less reactive aggregate F4 and F6. In addition, the maximal change of the pulse velocity during the entire exposure period was just ~18% for the highly reactive aggregate F1.

Overall, measurements of both elastic modulus and pulse velocity have a very poor correlation with the expansion results. Although the early drop of both elastic modulus and pulse velocity correlate well with the rapid increase in expansion of aggregate F1 for the first 4 days, the correlation between these two measurements and

increased expansion is generally not good. In addition, both elastic modulus and pulse velocity measurements lack a good differentiation between the moderately reactive aggregate F4 and marginally reactive aggregate F6.

In contrast, the cumulative nonlinearity parameter plotted in Figure 8.9 demonstrated a much better distinction among the tested aggregates. All four aggregates were well separated in an order of their corresponding ASR expansion after 6 days of exposure. The increase of cumulative nonlinearity parameter throughout the exposure period is significant compared to the change of linear parameters mentioned above. For example, the cumulative nonlinearity parameter at the end of 14 days for aggregate F1 is as high as 60 times the initial value.

The comparison between NIRAS experimental results and results from linear measurements demonstrates that nonlinearity parameters are much more sensitive to the material degradation than the linear parameters. The experimental techniques based on nonlinear acoustics/ultrasonics are advantageous to quantitatively characterize damage in materials. In the case of deleterious reactions, such methods appear to be especially advantageous for early detection of accumulating damage.

8.4 Results and Discussion of Concrete Prism Samples

The NIRAS technique was used to monitor concrete prim samples during testing as well. Three same aggregates (F1, C1 and C2) were tested using the NIRAS technique as in the previously reported CPT expansion measurements. The sample preparation and curing followed ASTM C 1293. The NIRAS measurements were performed at the same intervals as expansion measurements. Because of the limitations of the test set-up, it was

required that a small prism (25×25×250 mm.) be cut from the original concrete prism sample for each measurement. The NIRAS experiment for the small prisms is conducted in the same manner as for mortar samples introduced in Section 8.2.

Figure 8.11 presents the variation of normalized nonlinearity parameter against exposure time. It is seen that the developed NIRAS technique is able to distinguish highly reactive aggregate F1 from the other two aggregates as early as ~2-3 weeks, which is earlier than by expansion measurements alone (Figure 3.10). The nonlinearity parameter of aggregate F1 reaches its maximum (about 4) at the end of two months and then declines. The variation trend of nonlinearity parameter of aggregate F1 in Figure 8.11 is very similar to that of the same aggregate in mortar testing (Figure 8.8). However, the maximal nonlinearity parameter of concrete prism samples is only half of that of mortar bar samples, which is probably a result of different ASR damage states in AMBT and CPT tests. As described in Chapter 2, AMBT is an accelerated method and ASR damage is much more aggressive due to the aggressive exposure conditions. In contrast, concrete prism samples are stored in a less aggressive environment and the resulting ASR damage in concrete prisms is expected to be less extensive and slower to develop than that in mortar samples.

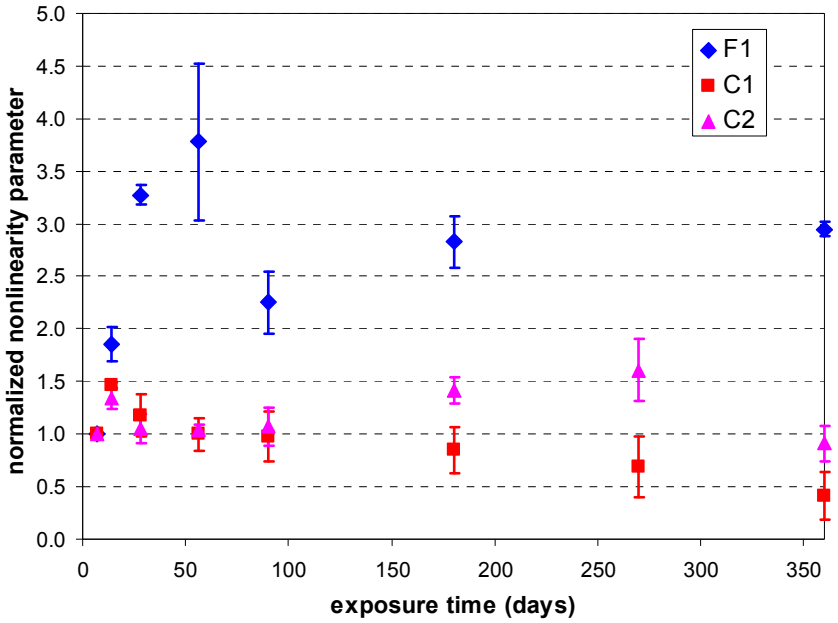

Figure 8.11 Variation of normalized nonlinearity parameter versus exposure time for concrete prism samples cast with three different aggregates.

The nonlinearity parameters of the concrete prisms prepared with coarse aggregates C1 and C2 are not separated from each other until later test ages (i.e., after 6 months) in NIRAS. However, the distinction between the more reactive aggregate C2 and the less reactive aggregate C1 provided by NIRAS is more clear and is evident earlier than in the CPT expansion data. As shown in Figure 3.3. the behavior of these two aggregates are indistinguishable until the end of the one-year test. Thus, the NIRAS technique offers a clear advantage over the expansion tests in terms identifying potentially reactive aggregates in a shorter amount of time, as well as showing a clearer distinction in behavior between these two aggregates.

Also, as shown in Figure 8.8, the corresponding mortars prepared with these sources but crushed into fine aggregates (F4 and F6) are distinguished very well by the NIRAS technique at very early test durations. Again, the contrast in NIRAS results for

the mortar samples and concrete samples may reflect the differences in the exposure conditions in the different testing regimes, as well as the reduction in aggregate size when testing coarse aggregates in concrete and crushed aggregates in mortars. Due to the less aggressive test conditions, the nonlinearity parameters of concrete prism samples cast with aggregate C1 and C2 have a smaller absolute value than their counterparts in mortar samples. Therefore, the excitation of vibrations applied for the concrete prisms has to be increased from its level for the mortar samples to experimentally obtain an equivalent nonlinearity signature (shift of resonance frequency). However, the excitation is generated by an instrumented hammer in the developed NIRAS technique and can not be increased in an unlimited way due to practical constraints (i.e. the overload may damage samples).

8.5 Effect of SCMs on NIRAS Measurements

The effect of SCMs on NIRAS measurements is studied in this section. In this preliminary investigation, the use of one SCM – a Class C fly ash as described in Table 3.6 – was examined. Class C fly ash can be used in some cases to mitigate ASR, but it is generally not as effective as Class F fly ash [11, 16]. Here, the use of Class C fly ash was considered to be advantageous as the influence of the SCM on the matrix (e.g., densification) could be examined, while still allowing for some aggregate reactivity, particularly at later test ages.

Three samples were cast with aggregate F1 and a 20% cement replacement with fly ash was used. The same sample preparation and NIRAS testing procedure for ordinary

mortar samples applied for the samples blended with fly ash. Expansion results for mortars prepared with these materials are provided in Section 3.3, Figure 3.8.

Figure 8.12 shows a comparison of NIRAS results between ordinary mortar samples and mortar samples containing fly ash. It is seen that the nonlinearity parameter of mortar samples with fly ash is substantially decreased from its corresponding value of ordinary mortar samples. The significant decrease of measured nonlinearity parameter of samples blended with fly ash shown in Figure 8.12 demonstrates the potential for fly ash to mitigate ASR since the nonlinearity parameter is used to characterize progressive ASR damage in the NIRAS technique.

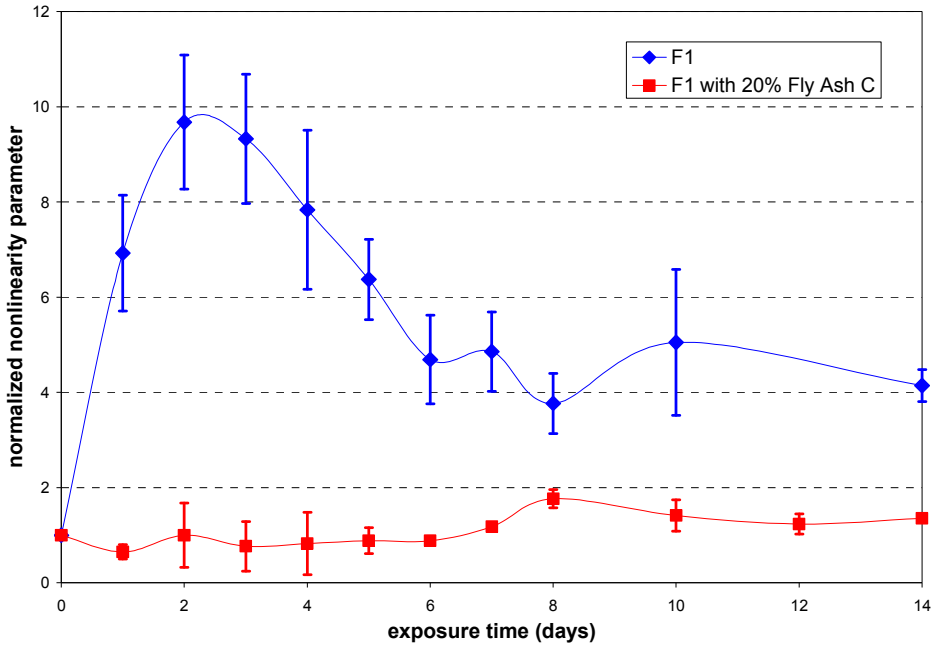

Figure 8.12 A comparison of nonlinearity parameters between ordinary mortar samples and mortar samples blended with a Class C fly ash.

The results in Figure 8.12 show correlations with corresponding expansion data in Figure 3.8, particularly at the early test age. In both data sets, the mitigation afforded by the fly ash addition is apparent within 2 days (i.e., the initial NIRAS measurement and

the second expansion reading). The nonlinearity parameter of samples blended with fly ash has a slight increase from day 6 to day 8. No further increase in the nonlinearity parameter is found after day 8 although the AMBT expansion does just exceed 0.1% by 14-days, indicating that the nonlinearity parameter in NIRAS might have different response to the fly ash addition from the AMBT expansion at the late test age. Further research, however, should consider the influence of varying amounts and types of SCMs on NIRAS measurements for mortar samples.

8.6 Effect of Aggregate Angularity and Gradation on NIRAS Results

Because defects in cement-based materials are often associated with the aggregate/paste interface and because angular aggregates can act as stress-raisers, or points where cracks could be initiated, it is useful to examine how variations in aggregate gradation (or size distribution) and angularity influence NIRAS measurements. Here, the behavior of three non-reactive aggregates, aggregates F7, F8 and F9, were examined; their AMBT expansions were shown in Figure 3.8.

First, the description of aggregate size distribution and aggregate angularity is presented. The particles of aggregate F7 are generally angular. The particles of aggregate F8 and F9 are generally more ring-shaped (less angular) compared to those of aggregate F7. A generally-accepted parameter, fineness modulus, was used to quantitatively describe the size distribution of particles in aggregates, but it has to be noted that the fineness modulus of each aggregate in its natural state is different. For example, the fineness moduli of aggregates F7 and F9 in the natural state are 2.91 and 2.35, respectively. To study the effect of fineness modulus on NIRAS measurements,

aggregate F8 was thus graded to two different sets, which had the same fineness modulus as F7 and F9.

The variations of nonlinearity parameters of aggregate F7, F9 and F8 in two cases of different fineness moduli are plotted together in Figure 8.13. Except for aggregate F7, there is a large increase of nonlinearity parameter in the middle of test period in other three cases. It is seen that variation pattern of nonlinearity parameter for aggregate F8 is very similar in both cases of fineness modulus 2.9 and fineness modulus 2.35. The nonlinearity parameter of aggregate F9 has a similar curve with that of aggregate F8 but the peak value is reached 3 days later, which could be caused by the slight difference in the alkali-reactivity of aggregates. The results from aggregate F8 and F9 indicate that the gradation of aggregates may not have significant effects on the variation of nonlinearity parameter measured in the NIRAS technique. It is interesting to observe that the nonlinearity parameter of aggregate F7 has a very flat curve. Since aggregate F7 is the only tested aggregate having an angular shape, the different variation pattern of aggregate F7 from that of aggregates F8 and F9 is more likely due to the aggregate angularity.

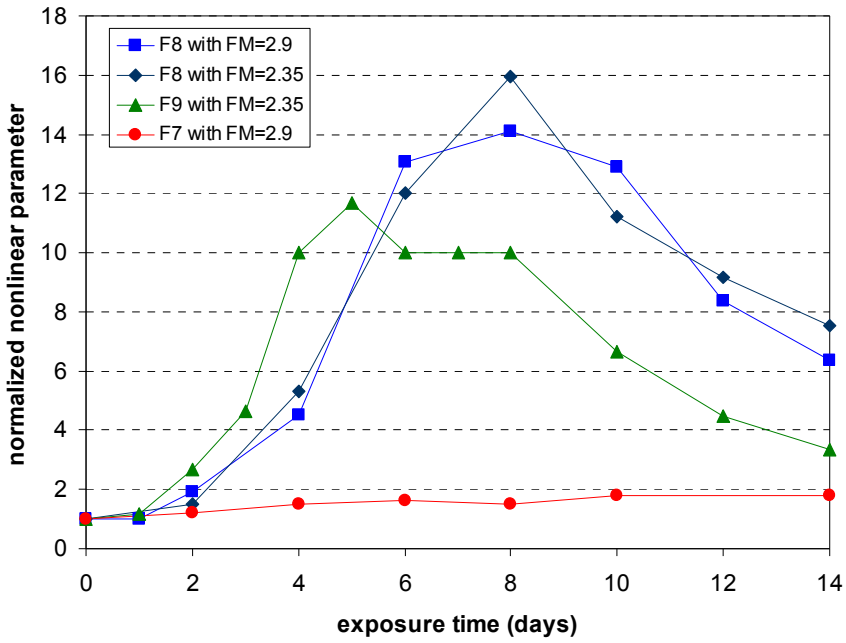

Figure 8.13 Comparison of variation of nonlinearity parameters for three different non-reactive aggregates, showing that the aggregate angularity may be the main reason for the difference.

8.7 Modeling of NIRAS for Mortar Samples

In this section, a numerical simulation is implemented using the analytical model proposed in Chapter 5 for the developed NIRAS technique. Experimental resonance curves under different impact excitation are simulated based on a robust fitting procedure.

The experimental data used in the simulations come from NIRAS measurements of a mortar sample cast with aggregate F1. Two significant cases are studied in the simulations; when the sample is in the intact condition and when the sample is in an ASR-damaged condition.

The simulating resonance curves are based on the analytical solution of NIRAS technique as in Eq. (6.28). A fitting procedure is implemented as below to generate a

series of resonance curves corresponding to increased excitation force $\tilde{F}$. As shown in Eq. (6.33), the downward shift of resonance frequency is manipulated by two nonlinear parameters λ_1 and λ_2, which are assumed as the indictor of internal damage condition of materials. These nonlinear parameters are thus increased with the growing damage of the specimen. While at a specific material state (intact or damaged), the nonlinear parameters will not change with the increased excitation magnitude. Therefore, the nonlinear parameters are fixed in the numerical implementation for the different impact excitation input, and the values are determined by the fitting of resonance curve at the lowest excitation magnitude. Following this fitting principle, λ_1 and λ_2 for the intact sample are chosen as $\lambda_1 = -0.01$ and $\lambda_2 = -0.001$. The value of quality factor Q and impact force $\tilde{F}$ are also selected based on the best fitting of the lowest resonance curve. The Q factor selected here is 19, which is consistent with the value of quality factor for concrete materials in other experimental studies [97].

For the resonance curves at larger excitations, the quality factor Q remains the same value in the fitting procedure, which indicates that the attenuation on vibrations is independent of excitation magnitudes when the material is not damaged yet. The impact force $\tilde{F}$ is adjusted in the fitting procedure based on the ratios of corresponding excitation magnitude over the lowest excitation. The comparison between experimental data and analytical results for the sample in the undamaged condition is seen in Figure 8.13, where the blue solid lines refer to the simulated results and red dashed lines represent the experimental results. Using the approximated nonlinear parameters by fitting the resonance curve at the lowest excitation, analytical results in Figure 8.13 show

a very good match with experimental data for the resonance curves subjected to larger impact excitations.

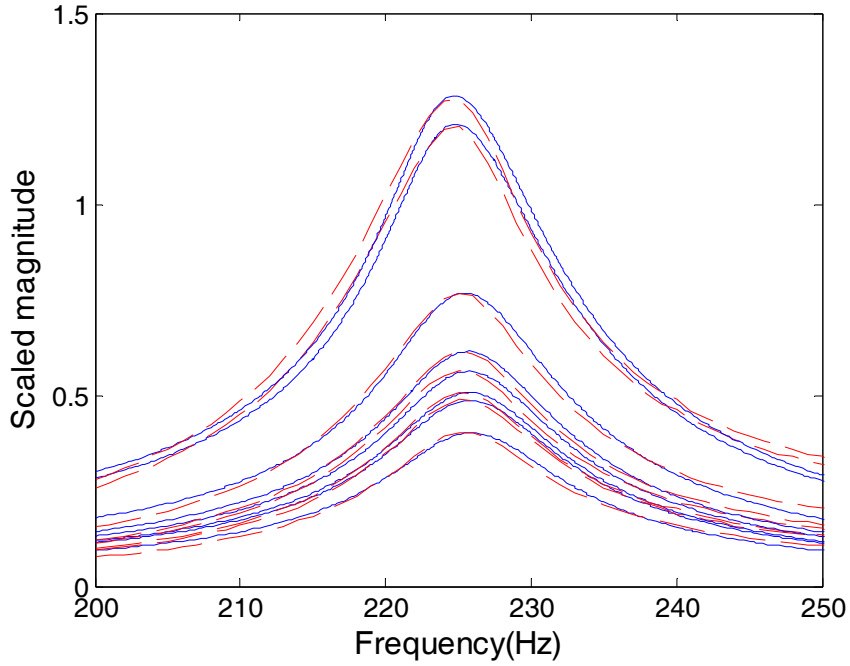

Figure 8.14 A comparison of experimental and simulated resonance curves of a mortar sample cast with aggregate F1 in intact state.

The simulations for resonance curves of damaged mortar sample are conducted in a similar manner. Several experimental studies indicated that the hysteretic parameter is dominant in the nonlinearity effect if the excitation is not very large for samples made of brittle materials such as concrete and rock [28, 84]. The nonlinearity parameter related to anharmonicity λ_2 for the damaged sample is thus assumed to remain the same value as for the intact sample ($\lambda_2 = -0.001$). Again the hysteretic parameter and quality factor are selected according to the fitting of resonance curve at the lowest excitation magnitude and they are $\lambda_1 = -0.04$ and $Q = 19$. Experimental results shown in Figure 8.14 (red dashed

line) indicates that the width of resonance curve becomes larger with increasing impact excitation. This relationship means the attenuation effect is increased and the quality factor Q of the damaged sample becomes smaller accordingly with the increased excitation. Therefore, simulations for the damaged sample are more complicated than simulations for the intact case since the quality factor Q must be adjusted for each impact force in the fitting procedure.

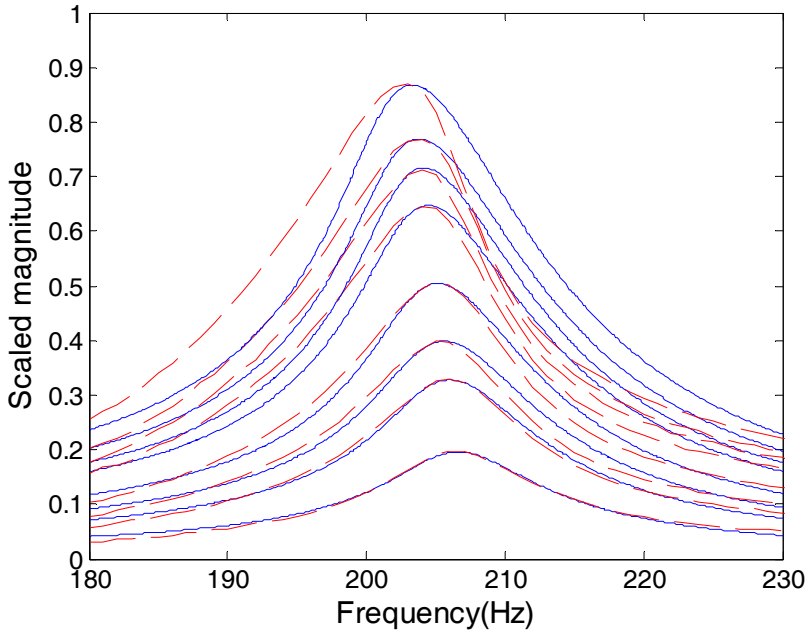

Figure 8.15 A comparison of experimental and simulated resonance curves of a mortar sample cast with aggregate F1 in ASR-damaged state.

The comparison between experimental data and analytical results for the damaged sample is shown in Figure 8.14. It is seen that the downward shift of resonance frequency in both experimental (red dashed lines) and simulation results (blue solid lines) is pronounced due to the degradation of materials. With the nonlinear parameters specified above, simulation results locate resonance frequencies shown in experimental data very well for each excitation magnitude. The shape of analytical and experimental resonance

curves matches each other well when the excitation is relatively small, and there are some distortions when the excitation becomes large.

CHAPTER 9

CONCLUSIONS AND RECOMMENDATIONS

9.1 Conclusions

This multi-disciplinary research is the first work to provide a rapid assessment of alkali-reactivity of aggregates and aggregate/paste combinations based on nonlinear acoustics. This research was conducted from three major aspects, theoretical models, conventional test methods for ASR, and nonlinear acoustic experiment.

9.1.1 Theoretical Models

Assuming a nonlinear constitutive relation for the cement-based materials during ASR damage, two theoretical models were established for the nonlinear wave modulation theory and nonlinear resonance frequency theory, respectively. The key findings from the derivation of theoretical models are

- Two propagating waves interact with each other when the propagation medium does not obey a linear constitutive relation. When the two incident waves have different frequencies, extra frequency components occur and the amplitude of extra frequency components is proportional to the cubic parameter of material nonlinearity and the amplitudes of incident signals.
- Resonance frequency of transverse vibrations is dependent of the vibration excitation if the material is nonlinear. There is a downward shift of resonance frequency with respect to the increased excitation amplitude for brittle materials

such as concrete and rock. When the excitation is under a relatively low level, the relative shift of resonance frequency has a linear relation with the amplitude of excitation. The slope of this linearity is proportional to the hysteresis parameter of brittle materials.

9.1.2 Conventional Test Methods for ASR

Four conventional test methods for ASR were used in this research, including expansion measurements, Young's modulus measurements in compression tests, ultrasonic pulse velocity measurements and petrographic analysis. The expansion measurements were conducted for both mortar samples and concrete samples. The other three techniques were only used for mortar samples. The key findings and conclusions from conventional ASR test methods are listed as below

- The AMBT expansion measurement is able to differentiate highly reactive aggregates well from other aggregates, even at the early age of tests. For example, the expansions of highly reactive aggregate F1 at 2 days and 4 days are about 0.15% and 0.25%, which are at least 4 times expansions of any other aggregates tested at the same age. However, the AMBT expansion method does not have a good distinction for aggregates having similar reactivity, particularly at the early test age. For example, expansions of marginally reactive aggregate F6 and non-reactive aggregate F7 can hardly be differentiated until 8 days.
- The CPT expansion measurement is also able to distinguish highly reactive aggregates from others rapidly. For example, the expansion of highly reactive aggregate F1 is about 0.2% at 2 months while expansions of moderately reactive

aggregate C1 and C2 are less than 0.01% at the same test age. Aggregates C1 and C2 are not distinguished from each other until 9 months.

- Young's modulus measured in compression tests shows a good distinction for non-reactive aggregate F7 and highly reactive aggregate F1. But moderately reactive aggregate F4 and marginally reactive aggregate F6 are indistinguishable during the entire test period.
- Non-reactive aggregate F7 is well distinguished from other aggregates in the measurements of ultrasonic pulse velocity. Pulse velocity of highly reactive aggregate F1 has a rapid drop during the first 4 days and then increases back in between aggregates F4 and F6.
- Petrographic results indicate that microscopic analysis can be a supplementary tool for the identification of ASR damage. For example, the quick observation of ASR-induced microcracking in samples cast with aggregate F1 is consistent with the rapid increase in AMBT expansion measurements during the first 4 days.
- The decrease of Young's modulus and ultrasonic pulse velocity has a good correlation with the rapid increase in expansion data for aggregate F1 during the first 4 days. But these two linear techniques generally are not appropriate to serve as a rapid and reliable technique for the screening of aggregates due to their overall poor correlation with expansion measurements.

9.1.3 Nonlinear Acoustic Experiments

To experimentally implement the two theoretical models proposed, two nonlinear acoustic techniques (NWMS and NIRAS) were developed for the characterization of

ASR in both mortar and concrete samples, cast and exposed to ASR-inducing conditions according to standard test methods. The mitigating effect of SCMs such as a Class C fly ash on ASR was also investigated through nonlinear acoustic measurements. In addition, a case study of effect of aggregate angularity and gradation was carried out using NIRAS technique. The following conclusions can be reached based upon nonlinear acoustic experiments

- Both NWMS and NIRAS techniques clearly distinguish a highly reactive aggregate F1 from other aggregates in the mortar bar tests. The representative nonlinearity parameter defined in both experimental techniques increase significantly at a very early test age (around 4-6 days of exposure in the mortar test). The separation of nonlinearity parameters for aggregate F1 from other aggregates at the early age is consistent with the trend of expansion variation in the AMBT measurements.
- In the mortar bar tests, moderately reactive aggregates F4 and F6 are distinguished more apparently by the developed NWMS and NIRAS techniques than the accompanying AMBT expansion measurements. The nonlinearity parameter of aggregate F4 is average 2.5 times the nonlinearity parameter of aggregate F6 in the NWMS measurements. The nonlinearity parameter of aggregate F4 is averagely 2 times the nonlinearity parameter of aggregate F6 from day 2 to day 6 in the NIRAS measurements. In contrast, the expansion of aggregate F4 is average 10% higher than the expansion of aggregate F6 in the AMBT measurements.

- Nonlinearity parameters of aggregate F1 in NWMS and NIRAS techniques both increase rapidly to a peak value at the early test age and then decline afterwards. Correlated with accompanying petrographic analysis, the variation pattern of nonlinearity parameter for aggregate F1 is believed to be affected by the change of material microstructure. The formation and expansion of ASR gel increases the material heterogeneity, and the opening/closure cycles of microcracks have been proved one mechanism leading to the increase of material nonlinearity. The changes of ASR gel and microcracks in the late exposure period also largely contribute to the post-peak decrease of the nonlinearity parameter for aggregate F1. First, the ASR gel initially formed could become more fluid-like or dissolved with the continuing immersion in the highly alkaline solution. Microcracks become further widen which leads to the attenuation of the open/closure cycles at the late ages. Petrographic images of mortar samples cast with aggregate F1 provide microscopic evidence that the occurrence time of observed ASR gel and microcrack (initiation and progression) coincide with the increase/decrease trend of nonlinearity parameters in NWMS and NIRAS measurements. As such, the nonlinearity parameter is more likely a measure newly formed ASR gel and microcracks in the damaged materials. The cumulative of measured nonlinearity parameter is a better caliber for the overall damage in materials. In fact, the cumulative nonlinearity parameter in NIRAS technique has a very good correlation with the expansion results for the four aggregates tested.
- In addition to the AMBT expansion data, measurements from developed acoustic techniques also validate that the use of fly ash can effectively mitigate ASR

damage in cement-based materials. In the NIRAS measurements, the nonlinearity parameter of samples blended with 20% fly ash is significantly reduced compared to the nonlinearity parameter of samples without the fly ash blend and corresponds well with ABMT expansion results.

- Three non-reactive aggregates are used to study effects of aggregate parameters such as the gradation and angularity on NIRAS measurements. It is found that the gradation may have a minor effect on the measured nonlinearity parameter. The angular shape of non-reactive aggregates causes a large increase in the measurements of nonlinearity in the current research.
- With concrete, the NIRAS technique can clearly distinguish aggregate F1 in the CPT measurements as early as a few weeks, earlier than by expansion testing. Also, moderately reactive aggregate C2 is also clearly distinguished from slightly reactive aggregate C1 after ~6 months via NIRAS, while this distinction is not evident until the end of the one-year expansion test and is not clear as well in the expansion data.
- Despite the limited numbers of aggregates tested, the cumulative nonlinearity parameter defined in the NIRAS technique may have the potential to be a complementary parameter to the expansion limit broadly used in expansion methods. For example, a value of 18 for the cumulative nonlinearity parameter may be set for the limit of aggregate reactivity in the end of 14 days in AMBT tests, which corresponds to the expansion limit of 0.1% at 14 days. However, it has to be addressed again that this value is based on tests for a limited numbers of aggregates, and more research should be conducted based on a more wide range

of aggregate sources for the quantitative definition of the value of nonlinearity parameters corresponding to the expansion limits in AMBT and CPT methods.

9.1.4 Impact of Research

Cement-based materials are complicated composites consisting of cement paste, aggregates and the interfacial transition zone. Due to the inherent material heterogeneity, it is very difficult to quantitatively measure damage in concrete using acoustic or ultrasonic techniques. For example, previous research [24, 25] used the pulse velocity method and attenuation method to characterize different ASR damage. Similar to the results of pulse velocity measurements in this research, these linear measurements may be sensitive to differentiate a highly reactive aggregate from a non-reactive aggregate, but cannot provide a clear distinction for aggregates having similar levels of reactivity, which actually are more necessary in practice. This research is the first successful work to apply new nonlinear acoustic techniques for quantitatively characterizing different levels of ASR damage in concrete. In conjunction with supplementary experimental tools such as petrographic analysis, this robust test methodology provides a new perspective to investigate different types of damage (not only ASR) in concrete in a timely manner.

According to the latest ASCE Report Card for America's Infrastructure released in January 2009, the overall condition of infrastructure in the United States had a grade of "D", with a total of 2.2 trillion dollars is needed to be invested on the deteriorated infrastructure system. Thus it is of the utmost importance to accurately assess the health condition of existing structures. With the successful experience in ASR damage, the nonlinear acoustic techniques developed in the current research could have further

applications in the structural health monitoring for varying deterioration mechanisms in concrete infrastructure.

9.2 Recommendations

Based upon the outcomes of the current research, further testing and development in the following areas is recommended.

- Although the current results showed that the developed NWMS and NIRAS techniques were able to differentiate well between fine aggregates of different reactivity, only a limited number of aggregates have been tested to date. To generalize the current findings and to provide data allowing for the identification of limits on nonlinear parameters defining reactivity, more aggregates from a wider variety of sources should be further investigated. Further testing should consider aggregates of varying reactivity, mineralogy, fineness or surface area, angularity, porosity and specific gravity to better assess the influence of these features on the nonlinear parameters.
- The current research considered just one combination of cement and SCM. Different SCMs and more combinations such as binary and ternary should be examined for a range of aggregate reactivity in the future work.
- Improvements in test set-ups should be examined. For example, both NWMS and NIRAS techniques use an instrumented hammer to generate the vibration of samples. Additional instruments such as loud speakers and ultrasonic transducers can be considered for the excitation generation. The control and operation of loud speakers and ultrasonic transducers can be carried out digitally, which can reduce

the workload of manual operation of the instrumented hammer. In addition, with improvements in instrumentation, it is very likely possible to make measurements on full-size CPT samples, eliminating the need to reduce the sample size. Thus it is recommended to revise the experimental apparatus to further increase the excitation level for the vibration modes of concrete prism samples in the future tests.

- The test methodology could be expanded to assess damage state for concrete samples cored from structures. Such testing could be performed using the NWMS and/or NIRAS techniques to identify concrete which has been damaged and also to monitor the rate of damage progression over time. The experimental setup may need minor changes such as the fixture for clamping samples in the NIRAS technique to satisfy other cross-section shape of cored samples other than the currently used rectangular one. Ultimately, the experimental techniques could be further extended to the *in situ* assessment of concrete components in fields.
- While preliminary modeling work has been conducted in the current work, because ASR occurs by such a complicated chemical process, a more sophisticated predictive model is necessary to more accurately capture the physical, mechanical, and chemical responses of the complex material during the varying stages of damage. It is fundamentally important to develop a more advanced predictive model relating the progression of ASR damage to nonlinear measurements both to improve the interpretation of the nonlinear data and to improve understanding of the mechanisms of damage resulting from this reaction.

- One significant advantage of the developed experimental techniques is their sensitivity and reliability to a wide range of material degradation. Thus, the developed experimental techniques can be applied for the inspection of damage caused by other mechanisms other than ASR, such as corrosion, thermal effects and freeze-thaw cycling which have been broadly found in concrete infrastructure. These different damage mechanisms have a similar effect on the material properties of concrete, i.e., the increase of nonlinear terms in constitutive relations, which can be substantially captured by the developed nonlinear acoustic techniques. The unique microstructural signature of concrete in each damage mechanism can be further differentiated by the microscopic analysis, as in the ASR case mentioned in the current research.

APPENDIX

NWMS RESULTS OF OTHER AGGREGATES

As mentioned in Chapter 7, aggregates F2, F3, F5 and F9 were also used for the NWMS tests. However, unlike the results of aggregates F1, F4 and F6 shown in Figure 7.9, the results of aggregates F2, F3, F5 and F9 do not have a very clear correlation with respect to their corresponding reactivity.

Figure A.1 shows the variation of nonlinearity parameter *D* with respect to exposure time for aggregates F2, F3, F5 and F9. According to the AMBT expansion results in Figure 3.7, aggregates F2, F3, F5 and F9 are supposed to be highly reactive, highly reactive, moderately reactive and non-reactive, respectively. But it is seen in Figure A.1 that there is a large drop at day 4 and day 5 although the nonlinearity parameter of aggregate F2 increases to a high value at day 3. As for aggregate F9, the nonlinearity parameter has a large rise at day 6, which is not anticipated based on its reactivity. The nonlinearity parameters of aggregates F3 and F5 have no irregular peaks, but the relative values of the nonlinearity parameters contradict the expansion data in Chapter 3.

The reasons for the discrepancy shown in results for aggregate F2, F3, F5 and F9 are not very clear. Several possible explanations are discussed here. First, the angularity of aggregates may have effect on the NWMS results. As found in NIRAS results, the angularity of aggregates could affect the variation of nonlinearity parameter, causing the unexpected peak during the middle of test age. The similar effect could exist for the NWMS results in Figure A.1, for example, the peak of nonlinearity parameter of aggregate F9 which is crushed from coarse aggregates and has a more angular shape. In

addition, it is not easy to interpret the NWMS results sometimes because the relatively high frequency signals were used in experiments. The sidebands are supposed to occur at the location nearby the high frequency end (39kHz) so that they usually have a value around 35-45 kHz. The attenuation of cement-based materials on the high-frequency sideband occasionally compromises the effort of accurately calculating the sideband energy and then scatters the presuming linear relation between impact energy and sideband energy, which further causes the error for the calculation of nonlinearity parameter.

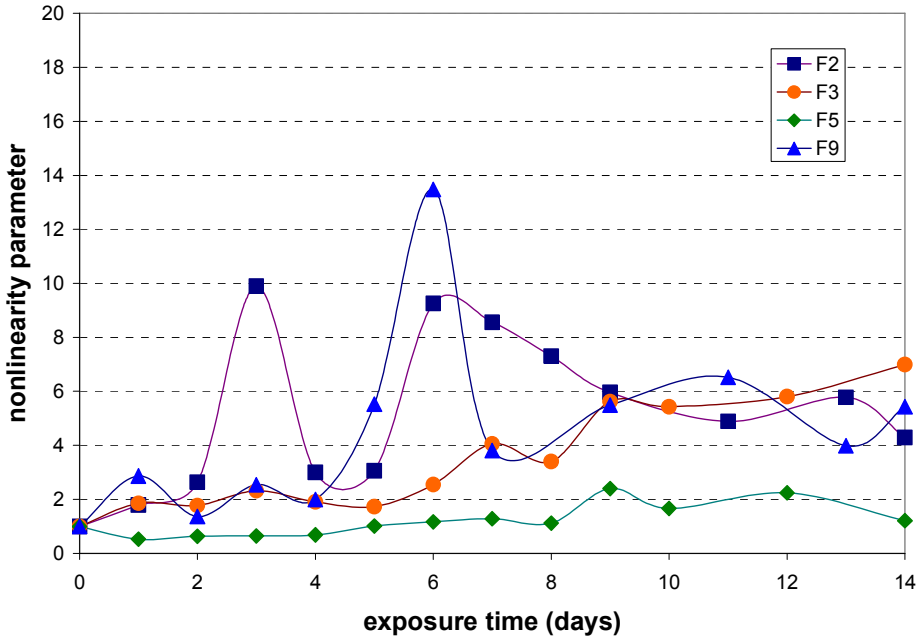

Figure A.1 NWMS results for aggregates F2, F3, F5 and F9

REFERENCES

[1] Dent Glasser, L.S. and Kataoka, N., "On the role of calcium in the alkali-aggregate reaction," *Cement and Concrete Research*, 11 (1981), 321-331.

[2] Chatterji, S., "Chemistry of alkali-silica reaction and testing of aggregates," *Cement and Concrete Composites*, 27 (2005) 788-795.

[3] Kurtis, K.E., Monteiro, P.J.M., Brown, J.T. and Meyer-Ilse, W., "Imaging of ASR gel by soft X-ray microscopy," *Cement and Concrete Research*, 28 (1998), 411-421.

[4] Swamy, R.N., "The alkali-silica reaction in concrete," Blackie, Glasgow, 1992.

[5] Helmuth, R., "Alkali-silica reactivity: An overview of research," SHRP-C-342, National Research Council, Washington, DC, 1993.

[6] Mehta, P.K., and Monteiro, P.J.M., "Concrete: microstructure, properties and materials," 3rd Edition, McGraw-Hill Publisher, New York, 2005.

[7] Stanton, T. E., "Expansion of concrete through reaction between cement and aggregate," *in Proceedings of the American Society of Civil Engineers*, V. 66 No. 10, New York, 1940, 1781-1811.

[8] Borge Johannes Wigum, "Alkali-aggregate reactions in concrete: Properties, classification and testing of Norwegian cataclastic rocks," *PhD Dissertation*, University of Trondheim, 1995.

[9] ASTM C 295, "Standard guides for petrographic examination of aggregates in concrete," *Annual Book of ASTM Standards* vol. 04.02, (Concrete and Aggregates), Philadelphia (PA), 2007.

[10] Folliard, K.J., Fournier, B., and Thomas, M., "ASR testing and evaluation protocols, Protocol A: Determining the reactivity of concrete aggregates and selecting appropriate measures for preventing deleterious expansion in concrete," Federal Highways Administration, Washington D.C., 2008.

[11] Farny, J., and Kosmatka, S. "Diagnosis and concrete of alkali-aggregate reactions in concrete," Portland Cement Association, 1997.

[12] ASTM C 1260-07, "Standard test method for determining the potential alkali reactivity aggregates (accelerated mortar-bar method)." *Annual Book of ASTM Standards* vol. 04.02, (Concrete and Aggregates), Philadelphia (PA), 2007.

[13] ASTM C 1567-04, "Standard test method for determining the potential alkali reactivity of combinations of cementious materials and aggregate (accelerated mortar-bar method)," *Annual Book of ASTM Standards* vol. 04.02, (Concrete and Aggregates), Philadelphia (PA), 2008.

[14] ASTM C 1293-08, "Standard test method for concrete aggregates by determination of length change of concrete due to alkali-silica reaction," *Annual Book of ASTM Standards*, vol. 04.02 (Concrete and Aggregates), Philadelphia (PA), 2008.

[15] Shaikh, H., "Mitigation of delayed ettringite formation in laboratory specimens," *PhD Dissertation*, University of Maryland, 2007.

[16] Folliard, K.J., Thomas, M.D.A., and Kurtis, K.E., "Guidelines for the use of lithium to mitigate or prevent ASR," *FHWA-RD-03-047*, Federal Highways Administration, National Research Council, Washington D.C., 2003.

[17] Shayan, A., Xu, A., and Morris, H., "Comparative study of the concrete prism test (CPT 60°C, 100%RH) and other accelerated tests," *in Proceedings of the 13th ICAAR*, Trondheim, Norway (2008).

[18] DeGrosbois, M., and Fontaine, E., "Performance of 60°C-accelerated concrete prism test for the evaluation of potential alkali-reactivity of concrete aggregates," *in Proceedings of the 11th ICAAR*, Québec, Canada (2000), 277-286.

[19] Lu, D.Y., Fournier, B., and Grattan-Bellew, P.E., "Evaluation of accelerated test methods for determining alkali-silica reactivity of concrete aggregates," *Cement and Concrete Composites*, 28 (2006), 546-554.

[20] Ideker, J.H., East, B.L., Folliard, K.J., Thomas, M., and Fournier, B., "The current state of the accelerated concrete prism test," *in Proceedings of the 13th ICAAR*, Trondheim, Norway (2008).

[21] Krautkramer, J., and Krautkramer, H., "Ultrasonic testing of materials," Springer-Verlag, Berlin-Heiderberg-New York, 1977.

[22] Green, R.E., "Ultrasonic investigation of mechanical properties," Academic Press, New York & London, 1973.

[23] Amasaki, S., and Takagi, N., "The estimate for deterioration due to alkali-silica reaction by ultrasonic spectroscopy," *in Proceedings of the 8th ICAAR*, Kyoto, Japan (1989), 839-844.

[24] Bungey, J., "Ultrasonic testing to identify alkali-silica reaction in concrete," *British Journal of Nondestructive Testing*, 33 (1991), 227-231.

[25] Saint-Pierre, K., Rivard, P., and Ballivy, G., "Measurement of alkali-silica reaction progression by ultrasonic waves attenuation," *Cement and Concrete Research*, 37 (2007), 948-956.

[26] Phair, J.W., Tkachev, S.N., Manghnani, M.H., and Livingston, R.A., "Elastic and structural properties of alkaline-calcium silica hydrogels," *Journal of Material Research* 20 (1995), 344-349.

[27] Pier Paolo Delsanto, "Universality of Nonclassical nonlinearity: Application to nondestructive evaluations and ultrasonics," Springer, 2006.

[28] K. Van Den Abeele, J. De Visscher, "Damage assessment in reinforced concrete using spectral and temporal nonlinear vibration techniques," *Cement and Concrete Research* 30 (2000) 1453-1464.

[29] J.-Y. Kim, L.J. Jacobs, J. Qu, J.W. Littles, "Experimental characterization of fatigue damage in a nickel-base superalloy using nonlinear ultrasonic waves," *Journal of the Acoustical Society of America* 120 (2006) 1266-1273.

[30] Herrmann, J., Kim, J.-Y., Qu, J., and Jacobs, L.J., "Assessment of material damage in a nickel-base superalloy using nonlinear Rayleigh surface wave," *Journal of Applied Physics* 99 (2006) 124913.

[31] Pruell, C., Kim, J.-Y., Qu, J., and Jacobs, L.J., "Evaluation of plasticity-driven material damage using Lamb waves," *Applied Physical Letters* 91 (2007) 231911.

[32] Donskoy, D., Sutin, A., and Ekimov, A., "Nonlinear acoustic interaction on contact interfaces and its use for nondestructive testing," *NDT&E International* 34 (2001) 231-238.

[33] Ekimov, A.E., Didenkulov, I.N., and Kazakov, V.V., "Modulation of torsional waves in a rod with a crack," *Journal of Acoustical Society of America* 106 (1999) 1289-1292.

[34] ASSHTO T 303-00, "Standard method of test for accelerated detection of potentially deleterious expansion of mortar bars due to alkali-silica reaction," *Standard specifications for transportation materials and methods of sampling and testing Part 2B: Tests*, American Association of State Highway and Transportation Officials, Washington D.C., 2006.

[35] Oberholster, R.E., and Davies, G., "An accelerated method for testing the potential alkali reactivity of siliceous aggregates," *Cement and Concrete Research*, 16 (1986), 181–189.

[36] Grattan-Bellew, P.E., "A critical review of ultra accelerated tests for alkali-silica reactivity," *Cement and Concrete Research*, 19 (1997), 403-414.

[37] Sanchez, L., Kuperman, S.C., Helene, P., and Kihara, Y., "Trials to correlate the accelerated mortar bar test, the standard and the accelerated concrete prism tests," *in Proceeding of the 13th ICAAR*, Trondheim, Norway (2008).

[38] CSA A23.2-25A, "Test method for detection of alkali-silica reactive aggregate by accelerated expansion of mortar bars," *CSA A23.2-04: Methods of Test for Concrete*, Canadian Standards Association, Mississauga (ON), 2004b, 240-245.

[39] CSA A23.2-28A, "Standard practice for laboratory testing to demonstrate the effectiveness of supplementary cementing materials and chemical admixtures to prevent alkali-silica reaction in conrete," *CSA A23.2-04: Methods of Test for Concrete*, Canadian Standards Association, Mississauga (ON), 2004, 260-262.

[40] RILEM TC106-AAR, "Detection of potential alkali-reactivity of aggregates-the ultra-accelerated mortar-bar test," *Materials and Structures*, 33 (2000), 283–293.

[41] RILEM TC-191-ARP, "Alkali-reactivity and prevention – assessment, specification and diagnosis of alkali-reactivity," *Materials and Structure*, 36 (2003), 472-479.

[42] Xu, Z., Shen, Y., and Lu, D., "Main parameters in the new test method for alkali-silica reactivity," *Journal of Nanjing University in Chemical Technology*, 20 (1998), 1-7.

[43] Tang, M., Han, S., and Zheng, S., "A rapid method for identification of alkali reactivity of aggregate," *Cement and Concrete Research*, 13 (1983), 417-422.

[44] Lu, D.Y., Fournier, B., and Grattan-Bellew, P.E., "Evaluation of accelerated test methods for determining alkali-silica reactivity of concrete aggregates," *Cement and Concrete Composites*, 28 (2006), 546-554.

[45] Grattan-Bellew, P.E., Cybanski G, Fournier B, and Mitchell L., "Proposed universal accelerated test for alkali-aggregate reaction the concrete microbar test," *Cement Concrete and Aggregates*, 25 (2004), 29-34.

[46] Andic-Cakir, O., Copuroglu, O., and Ramyar, K., "Evaluation of alkali-silica reaction by concrete microbar test," *ACI Materials Journal*, 106 (2009), 184-191.

[47] Shayan, A., Xu, A., and Morris, H., "Comparative study of the concrete prism test (CPT 60°C, 100%RH) and other accelerated tests," *in Proceeding of the 13th ICAAR*, Trondheim, Norway (2008).

[48] Thomas, M., Fournier, B., Folliard K., Ideker, J., and Shehata, M., "Test methods for evaluating preventive measures for controlling expansion due to alkali-silica reaction in concrete," *Cement and Concrete Research*, 36 (2006), 1842-1856.

[49] CSA A23.2-27A, "Standard practice to identify degree of alkali-reactivity of aggregates and to identify measures to avoid deleterious expansion in concrete," *CSA A23.2-04: Methods of Test for Concrete*, Canadian Standards Association, Mississauga (ON), 2004c, 251-259.

[50] CSA A23.2-14A, "Potential expansivity of aggregates (procedure for length change due to alkali-aggregate reaction in concrete prisms)," *CSA A23.2-04: Methods of Test for Concrete*, Canadian Standards Association, Mississauga (ON), 2004a, 207–216.

[51] RILEM TC-106-AAR, "Detection of potential alkali reactivity of aggregates-methods for aggregate combinations using concrete prisms," *Materials and Structures*, 33 (2000b), 290–293.

[52] Tremblay, C., Berube, M.-A., Fournier, B., Thomas, M.D.A., and Stokes, D.B., "Performance of lithium-based products against ASR: application to Canadian reactive aggregates, reaction mechanisms and testing", *in Proceeding of the 12th ICAAR*, Beijing, China (2004), 668-677.

[53] Fournier, B., Nkinamubanzi, P.C., Lu, D., Thomas, M.D.A., Folliard, K.J., and Ideker, J., "Evaluating potential alkali-reactivity of concrete aggregates – how reliable are the current and new test methods?" *Symposium on alkali-aggregate reaction in concrete structures*, Rio de Janeiro, Brazil (2006).

[54] Ranc, R., and Debray, L., "Reference test methods and a performance criterion for concrete structures," *in Proceeding of the 9th ICAAR*, London, UK (1992), 824-831.

[55] RILEM TC-191-ARP, "Alkali-reactivity and prevention – assessment, specification and diagnosis of alkali-reactivity," *Materials and Structure*, 36 (2003), 472-479.

[56] Einarsdottir, S.U., and Wigum, B.J., "Alkali aggregate reaction in Iceland – new test methods," *in Proceeding of the 13th ICAAR*, Trondheim, Norway (2008).

[57] Fournier, B., Chevrier, B., DeGrosbois, R., Lisella, M., Folliard, R., Ideker, K., Shehata, M., Thomas, M., and Baxter, S., "The accelerated concrete prism test (60°C): variability of the test method and proposed expansion limits," *in Proceeding of the 12th ICAAR*, Beijing, China (2004), 315-323.

[58] DeGrosbois, M., and Fontaine, E., "Performance of 60°C-accelerated concrete prism test for the evaluation of potential alkali-reactivity of concrete aggregates," *in Proceeding of the 11th ICAAR*, Québec, Canada (2000), 277-286.

[59] Touma, W.E., Fowler, D.F., and Carrasquillo, R,L., "Alkali-silica reaction in Portland cement concrete: testing methods and mitigation alternatives," *Report ICAR 301-1F*, International Center for Aggregates Research, Austin, Texas (2001).

[60] Folliard, K.J., Fournier, B., Thomas, M., and Bérubé, M.-A., "Assessing aggregate reactivity using the accelerated concrete prism test," *8th CANMET/ACI International Conference on Recent Advances in Concrete Technology – supplementary paper*, Las Vegas, 269-283.

[61] Ben Haha., M., Gallucci., E., Guidoum., A., and Scrivener., K. L., "Relation of expansion due to alkali silica reaction to the degree of reaction measured by SEM image analysis," *Cement and Concrete Research*, 37(2007), 1206-1214.

[62] Jensen, V., "Alkali aggregate reaction in southern Norway," *PhD thesis*, University of Trondheim, 1993.

[63] Niels Thaulow, Mette Geiker, "Determination of the residual reactivity of alkali silica in concrete," *in Proceeding of the 9th ICAAR*, London, UK (1992), 1050-1058.

[64] Folliard, K.J., Fournier, B., Thomas, M., and Bérubé, M.-A., "ASR testing and evaluation protocols, Protocol B: Diagnosis and prognosis of alkali-aggregate reaction (AAR) in transportation structures," Federal Highways Administration, Washington D.C., 2008b.

[65] Mix, P.E., "Introduction to nondestructive testing: A training guide," Hoboken, N.J., John Wiley & Sons (2005).

[66] ASTM C597-02, "Standard test method for pulse velocity through concrete," *Annual Book of ASTM Standards* vol. 04.02, (Concrete and Aggregates), Philadelphia (PA), 2002.

[67] Kamada, T., Nagataki, S., and Iwanami, M., "Evaluation of material deterioration in concrete by nondestructive testing methods," *International Conference on Engineering Materials*, Ottawa, Canada, 95, (1997), 453-466.

[68] Daponte, P., Maceri, F., and Olivito, R.S., "Ultrasonic signal-processing techniques for the measurement of damage growth in structural materials," *IEEE Transactions on Instrumentation and Measurement*, 44 (1995), 1003-1008.

[69] Van Hauwaert, J., Thimus, J.-F., and Delanny, F., "Use of ultrasonics to follow crack," *Ultrasonics* 36 (1998), 209-217.

[70] Buck, O., Morris, W.L., and Richardson, J.M., "Acoustic harmonic generation at unbounded interfaces and fatigue cracks," *Applied Physics Letters*, 33 (1978), 371-372.

[71] Richardson, J.M., "Harmonic generation at an unbounded interface: I. Planar interface between semi-infinite elastic media," *International Journal of Engineering and Science*, 17 (1979), 73-85.

[72] Nazarov, V.E., and Sutin, A.M., "Nonlinear elastic constants of solids with cracks," *Journal of the Acoustic Society of America*, 102 (2005), 3349-3354.

[73] Yost, W.T., and Cantrell, J.H., "The effect of fatigue on acoustic nonlinearity in aluminum alloys," *in Proceeding of IEEE*, 2 (1992), 947-954.

[74] Na, J.K. Cantrell, J.H., and Yost, W.T., "Linear and nonlinear properties of fatigued 410Cb stainless steel," *Review of Progress of Quantitative Nondestructive Evaluation*, 15 (1996), 1479-1488.

[75] Barnard, D.J., Dace, G.E., and Buck, O., "Acoustic harmonic generation due to thermal embrittlement of Inconel 718," *Journal of Nondestructive Evaluation*, 16 (1997), 67-75.

[76] Nagy, P.B., "Fatigue damage assessment by nonlinear ultrasonic material characterization," *Ultrasonics*, 36 (1998), 375-381.

[77] Frouin, J., Sathish, S., Matikas, T.E., and Na, J.K., "Ultrasonic linear and nonlinear behavior of fatigued Ti-6Al-4V," *Journal of Material Research*, 14 (1999), 1295-1298.

[78] Van Den Abeele, K. E.-A., Johnson, P.A., and Sutin, A., "Nonlinear elastic wave spectroscopy techniques to discern material damage, Part I: Nolinear wave modulation spectroscopy (NWMS)," *Research in Nondestructive Evaluation*, 12 (2000), 17-30.

[79] Kazakov, V.V., Sutin, A., and Johnson, P.A., "Sensitive imaging of an elastic nonlinear wave-scattering source in a solid," *Applied Physics Letters*, 81 (2002), 646-648.

[80] Warnemuende, K., and Wu, H.-C., "Actively modulated acoustic nondestructive evaluation of concrete," *Cement and Concrete Research*, 34 (2004), 563-570.

[81] Zumpano, G., and Meo, M., "Damage detection in an aircraft foam sandwich panel using nonlinear elastic wave spectroscopy," *Computer and Structures*, 86 (2008), 483-490.

[82] Van Den Abeele, K. E.-A., Sutin, A., Carmeliet, J., and Johnson, P.A., "Micro-damage diagnostics using nonlinear elastic wave spectroscopy(NEWS)," *NDT&E International*, 34 (2001), 239-248.

[83] McCall, K.R., and Guyer, R.A., "Equation of state and wave propagation in hysteretic nonlinear elastic-materials," *Journal of Geophysical Research*, 99 (1994), 23887-23897.

[84] McCall, K.R., and Guyer, R.A., "A new theoretical paradigm to describe hysteresis, discrete memory and nonlinear elastic wave propagation in rock," *Nonlinear Processes Geophysics*, 3 (1996), 89-101.

[85] Van Den Abeele, K. E.-A., Johnson, P.A., Guyer, R.A., and McCall, K.R., "On the quasi-analytic treatment of hysteretic nonlinear response in elastic wave propagation," *Journal of the Acoustic Society of America*, 101 (1996), 1885-1898.

[86] Van Den Abeele, K. E.-A., "Multi-mode nonlinear resonance ultrasound spectroscopy for defect imaging: An analytical approach for the one-dimensional case," *Journal of the Acoustic Society of America,* 122 (2007), 73-90.

[87] Guyer R.A., McCall K.R., and Van Den Abeele, K. E.-A., "Slow elastic dynamics in a resonant bar of rock," *Geophysical Research Letters*, 25 (1998), 1585-1588.

[88] Landau, L.E., and Lifshitz, E., "Elasticity," Oxford, Pergamon (1986).

[89] Johnson, P.A., Zinszner, B., and Rasolofosaon, P.N.J., "Resonance and elastic nonlinear phenomena in rock," *Journal of Geophysical Research*, 101 (1996), 11553-11564.

[90] Payan, C., Garnier, V., and Moysan, J. "Applying nonlinear resonant ultrasound spectroscopy to improving thermal damage assessment in concrete," *JASA Express Letters*, 121 (2007), 125-130.

[91] Chen, X.J., Kim, J.-Y., Kurtis, K.E., Qu, J., Shen, C.W., and Jacobs, L.J., "Characterization of progressive microcracking in Portland cement mortar using nonlinear ultrasonics," *NDT&E International*, 41 (2008), 112-118.

[92] Swamy, R.N., and Al-Asali, M.M., Engineering properties of concrete affected by alkali-silica reaction, *ACI Materials Journal* 85 (1988) 367-377.

[93] Giaccio, G., Zerbino, R., Ponce, J.M., and Batic, O.R., Mechanical behavior of concretes damaged by alkali-silica reaction, *Cement and Concrete Research* 38 (2008), 993-1004.

[94] Chen, J., Jayapalan, A.J., Kurtis, K.E., Kim, J.-Y., and Jacobs, L.J., "Nonlinear wave modulation spectroscopy method for ultra-accelerated ASR assessment," *ACI Materials Journal* 106 (2009), 340-348.

[95] Kim, J.-Y., and Lee, J.-S., "A micromechanical model for nonlinear acoustic properties of interfaces between solids," *Journal of Applied Physics*, 101 (2007), 043501.

[96] Chen, J., Jayapalan, A.J., Kurtis, K.E., Kim, J.-Y., and Jacobs, L.J., "Rapid evaluation of alkali-silica reactivity of aggregates using a nonlinear resonance spectroscopy technique," *Cement and Concrete Research* (in press).

[97] Tao, L., Mori, Y., and Motooka, S., "Evaluation of quality of concrete by linear predictive coefficient method with multi-reflected elastic wave," *Acoustic Science & Technology*, 25 (2004), 483-485.